TECHNISCHE
UNIVERSITÄT
WIEN

ACIN

AUTOMATION & CONTROL INSTITUTE
INSTITUT FÜR AUTOMATISIERUNGS-
& REGELUNGSTECHNIK

Optimal Control Strategies for Quantum Field Thermal Machines

DIPLOMA THESIS

Conducted in partial fulfillment of the requirements for the degree of a

Diplom-Ingenieur (Dipl.-Ing.)

supervised by

Univ.-Prof. Dr. techn. A. Kugi
Dr. techn. A. Deutschmann-Olek

submitted at the

TU Wien

Faculty of Electrical Engineering and Information Technology
Automation and Control Institute

by
Katharina Schrom
Matriculation number 01525093

Vienna, November 2021

Vorwort

An dieser Stelle möchte ich all jenen danken, die zum Gelingen dieser Diplomarbeit beigetragen haben.

Danke an Dr. Andreas Deutschmann-Olek und Univ. Prof. Andreas Kugi für die hervorragende Betreuung. Ich bedanke mich für die Freiräume die mir in der Gestaltung dieser Arbeit gegeben wurden und für die fachliche und persönliche Unterstützung.

Ich bedanke mich auch für die Zusammenarbeit mit der Gruppe von Univ. Prof. Jörg Schmiedmayer vom Atominstitut, da diese Arbeit anderenfalls nicht zustande gekommen wäre. Danke an João Sabino für die Unterstützung durch experimentelle Messungen und an Dr. Sebastian Erne, der mir bei vielen fachliche Fragen weitergeholfen hat.

Schlussendlich will ich mich auch bei allen Freunden und bei meiner Familie bedanken, die mich durch alle Höhen und Tiefen des letzten Jahres begleitet haben.

Wien, November 2021

Abstract

Advanced experimental setups to prepare and manipulate Bose-Einstein Condensates open the possibility to realise quantum field thermal machines (QFTMs), the analogue to classical heat pumps acting on the quantum field of a gas. With the aim of enhancing the performance of such systems, this work studies the dynamics of the experimental quasi condensate within mean-field theory and for non-zero temperatures. Optimal trajectories for a complete cooling cycle are derived that minimise mean-field excitations whereby different approaches are compared. A minimum variance estimator is designed to adapt parameters of the mathematical model based on experimental data. In studying the condensate at non-zero temperatures, we find that trajectories that minimise mean-field excitations also alleviate undesired heating during the cooling sequence.

Kurzzusammenfassung

Moderne Versuchsaufbauten zur Erzeugung und Manipulation von Bose-Einstein Kondensaten eröffnen neue Möglichkeiten in der Realisierung von quantenmechanischen Wärmepumpen, dem Analog zur klassischen Wärmepumpe zur Manipulation des Quantenfeldes des Gases. Mit dem Ziel, die Performance einer solchen Wärmepumpe durch optimale Ansteuerung zu verbessern, wird die Dynamik des Quasi-Kondensats im Experiment im Rahmen der Mean-Field Theorie und für Temperaturen über dem absoluten Nullpunkt untersucht. Dazu werden optimale Trajektorien für alle Teilsequenzen der Wärmepumpe berechnet, sodass Anregungen des Mean-Fields minimiert werden. Zur Lösung des Optimalsteuerungsproblems werden verschiedene Ansätze miteinander verglichen. Darüber hinaus wird ein Minimum-Varianz Schätzer für fluktuierende Modellparameter entworfen. In der Untersuchung von thermischen Zuständen wird gezeigt, dass diese optimalen Trajektorien auch den Eintrag zusätzlicher thermischer Energie zu einem großen Teil verhindern können.

Contents

IV

List of Figures

List of Tables

1 Introduction

In recent times, progress in quantum physics and enhanced quantum experiments vastly improve the capabilities of controlling and manipulating individual quantum systems. While previously experiments in quantum physics were mainly designed to observe quantum effects or validate theoretical models, advanced experimental setups nowadays try to make use of genuine quantum effects. These so called quantum techniques use effects like tunneling, entanglement or superposition, to fulfil some desired task with superior performance to classical techniques. The use of quantum simulators [1] for example makes simulations of less accessible quantum systems possible, which might be infeasible to calculate with conventional techniques. Quantum metrology [2], e.g. atomic interferometry, uses effects of squeezing and entanglement to surpass classical measurement tools. The emerging field of quantum computing [3] promises a significant reduction of computation speed, but also comes with the development of quantum decryptors, which will leave information that was encrypted with today's methods vulnerable. Likewise, quantum cryptography [4] can offer solutions for this problem. By using quantum effects, an ultimate encryptor could be built which would also withstand possibly in the future developed quantum- or non-quantum algorithms.

A number of these quantum techniques have their origin in classical systems. The steam engine can be considered one of the most impactful classical systems invented in the last centuries, and the limited understanding of its inner workings was a main driving force for the development of classical thermodynamics. Following this rational, a genuine quantum thermal machine could help exploring the nature of thermodynamics in the quantum regime [5, 6].

In [7], Gluza proposes a quantum field thermal machine (QFTM) that has its classic analogue in a heat pump. A heat pump transfers thermal energy from one place to another, acting against the striving of nature to equilibrate temperature distribution. It can cool a cold place while making a hot place hotter. The proposed QFTM from Gluza can provide an additional cooling stage for quantum gases or liquids and acts as a tool for further exploration of strong correlation and coherences. The observation and manipulation of quantum effects has proven to be notoriously difficult, requiring extremely precise and accurate capabilities. It is thus natural that [7] already points towards the exploitation of advanced control concepts to realize such a QFTM. Similarly, James Watt designed a centrifugal governor to stabilise the speed of the steam engine and its mathematical description by James Clerk Maxwell is considered the foundation of modern control theory [8].

The main differences between this classic heat pump and the proposed QFTM are the working fluid, the spatial dimensions of the machine and the methods of actuation and measurement. In an ordinary refrigerator, a refrigerant liquid undergoes a process called 'vapor-compression refrigeration' of evaporation, compression, condensation and expansion.

To replace this working liquid using a Bose Einstein Condensate (BEC) is a promising option. In 1925, Albert Einstein predicted a state of matter, where bosons (particles which can occupy the same quantum state) 'condense' at low temperatures in a single quantum state. They get indistinguishable from each other and behave like the same single particle which can be described by one single wave-function [9]. Newly developed tools of cooling atoms that are trapped in magnetic potentials on atom-chips made it possible to reach temperature regimes of 20 to 100 nK. The procedure of preparing BECs has become a routine in the labs around the world, which makes them attractive to use in such advanced applications.

To gain a deeper insight into quantum many-body phenomena, a variety of mathematical models was developed to describe BECs in different thermal regimes. A selection of these models can be found in Chapter 2. The existence of suitable mathematical descriptions that accurately describe the behaviour of the atoms in the experiment is another reason for using BECs in the proposed QFTM since it allows to apply model-based control theory.

1.1 Experimental setup

The components of a classic heat pump are an electrical compressor, two heat exchangers (coils or tubes where condensation and evaporation take place) and an expansion valve where the refrigerant liquid undergoes an abrupt reduction in pressure. In one cooling cycle, the liquid passes sequentially through all different stages of the refrigerator. In the QFTM proposed in [7], a BEC replaces the refrigerant liquid and is compressed, coupled and decompressed.

For the realisation of the QFTM, the experimental setup that is described in [10] is considered and later used to test the methods that are developed in this work. In this setup, 87Rb atoms are cooled by laser cooling and particle dissipation (i.e., evaporative cooling) to a temperature around 50 nK where quantum effects play a prominent role. The BEC is confined by an anisotropic magnetic potential due to micro currents on the atom-chip. This confinement potential is tighter in transversal direction than in longitudinal direction, and forms the atomic cloud to a cigar like shape. When cooled sufficiently low, the condensate reaches a 1D regime where it can be described by a 1D macroscopic wave-function and is now called quasi condensate.

To build a quantum machine and to apply control theory some form of actuation is required. In [11], [12] and [13], the confinement potential can be controlled by changing the currents of the magnetic micro traps. The design of a QFTM requires to create and manipulate several compartments. This problem of actuation is solved in the considered experimental setup by optical dipole trapping [14] of the BEC, which allows detailed control of potentials. Optical manipulation is obtained by directing a shaped laser beam on the BEC. The electric dipole interaction produces a trapping force, which enables the realisation of, at least to some extend, arbitrary time-dependent potential landscapes.

The intensity profile of the laser beam is shaped with a digital micro-mirror device (DMD), which is a matrix of micro mirrors. Those mirrors have two states and can either direct the incoming light to the BEC or somewhere else. The shaping of a desired potential is a non-trivial task [15], since the coherent light used in the setup introduces interference

(a) Preparation of a BEC with three compartments

(b) Compression of P

(c) Coupling of P and B

(d) Decompression of P

(e) Coupling S and P

(f) Decoupling of S and P
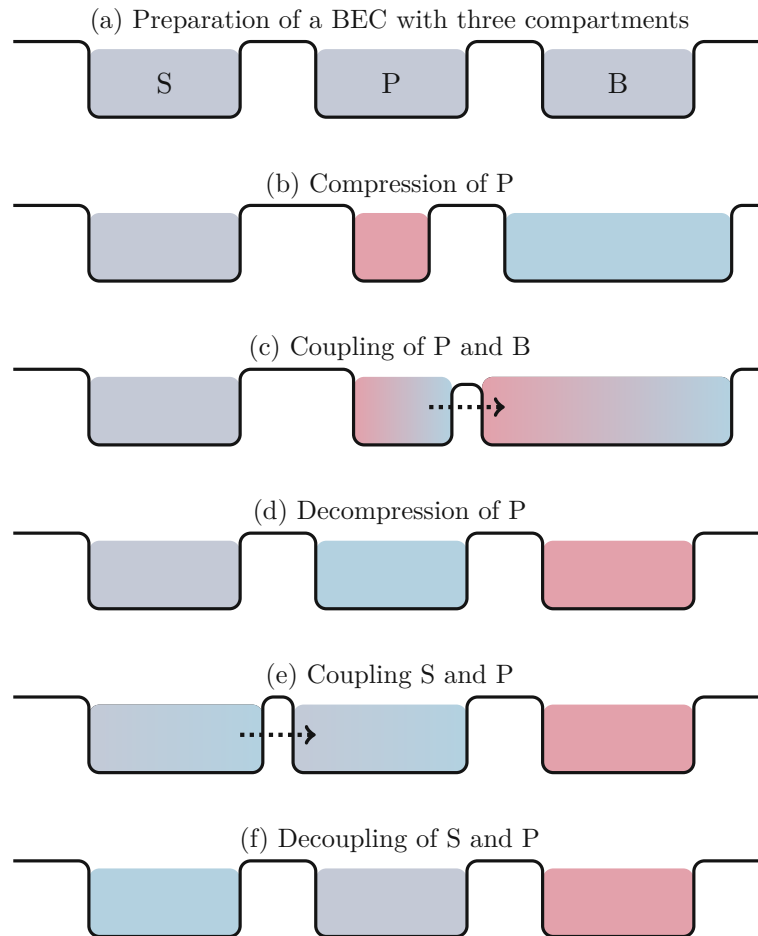
Figure 1.1: Quantum field thermal machine sequence. Steps (b) to (f) form a single cooling cycle and can be repeated for multiple several times.

and speckle patterns due to dust particles in the optical system. Thus, this work will focus on boxlike potential shapes with moving walls, which are easier to implement. The use of non-coherent light and suitable control methods to efficiently produce arbitrary potential shapes would allow more advanced configurations.

1.2 The QFTM sequence

Following [7], the quasi 1D condensate of the QFTM is divided into three compartments (Figure 1.1) by adapting the pixels of the DMD. The most left compartment is called system (S), the middle one is the piston (P) and the right one is called bath (B). Over one cooling cycle, energy should be transferred from S to B, while the number of atoms in all subsystems, especially in S, should not change. Analogously to the classical heat pump, such a cooling cycle consists of multiple subsequences:

- Initial state: S, P and B are initially decoupled and have the same temperature.

- Compression of P: While P gets compressed, the temperature and the density in P increases. B could simultaneously be decompressed to lower its temperature and to decrease the distance between P and B, for enhancing energy flow from P to B. Furthermore, it is desirable to adapt the chemical potential on P and B to avoid possible particle flow.

- Coupling of P and B: After adapting the chemical potentials of P and B, energy is transferred from the now hotter P to B. This coupling is done either by lowering the barrier between P and B or by further decreasing the wall width. During the coupling no atoms should travel from one compartment to the other.

- Decompression of P: After P and B are decoupled, P gets decompressed. While decompressing P, its temperature decreases. To build a working quantum field thermal machine, P now should be colder than S. To allow decompression of P, B has to be compressed again.

- Coupling of S and P: Since P is now colder than S, energy can be transferred from S to P by coupling them like P and B where coupled.

- Decoupling of S and P: To close the cycle, P gets decoupled from S. S should now be colder than at the beginning and energy was pumped from S to B. For further cooling of S, this cycle can be repeated multiple times until heat flow from P to B is not possible any more because of B being too hot.

To reach the higher-level goal of cooling the system (S) in an optimal way, it is reasonable to first understand the compression and decompression of a subsystem and the coupling and decoupling of two subsystems by their own. Those sequences are the building blocks of the QFTM and are called 'quantum thermal primitives' (QTPs). Each QTP is a transition between two configurations of the external potential, which is controlled by a number of control parameters.

The term of cooling inherently asks for a discussion of temperature. Regarding measurement possibilities in the experiment, there are two main quantities to get insight into the temperature of the condensate, namely the global density fluctuation and the phase coherence length. In a thermalized BEC, thermal energy is distributed in phase- and density fluctuations [16], which come on top of the classical field but for systems that are not in thermal equilibrium it is not possible to assign a single temperature. Nevertheless, quantities as the density fluctuation and the phase coherence length can sill give insight in the thermal state of the condensate even for non-thermalized states. These quantities are thus subject for optimisation in the long term. Furthermore, stochastic fluctuations interact with bulk excitations of the classic field and remaining bulk excitations will most likely result in a higher temperature of the condensate after thermalisation. Therefore, it is important to aim not only for the minimisation of phase and density fluctuations but also for the minimisation of excitations in the classic field.

1.3 Optimal control of BECs

Compression or decompression of the condensate by moving the walls of the box potential in a linear manner, i.e. using simple ramps as trajectories for the control parameters, will cause mean-field excitations and thus reduce the cooling efficiency. This problem raises the idea of applying control theory to suppress mean-field excitations when performing QTPs. The model for which optimal control theory is investigated in this work is the Gross-Pitaevskii equation (GPE), which is the classic equation of motion of the mean-field wave-function. This model only describes the evolution of the mean density and phase in the temperature regime $T \to 0$ and thus does not include stochastic fluctuations or any other quantities describing temperature. After one optimal cooling cycle, the wave-function in the GPE should be in the same ground state as before the sequence, and no such thing as cooling can be studied. Since particle numbers should be preserved in each subsystem, coupling in the GPE description should do nothing and quantities like the coupling time or strength and the compression ratio are not reasonable to optimise using only the GPE as mathematical description. Thus, to optimise the energy flow from S to P or from P to B during the coupling phases, an advanced mathematical model is necessary to describe the dynamics of phase and density fluctuations and include the temperature of the condensate. Models that go beyond mean-field theory are for example the stochastic GPE and the Truncated Wigner approach [16], the MCTDHB-Model [17] or linearised theories such as the Luttinger Liquid approach.

To reach the ultimate goal of cooling the system (S), a two-level approach will be pursued in this thesis. First, optimal control trajectories are investigated based on a mean-field description of the condensate. Solving this low-level control problem, quantum thermal primitives should be obtained that yield minimal excitations of the mean field. Some involved parameters of the quantum thermal primitives such as the coupling time or the compression ratio cannot be decided by employing a GPE description. To define these parameters, an optimisation of the resulting energy transport and achieved cooling has to be performed as a second control problem. This top-level control problem must go beyond mean-field theory and is possibly executed directly on the experiment using online-optimisation methods.

The optimality of each quantum thermal primitive is quantified with a cost functional. Together with a mathematical model of the system dynamics, an optimal control problem can be formulated. Optimal quantum control problems for BECs have been studied in multiple works. In [11], different benchmark problems (e.g. dislocating a condensate or splitting it into two by controlling the confinement potential of magnetic micro traps) are discussed. In [12], it was shown that optimal control theory can also be applied to 3D condensates and in [13] they go beyond mean-field theory and compare splitting in a two-mode model and using the MCTDHB method.

Due to the absence of real-time measurements, all of the above mentioned applications of optimal control theory (OCT) are pure feedforward control approaches. As such, they all share the same drawbacks as any open-loop control, i.e. the mathematical description has to fit the experiment extremely well to obtain good results. Since one is able to perform destructive measurements at some point of a QTP transition, one can try to use this information to improve the trajectory with each iteration of the experiment. This

adaption mechanism can either be an estimation of model parameters to adjust the model to the observed system behaviour, or a direct modification of the trajectories by using a cost functional which contains measurable quantities. In the considered experiment, there are different measurements possible. Either the density distribution and fluctuations or the phase fluctuations can be extracted by using a time-of-flight method [10, 18]. These measurements give insight into local or global distributions and correlations.

1.4 Structure of this thesis

This work is structured as follows: In Chapter 2, a brief introduction to different models of a BEC is given. Two mean-field theories, namely the GPE and the npSE at zero temperature, are described in detail and the sGPE is discussed to prepare thermal initial states to study the BEC beyond the mean field at temperatures bigger than zero. Then, the optimal control problem for two different mathematical descriptions and cost functionals is presented with two different approaches for solving it. The first approach is an indirect optimisation approach (IOA), in which the search space for the optimal control variable is not limited, and the second one is a basis function approach (BFA). Optimal trajectories for both models are given for one QFTM sequence and compared to the simple protocol of linear trajectories. To overcome model-inaccuracies in the experiment and to introduce feedback into the system, a parameter estimator is designed in Chapter 4. In Chapter 5, the propagation of thermal initial states is used to study the evolution of fluctuations and to gain insight into the temperature evolution during the transitions. The trajectories that where optimised for the mean field are applied to the QFTM sequence at non-zero temperature and results are compared to simple linear transitions. A conclusion of this work and an outlook on possible extensions of the project are given in Chapter 6.

2 Mathematical description of BECs

In this chapter, an overview and brief introduction to different mathematical descriptions for Bose-Einstein condensates will be given. Those two, which are later used in this thesis will be explained in greater detail.

Strictly speaking, a BEC is a many-body system and every particle in it will have its own wave-function. In the Hamiltonian of such a system, the interaction between all pairs of atoms has to be described, which leads to N^2 terms in the many-body Hamiltonian, with N being the number of particles in the condensate [19]. At low temperatures, this very complex behaviour can be approximated up to different orders. The Gross-Pitaevskii equation (GPE) represents the lowest order of approximation. All particles are assumed to be in one single state and are described by the same quasi-particle wave-function $\Psi(\mathbf{r}, t)$, which is a classic field. In the three-dimensional space, $\Psi(\mathbf{r}, t)$ gives the expectation value of the true quantum field and thus the GPE is referred to as a mean-field theory. Thermal and quantum fluctuations, i.e. stochastics introduced due to finite temperature and quantum mechanics, are not described by such a mean-field theory. At nonzero temperature, the GPE can still be used as classical equation of motion for thermal initial states, which yields a description of the BEC that goes beyond mean-field theory.

The Hartree-Fock-Bogoliubov theory allows second-order terms in the Hamiltonian [20]. The field operator is split into a condensate (the classic field of the GPE) and a non-condensate (density and phase fluctuations). This results in equations of motion for the non-condensed part, which also couple to the classical field of the GPE. Linearisation of this semi-classical theory yields the Tomonaga-Luttinger Liquids model [16].

In the multi-configurational time-dependent Hartree method for Bosons (MCTDHB) [17, 21], the full many-body state is approximated by a set of ansatz functions. The ansatz functions can be viewed as states or orbitals, in which the atoms are distributed. Using only one orbital results in the GPE, and higher orbitals relate to states of higher energy. This method yields the evolution in time of the atom distribution in the orbitals, which are themselves time dependent. Because not all atoms are assumed to be in the ground state, many-body correlations can be studied up to different orders, depending on the number of orbitals used.

The uncertainty properties due to finite temperatures can also be mimicked by propagating multiple thermal initial states. Realisations of such thermal states can be sampled from a Wigner distribution [4] or using the stochastic GPE [16]. These sampled thermal initial states are subsequently propagated in using the classic GPE. The desired statistics such as density and phase fluctuations and correlations can then be calculated from the ensemble of all resulting wave-functions and give insight into the evolution of the temperature in the BEC.

2.1 Gross-Pitaevskii equation

When the temperature of a condensate goes to zero, all atoms can be described by one complex wave-function $\Psi(\mathbf{r}, t)$. The classical equation of motion called Gross-Pitaevskii equation (GPE)

$$i\hbar\partial_t\Psi(\mathbf{r}, t) = -\frac{\hbar^2}{2m}\Delta\Psi(\mathbf{r}, t) + V(\mathbf{r}, t)\Psi(\mathbf{r}, t) + g|\Psi(\mathbf{r}, t)|^2\Psi(\mathbf{r}, t) \tag{2.1}$$

describes the evolution of the mean-field wave-function $\Psi(\mathbf{r}, t)$ in the three-dimensional space and has the form of a nonlinear Schrödinger equation. Here, Δ is the three-dimensional Laplace operator, m is the mass of the atoms in the condensate, V is an external potential which confines the condensate and the coupling constant $g = 4\pi\hbar^2 a_s/m$ describes the coupling between particles with the s-scattering length a_s. The wave-function is normalized to the atom number N, i.e. $\int|\Psi(\mathbf{r})|^2 d\mathbf{r} = N$.

For normalisation, equation (2.1) is divided by $\hbar$, the wave-function is normalised to one, i.e. $\int|\tilde{\Psi}(\tilde{\mathbf{r}})|^2 d\tilde{\mathbf{r}} = 1$, $|\Psi|^2 = |\tilde{\Psi}|^2 N/\mu\text{m}$, time is measured in ms and space in µm. Inserting the normalisation

$$t = \tilde{t} \cdot 1\,\text{ms}, \ \partial_t = \partial_{\tilde{t}} \cdot \frac{1}{\text{ms}} \tag{2.2a}$$

$$z = \tilde{z} \cdot 1\,\text{µm}, \ \Delta = \tilde{\Delta} \cdot \frac{1}{\text{µm}^2} \tag{2.2b}$$

$$V = \hbar\tilde{V} \cdot \frac{1}{\text{ms}} \tag{2.2c}$$

$$m = \hbar\tilde{m} \cdot 1\frac{\text{ms}}{\text{µm}^2} \tag{2.2d}$$

$$\Psi = \tilde{\Psi} \cdot \sqrt{\frac{N}{\text{µm}}} \tag{2.2e}$$

in (2.1), we get the normalized GPE

$$i\partial_{\tilde{t}}\tilde{\Psi}(\tilde{\mathbf{r}}, \tilde{t}) = -\frac{1}{2\tilde{m}}\tilde{\Delta}\tilde{\Psi}(\tilde{\mathbf{r}}, \tilde{t}) + \tilde{V}(\tilde{\mathbf{r}}, t)\tilde{\Psi}(\mathbf{r}, \tilde{t}) + \tilde{g}|\tilde{\Psi}(\tilde{\mathbf{r}}, \tilde{t})|^2\tilde{\Psi}(\tilde{\mathbf{r}}, \tilde{t}) \tag{2.3}$$

with a new coupling constant $\tilde{g} = 4\pi\hbar N\tilde{a}_s/\tilde{m}$. Although this normalisation is used in every following equation, the tilde sign is dropped for convenience. If normalised to one, the absolute value $|\Psi(\mathbf{r}, t)|^2$ gives the probability of finding an atom at time t and place $\mathbf{r}$. The particle number now is no longer included in the normalisation of the wave-function but in the coupling constant.

Equation (2.1) describes the wave-function in the three-dimensional space. As mentioned in the introduction, the condensate in the experiment is confined tightly in transversal direction and cooled to a regime where it is valid to assume 1D dynamics. A variational ansatz for the transverse wave-function and integrating the transversal degrees of freedom leads to the normalised non-polynomial Schrödinger equation (npSE) [16]

$$i\partial_t\Psi(z, t) = -\frac{1}{2m}\partial_{zz}\Psi(z, t) + V(z, t)\Psi(z, t) + \omega_\perp\left(\frac{1 + 3a_s N|\Psi(z, t)|^2}{\sqrt{1 + 2a_s N|\Psi(z, t)|^2}} - 1\right)\Psi(z, t) \tag{2.4}$$

Symbol	Name	Value	Unit
m	mass	$1.443 \cdot 10^{-25}$	kg
$\omega_\perp$	transversal confinement	10.000	rad/ms
a_s	s-wave scattering length	$5.200 \cdot 10^{-3}$	µm
N	atom number in the BEC	$5.000 \cdot 10^3$	1
g_{1D}	coupling constant of the 1D-GPE	520	µm/ms

Table 2.1: Parameter values for the mean-field description of BECs used in this work.

for the classic field $\Psi(z, t)$ with the frequency $\omega_\perp$ of the harmonic confinement in transversal direction.

If $a_s N |\Psi(z, t)|^2 \ll 1$ (valid for small atom numbers), Taylor-series expansion allows to approximate the npSE with the one-dimensional GPE

$$i\partial_t \Psi(z, t) = -\frac{1}{2m}\partial_{zz}\Psi(z, t) + V(z, t)\Psi(z, t) + g_{1D}|\Psi(z, t)|^2\Psi(z, t), \qquad (2.5)$$

where the 1D coupling constant $g_{1D} = 2a_s\omega_\perp N$. When reducing the npSE to the 1D-GPE, terms of higher order in the Taylor-series expansion are neglected and a shift of the speed of sound [16] is introduced. In the npSE, this speed of sound is

$$c_{\text{npSE}}^2 = \omega_\perp a_s N \rho \frac{2 + 3a_s N\rho}{m(1 + 2a_s N\rho)^{3/2}}, \qquad (2.6)$$

while in die 1D-GPE it is

$$c_{\text{1D-GPE}}^2 = g_{1D}\rho/m, \qquad (2.7)$$

with $\rho = |\Psi(z, t)|^2$ being the 1D density. For the ground state of a box-shaped potential this 1D density is constant in the middle of the condensate. In the harmonic approximation and assuming such a homogenous condensate, the speed of sound in the GPE can be adapted to the npSE with an effective 1D coupling constant [16]

$$g_{\text{eff}} = \omega_\perp a_s N \frac{2 + 3a_s N\rho}{(1 + 2a_s N\rho)^{\frac{3}{2}}}. \qquad (2.8)$$

Parameters of the GPE and the npSE that are used in this work are given in Table 2.1.

2.2 Ground state of the GPE

To find the ground state of the GPE, the time-independent GPE

$$-\frac{1}{2m}\partial_{zz}\Psi_0(z) + V(z)\Psi_0(z) + g_{1D}|\Psi_0(z)|^2\Psi_0(z) = \mu\Psi_0(z) \qquad (2.9)$$

has to be solved. The chemical potential μ of the ground state is the energy needed to add one particle to the condensate. If the coupling constant g_{1D} is neglected, one has to solve a simple linear eigenvalue problem, which is the time-independent Schrödinger equation. The chemical potential corresponds to the eigenvalue and the ground state wave-function
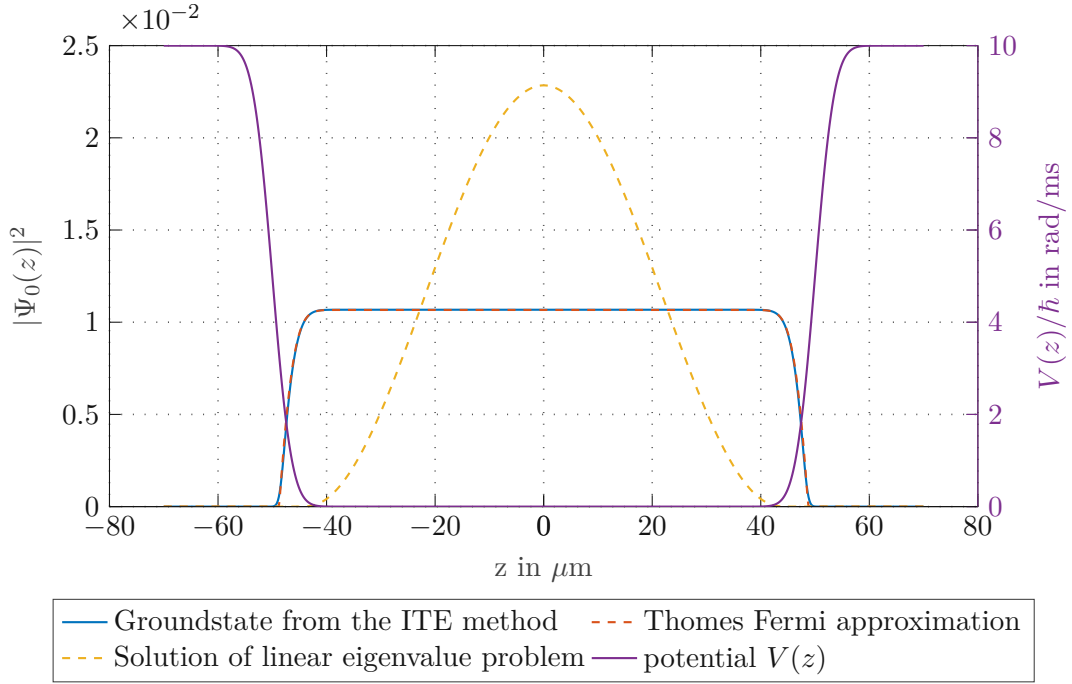
Figure 2.1: Comparison of different methods to calculate the ground state of the GPE for a box-shaped potential.

$\Psi_0(z)$ is the eigenvector of the smallest eigenvalue μ in this case. Another simplification can be found if the kinetic energy term $-\frac{1}{2m}\partial_{zz}\Psi_0(z)$ is neglected, while the non linearity is taken into account. This leads to the so called Thomas-Fermi approximation

$$\Psi_0(z) = \sqrt{\frac{\mu - V(z)}{g_{1D}}}. \tag{2.10}$$

In contrast to the properties of the linear eigenvalue problem, the chemical potential depends on the normalisation of the wave-function and is given by the normalisation condition $\int |\Psi_0(z)|^2 dz = 1$. A standard numerical method of solving the nonlinear problem (2.9) is propagating the 1D-GPE from some arbitrary initial density profile with a numerical solver using imaginary time-steps $\Delta t = -1i$, which is often referred to as imaginary time evolution (ITE) [22]. It introduces a dissipative effect and the wave-function will converge towards its lowest energy state. Notice that after every iteration the wave-function is renormalised. In Figure 2.1 a comparison of ground states obtained with different methods is given. Except for the edges of the condensate, (2.10) gives a good approximation for sufficiently high coupling constants. For the calculation of all further ground states, the imaginary time step method was used.

2.3 Moving solitons and numerical solutions of the GPE and the npSE

To validate numerical solvers of the GPE, an analytic solution is needed which can be compared to numerical results. Such an analytic solution is given for the propagation of bright solitons [23] with $V(z) = 0$. Inserting the ansatz

$$\Psi(z,t) = \Phi(z - ct)\mathrm{e}^{i\left(mcz - \frac{mc^2}{2}t - \mu t\right)} \tag{2.11}$$

in (2.5) and using the abbreviation $\zeta = z - ct$, results in the time-independent equation

$$\mu\Phi(\zeta) = -\frac{1}{2m}\frac{\mathrm{d}^2}{\mathrm{d}\zeta^2}\Phi(\zeta) + g_{1\mathrm{D}}|\Phi(\zeta)|^2\Phi(\zeta) \tag{2.12}$$

which can be solved to

$$\Phi(\zeta) = \sqrt{2\frac{|\mu|}{|g_{1\mathrm{D}}|}}\frac{1}{\cosh(\sqrt{2m|\mu|}\zeta)}. \tag{2.13}$$

The speed c of the moving soliton, which is not to be confused with the speed of sound in the GPE, is given by its initial state

$$\Psi(z,0) = \Phi(z)\mathrm{e}^{imcz}. \tag{2.14}$$

Numerical methods of solving the GPE can be classified into implicit or explicit finite-difference methods and solvers that use finite Fourier transformation or pseudospectral methods [24]. Two different numerical solvers, a Split-Step Fourier method and an implicit Crank-Nicolson scheme, are compared in this chapter. To convert the partial differential equation of the GPE or the npSE to a set of ordinary differential equations, a discrete grid with N_z spatial discretization points is applied. The spatial discretization was chosen as $\Delta x = \xi/10$, where $\xi = 1/\sqrt{2m\mu}$ is the healing length of the condensate, which also defines the characteristic length of solitonic solutions (2.12). The remaining temporal dynamics are then solved numerically according to the chosen solver.

Figure 2.2 shows the density evolution over time for a moving soliton. The analytic solution (2.11) is compared to the results of the Split-Step and the Crank-Nicolson solver. When the soliton approaches the edge of the spatial grid, both of the solvers will differ from the analytic solution because of the imposed boundary condition. The Crank-Nicolson solver reflects the soliton at the edges of the computational domain while the Split-Step solver has periodic boundary conditions and the soliton re-enters from the other side. These errors are not of interest in this work, since the potential V is later defined so that the condensate will never approach the edges of the computational domain. Furthermore, the Split-Step method introduces dispersion and the soliton dissolves with time, while the Crank-Nicolson scheme preserves the shape and energy of the soliton very well.

Figure 2.3 shows the computation time of both solvers and the distance to the numerical solution as a function of temporal step size, whereby the distance d asses the similarity between the numerical solution Ψ_{num} and the analytical solution Ψ_{ana} at $t = 2.5\,\mathrm{ms}$. The Crank-Nicolson scheme, as it is an implicit method, needs several iterations for solving

a nonlinear equation in each time step and therefore requires higher computation time than the explicit method. In some regimes, both of the solvers produce comparable small errors to the analytic result, but with step-sizes smaller than 0.5 ms, the Split-Step solver produces higher errors although the step size is decreased. This counterintuitive behaviour is typical for the Split-Step solver, since it is known to be sensitive to the ratio of spatial and temporal step size. The Crank-Nicolson method does get more precise with smaller time steps. To make sure not to choose an unfavourable ratio of spatial and temporal step size, the Crank-Nicolson solver was chosen for calculating the dynamics of the mean-field wave-function in this work. To calculate ground states, the Split-Step solver was used since it is computationally less expensive and the precise dynamics of the condensate are not of interest when calculating ground states. Note that the required spatial and temporal step-size depends on the healing length and the chemical potential of the condensate. The numerical solution of the GPE is a well known task and there already exist several implementations. In this work, the Matlab-toolbox OCTBEC [25] was used, which provides several different solvers.

To solve the npSE, the OCTBEC toolbox was extended with a Crank-Nicolson solver to calculate the dynamics of the npSE and with a Split-Step solver for the imaginary time method to calculate ground states. The result of the Crank-Nicolson solver for the npSE, starting from the initial state of a soliton as for the GPE results above, is shown in Figure 2.4. It can be seen that a soliton is not a stationary solution of the npSE and additional dispersion is introduced in comparison to the GPE [1]. Since there is no analytic solution of the npSE available to compare the numeric solution step sizes that produced good results in the GPE are also used for solving the npSE.

2.4 Stochastic Gross-Pitaevskii equation

As noted in Chapter 1, the GPE and the npSE describe the condensate at zero temperature. Also at nonzero temperature the evolution of the classic field during QTPs is nicely captured by these classic equations of motion. However, they do not include fluctuation due to thermal or quantum effects and designing a quantum thermal machine without a model that includes finite temperatures is clearly not reasonable. If we succeeded in optimising the transition parameters such that the condensate's classic field remains in the ground state at the end, there still is a need for advanced models to investigate the achieved energy transfer due to the whole cooling cycle or individual QTPs. The remaining degrees of freedom (e.g. the time of coupling, the strength of coupling, the compression ratio, or the number of cycles necessary to achieve sufficient cooling) have to be studied in a model that goes beyond mean-field approximations and is well suited to handle thermal states. In this work, a sampled approach is used, where a number of thermal initial states (TISs) are drawn to include fluctuation due to finite temperatures. These thermal states are then propagated with the GPE or the npSE and stochastic properties are calculated from the resulting ensemble. To sample TISs, one could draw initial states from the Wigner

---

[1]This dispersion depends on the chosen parameters, i.e. the chemical potential and the speed of the soliton. Furthermore, this observed dispersion might be less present for dark solitons since the difference between the npSE and the 1D-GPE is larger for higher densities.
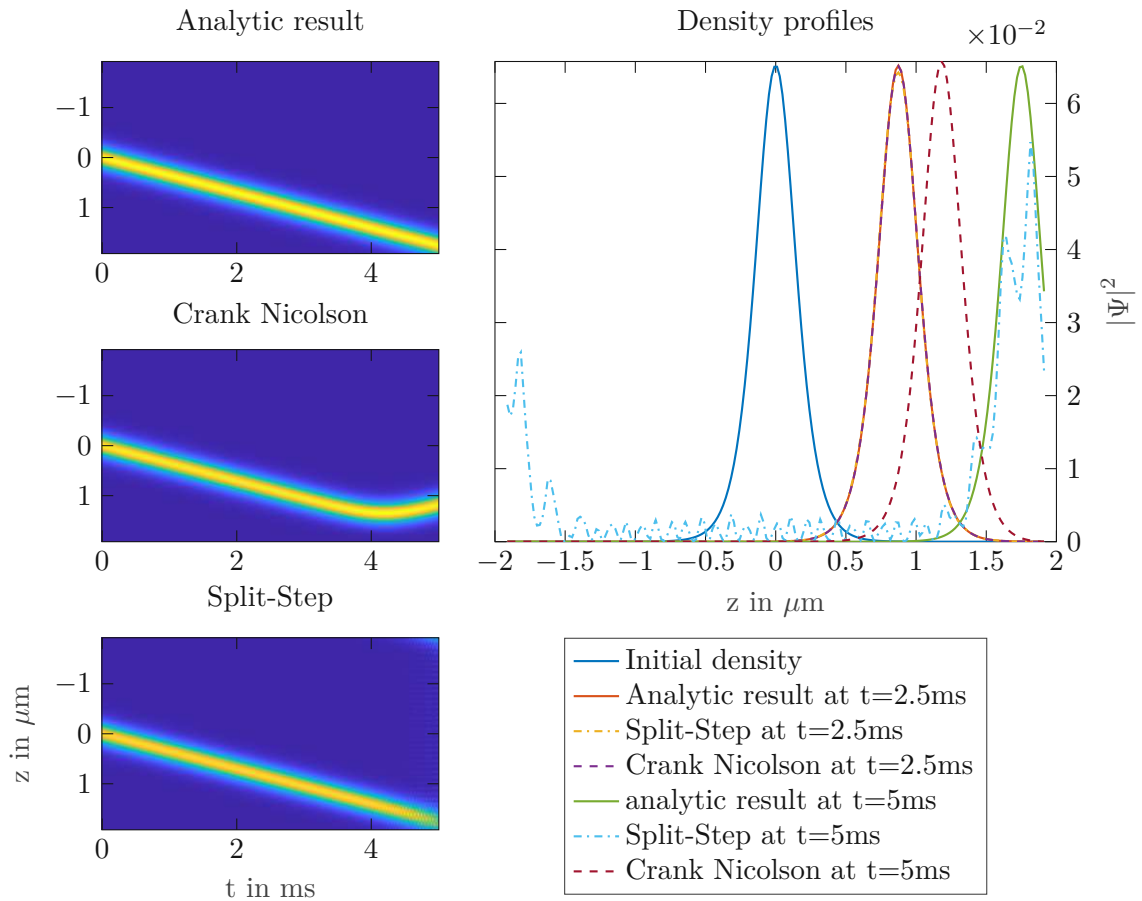
Figure 2.2: Carpet plot of the analytic solution (2.11) of a moving soliton in comparison to the numeric result with the Crank-Nicolson scheme and the Split-Step method. The density profiles on the right side are given at two points in time.
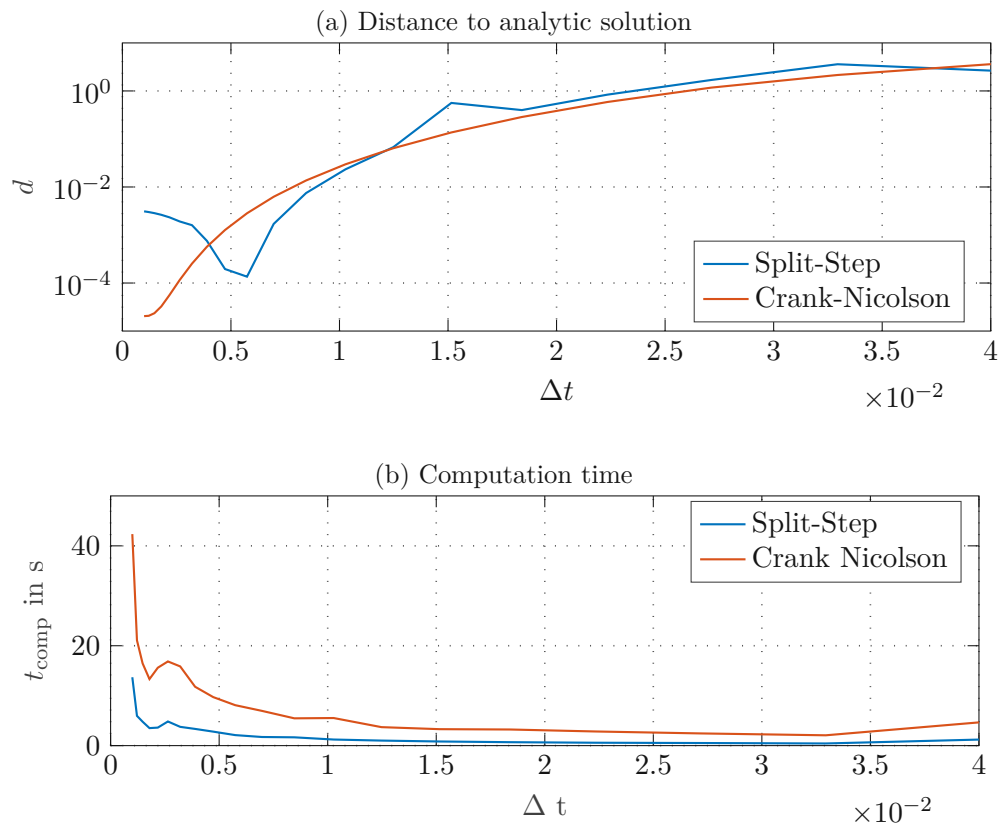
Figure 2.3: Error and computation time of two different numerical solvers for the GPE, plotted over the temporal step size Δt of the solvers. The numerical solution of a moving soliton is compared to the analytical solution (2.11) at $t = 2.5\,\mathrm{ms}$ and the computation time is evaluated for a simulation-time of $5\,\mathrm{ms}$ Above: The distance $d = \frac{1}{2}\big(1 - |\langle\Psi_{\mathrm{ana}}, \Psi_{\mathrm{num}}\rangle|^2\big)$ assesses the error to the analytical solution and is defined so that it is zero if Ψ_{num} and Ψ_{ana} are identical. The numerical solutions Ψ_{num} obtained with two different solvers of the GPE are compared to the analytic solution Ψ_{ana} of a moving soliton (2.11). Below: Computation time t_{comp} for the numerical solution of the GPE.
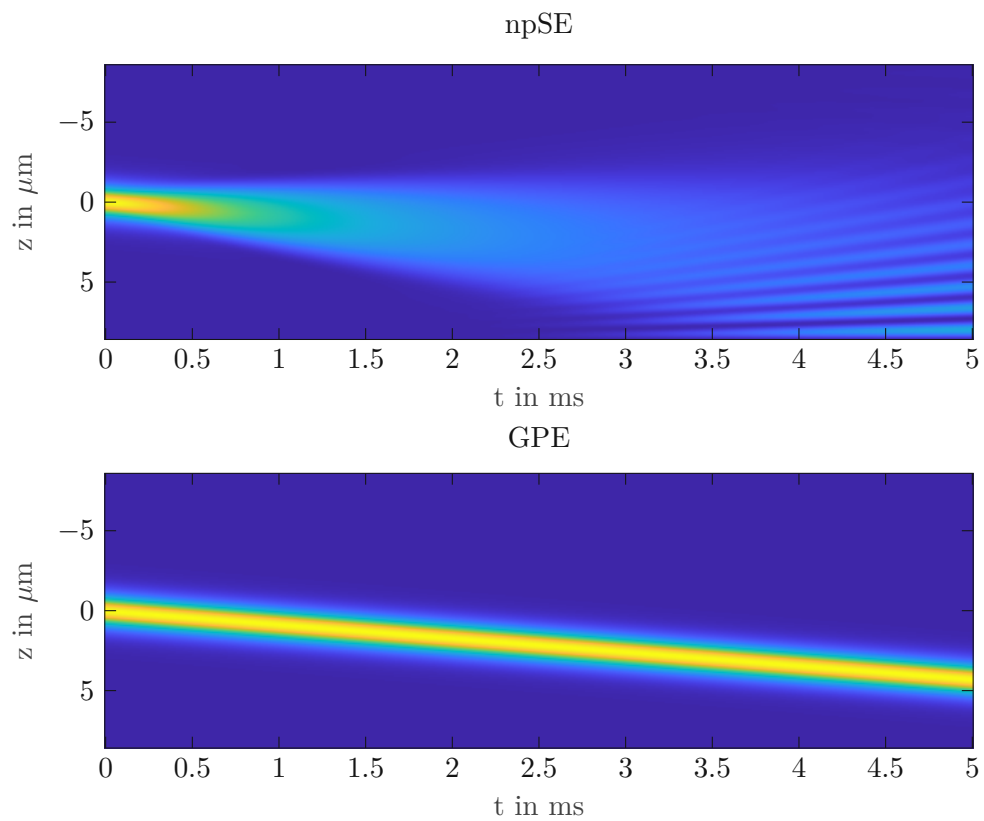
Figure 2.4: Density evolution over time of a moving soliton in the npSE and in the GPE. For both results, a Crank-Nicolson solver was used.

function, which is the Weyl transform of the density matrix [16]. The latter method requires the non-trivial task of solving Bogoliubov equations to obtain ansatz functions of the thermal state. An alternative method of sampling TISs uses the stochastic GPE (sGPE), which is chosen in this work. The sGPE is a Langevin type of equation [26], like the equation that describes the Brownian motion of a particle in a liquid. Such equations are derived from a fluctuation-dissipation theorem, whereby the strength of the fluctuations, introduced by a noise term, and the strength of dissipation, introduced by a damping term, are balancing each other.

In the (normalised) sGPE

$$
i\partial_t \Psi(z,t) = (1 - i\gamma)\left[-\frac{1}{2m}\Delta\Psi(z,t) + V(z,t)\Psi(z,t) + g_{1\mathrm{D}}|\Psi(z,t)|^2\Psi(z,t) - \mu \right] + \eta,
$$
(2.15)

the noise term η is complex Gaussian white noise, which introduces a stochastic drive. It is not correlated in space and time and has a variance of $\sigma_\eta = 2\gamma \mathrm{k_B}T/(\hbar \cdot 10^3\,\mathrm{rad/s})$. The desired temperature of the TISs is defined by T and $\mathrm{k_B}$ denotes Boltzmann's constant. The parameter γ in the sGPE on the other hand has a damping effect. The variance σ_η also depends on γ, which introduces the balancing effect that was mentioned above. As the sGPE is only used as growth sGPE to obtain thermal initials, γ is a parameter which, within some limits, does not effect the resulting thermal initial states, but influences the convergence of the sGPE. The chemical potential μ is determined beforehand by the calculation of the mean-field ground state as described in Section 2.2. Note that by determining the chemical potential we define the mean value of $\int |\Psi(z)|^2\,\mathrm{d}z$ to one but allow fluctuations in the atom number[2].

To sample a number of M thermal initial states Ψ_i^th, the sGPE is propagated M-times, starting from an empty condensate. The condensate gets increasingly occupied over time due to the noise term η and coherent growth due to the $-i\gamma[\ldots]$ term. As numerical solver the Split-Step method was used with a time discretization of $\Delta t = 0.05\,\mathrm{ms}$. Since we only use the sGPE to draw samples of stationary thermal states, the choice of the step size is completely arbitrary and the amount of noise added in each iteration can be tuned with the damping parameter γ. The product $\Delta t\gamma$ sets the growth of the convergence values. For example, to obtain TISs with a temperature of $50\,\mathrm{nK}$, γ was set to 0.1 to reach fast convergence without extremely high noise terms. Convergence can be checked by looking at the atom number, the global density fluctuation and the phase correlation [16]. The mean value of the (normalised) atom number is given by

$$
\bar{N} = \frac{1}{M}\sum_{i=1}^{M} N_i,
$$
(2.16a)

with

$$
N_i = \int |\Psi_i^\mathrm{th}(z)|^2\,\mathrm{d}z,
$$
(2.16b)

---

[2]The chemical potential μ in (2.15) depends on the temperature of the thermal state, which can be taken into account by iteratively renormalising the thermal initials to a desired mean atom number, evaluating the new chemical potential and correcting it in the sGPE. This effect is almost negligible in this work and small deviations in the resulting mean atom number where corrected once at the end of the sGPE propagation.

whereby $\bar{N}$ is expected to converge towards one. Global density fluctuations are calculated as the sample variance

$$\delta\rho(z) = \int \frac{1}{M-1} \sum_{i=1}^{M} \Big(|\Psi_i^{\text{th}}(z)|^2 - \bar{\rho}(z) \Big)^2 \, \mathrm{d}z, \tag{2.17a}$$

with the mean density

$$\bar{\rho}(z) = \frac{1}{M} \sum_{i=1}^{M} |\Psi_i^{\text{th}}(z)|^2 \tag{2.17b}$$

and the phase correlation is given by

$$C(z, z') = \frac{1}{M} \sum_{i=1}^{M} \cos\Big(\arg(\Psi_i^{\text{th}}(z)) - \arg(\Psi_i^{\text{th}}(z')) \Big). \tag{2.18}$$

To introduce an averaging effect and to check for convergence and validity of the thermal state, the phase correlation is integrated over diagonal lines (plotted as black dots in the phase correlation of Figure 2.6). This integrated phase correlation is written as

$$C_D(\Delta z) = \int C(z, z + \Delta z) \, \mathrm{d}z. \tag{2.19}$$

For a homogenous condensate in thermal equilibrium this phase correlation should decay exponentially with the thermal coherence length $\lambda_c = 2\hbar^2 \rho / (mk_bT)$, [16], which gives the analytic result

$$C_D^{\text{ana}}(\Delta z) = \mathrm{e}^{-\frac{\Delta z}{\lambda_c}}. \tag{2.20}$$

Note that the normalised coherence length $\tilde{\lambda}_c = 2\tilde{\rho}N/(\tilde{m}\tilde{T})$, with $\tilde{T} = k_bT/(\hbar \cdot 10^3 \, \text{rad/s})$, is given in µm consistently with the normalisation (2.2). In the considered box condensates, the phase correlation is calculated in the middle of the condensate, where it is quasi homogenous.

The number of iterations needed for the thermal state to converge depends on the desired temperature, whereby the mean particle number and the density fluctuations typically converge faster than the phase correlation. Furthermore, the number of samples, which is necessary to obtain TISs with correct stochastic properties, depends on the desired temperature. For 50 nK, 500 TISs where calculated, with each of them needing 6000 iterations of the sGPE. To check and improve convergence of the phase correlation, another 3000 iterations of the GPE where performed.

Figure 2.5(a) shows the density of ten of the resulting TISs for a box potential. The mean of all 500 density profiles can be seen in Figure 2.5(b). With increasing number of sampled states, this mean density converges to a smooth box shape.

The phase correlation and the integrated phase correlation of the resulting TISs is shown Figure 2.6. Outside the box, the density is zero apart from some remaining noise, which explains the vanishing correlations $C(z, z')$ for $|z| < 50$. The line over which is integrated to obtain $C_D(\Delta z)$ is drawn as dashed line for $\Delta z = 0 \, \text{µm}$ and $\Delta z = 20 \, \text{µm}$ in Figure 2.6. The integrated phase correlation nicely fits the analytic result (2.20) with a coherence length of $\lambda_c = 13.17 \, \text{µm}$. The convergence of the atom number, the global

density fluctuations and the integrated phase correlation at $\Delta z = 10\,\mu\text{m}$ are shown in Figure 2.7. Comparing all three convergence values, the atom number (defined by setting the chemical potential according to the GPE ground states) is the first value to converge, followed by the global density fluctuation. Clearly, obtaining TISs with correct phase correlations requires the largest number of iterations and a particularly high number of samples.

(a) Densities of the first 10 thermal initial states

(b) Comparison of the mean density of TISs and GPE ground state
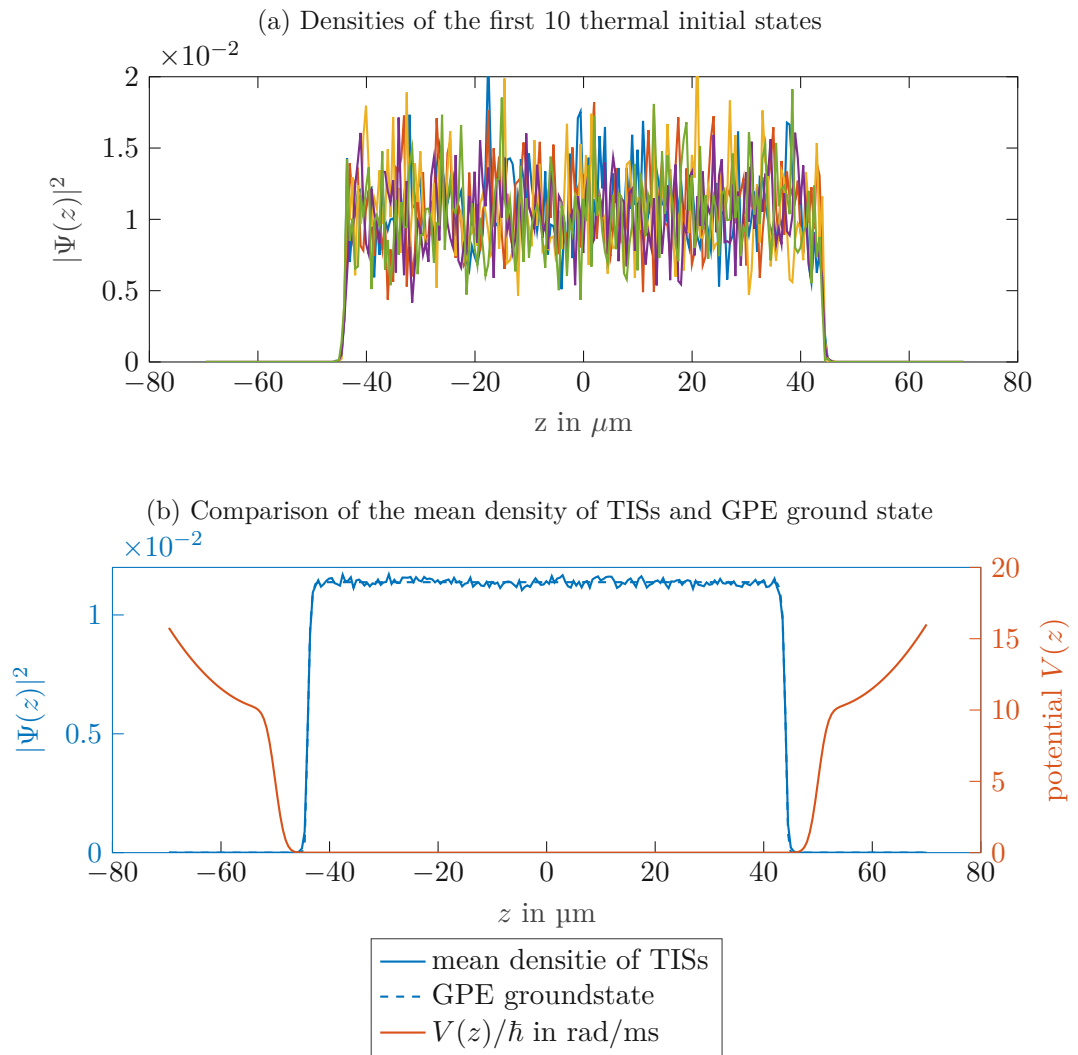
Figure 2.5: Density profiles of resulting TISs. 100 samples where calculated by solving the sGPE (2.15) with a desired temperature of $T = 50\,\text{nK}$ and $\gamma = 0.1$.

(a) Phase correlation $C(z, z')$ (b) Integrated phase correlation
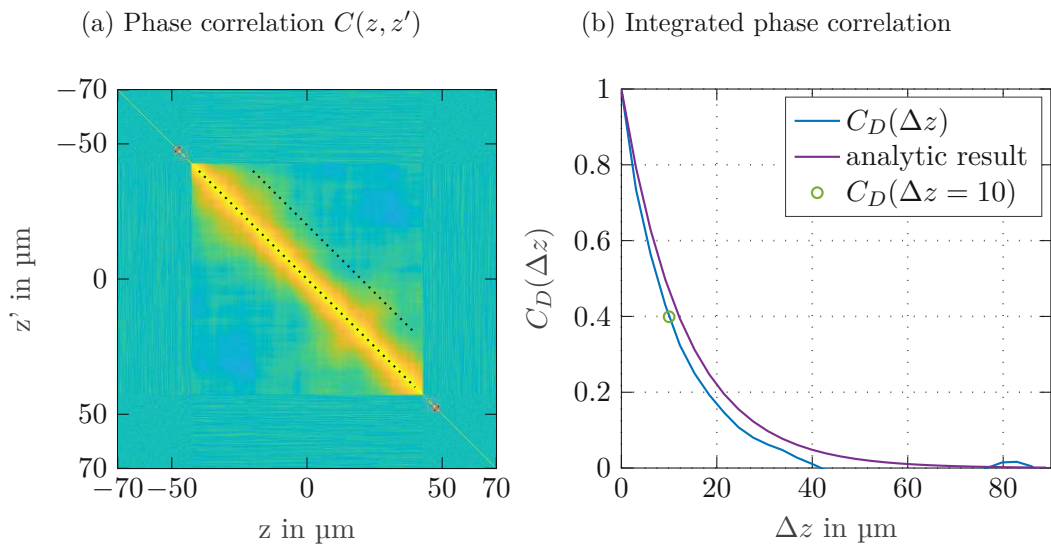
Figure 2.6: Phase correlation properties (2.18) of sampled TISs after convergence. To check the validity of the TISs, the integrated phase correlation (2.19) is compared to the analytic result of (2.20).

(a) Convergence of atom number (2.16) of three thermal initial states.

(b) Convergence of the global density fluctuation (2.17)

(c) Convergence of $C_D(\Delta z)$ at $\Delta z = 10\,\mu\mathrm{m}$
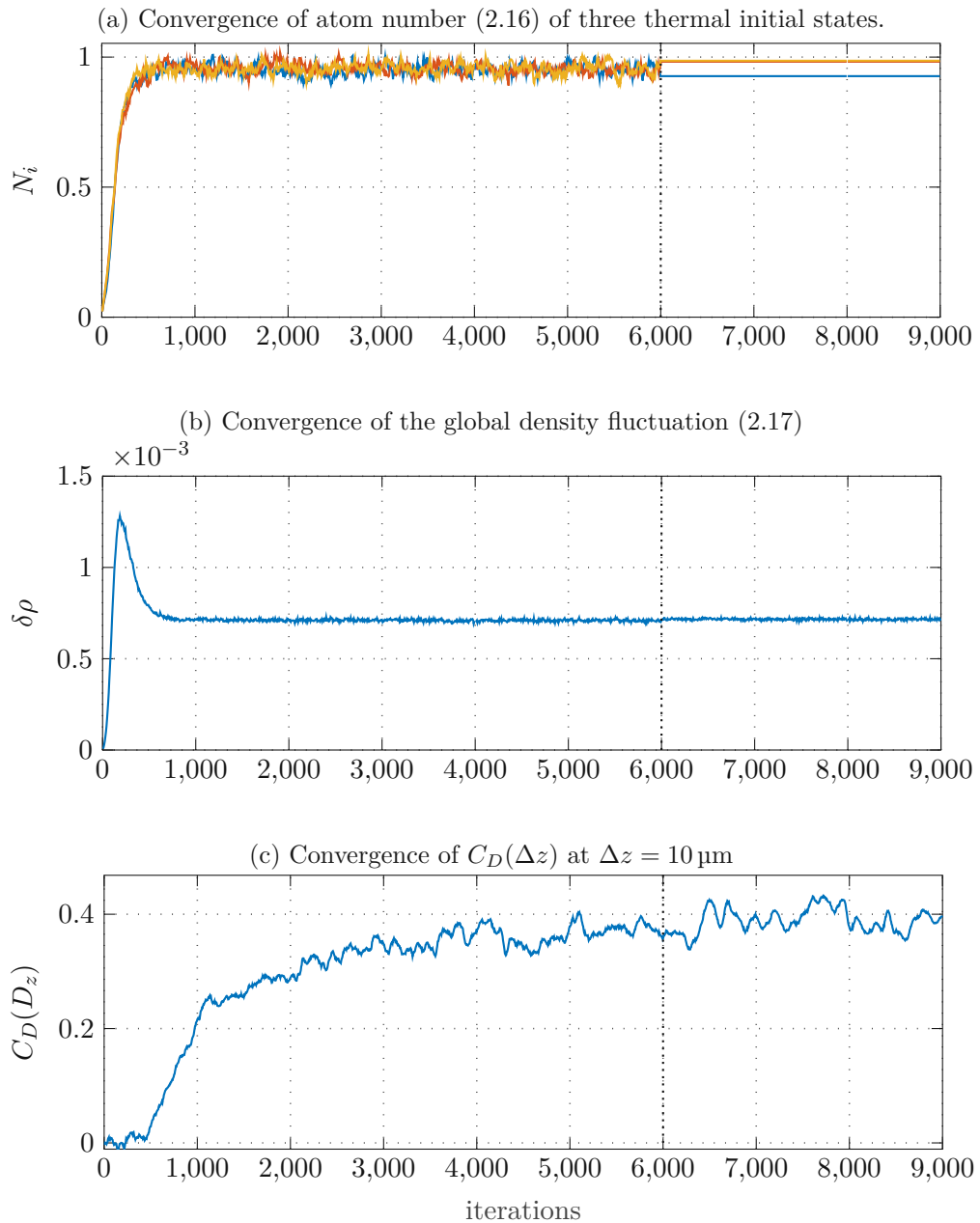
Figure 2.7: Convergence of stochastic properties of the TISs to check the TISs validity. 500 TISs are calculated with the sGPE (2.15). After 6000 iterations of the sGPE, another 3000 iterations of the GPE are performed. During the sGPE iterations, the atom number fluctuates but then stays constant for the last 3000 iterations since the GPE preserves the atom number of the condensate. The atom number and the global density fluctuations converge within 1000 iterations. To obtain correct phase correlation properties, many more iterations and a high number of sampled TISs are necessary.

3 Optimal control of the mean field in quantum thermal primitives

The application of optimal control theory (OCT) on BECs has been investigated in a number of contributions. In [11], optimal control of BECs in magnetic micro traps is studied using the GPE as model and optimal transitions are provided for splitting the condensate and shifting its position. They utilize simple parabolic potentials and more realistic descriptions of magnetic micro traps as the magnetic confinement of Hänsel [27] and Lesanovsky [28].

In [13], condensate splitting and squeezing in magnetic micro traps is explored in the generic two-mode model [29] for a more transparent picture of the dynamics and in the more elaborated MCDTHB model [17], which is formally a quantum-mechanically correct description of the many-body dynamics.

Optimisation for the 3D GPE is investigated in [12], where they calculate optimal trajectories for a 3D compression in a parabolic potential, for loading a toroidal trap and for splitting the condensate in two parts.

The problem of finding an optimal trajectory of some input variable or control parameter is called dynamic optimisation problem. There are two main approaches to solve such an optimisation problem. All of the above mentioned contributions follow an indirect optimisation approach (IOA), where the calculus of variations is used to formulate first-order optimality conditions. These optimality conditions are written as a set of equations (also referred to as optimality system) and define a boundary value problem, which has to be solved to obtain optimal trajectories. This approach does not restrict the search space for the optimal trajectory, but one has to put effort in deriving and solving the optimality conditions and the calculation of the gradient can be computationally expensive. For a direct approach, the input quantity is discretised or composed of a finite number of basis functions. If these basis functions are chosen wisely, the basis function approach (BFA) typically results in a lower number of parameters to optimise. With a direct approach, the dynamic optimisation problem is turned into a static optimisation problem, which can be solved with gradient-based or non-gradient-based methods. If a method is chosen which does not require a gradient, a BFA can also be executed directly on an experiment without model knowledge and can contain any measurable quantity. In [30], a BFA is combined with the randomisation of the basis functions and named Chopped Random Basis (CRAB).

In this chapter, a short introduction to optimal control approaches suited for BECs is given, the optimality conditions for the GPE are presented and then the equations for the npSE are derived. As illustrative problem, the compression of a condensate in a box potential, which is one of the QTPs described in Chapter 1, is explored in greater detail. The results of a BFA are compared to those of a IOA. Differences in the GPE and the

npSE are discussed for a less drastic compression and a more drastic one.

3.1 Formulation of the optimal control problem

The aim of optimal control is to find the trajectory (i.e. a function in time) of some input quantity of a system which produces an optimal result. The input quantity in this work is the control parameter $\lambda(t)$, $t \in [0, T_t]$, which is element of a suitable function space $\mathcal{V}$ and parametrises a transition of the external potential $V(z, t) = V(z, \lambda(t)) = V_\lambda(z)$. The transition starts at $t = 0$ and ends at the fixed end time $t = T_t$ while the potential is transformed from an initial to a final shape. The subscript of the external potential highlights the dependence on the control parameter. The mean-field wave-function $\Psi(z, t)$ is the state variable of the system and the initial wave-function is assumed to be the ground state of the initial potential $V(z, 0)$. To minimise excitations after the transition, the optimal final state should be the ground state of the final potential $V(z, T_t)$. The optimality of a transition is evaluated with a cost functional $J : \mathcal{V} \to \mathbb{R}$ of the form

$$J(\lambda) = \phi(T_t, \Psi(z, T_t)) + \int_0^{T_t} \mathrm{l}(t, \Psi(z, t), \lambda(t)) \, \mathrm{d}t, \tag{3.1}$$

with the terminal costs $\phi(T_t, \Psi(T_t))$ at the end of the transition, and the integral costs $\mathrm{l}(t, \Psi(z, t), \lambda(t))$ during the transition. As constraints to the optimisation problem, the state equation (i.e. the differential equations which describe the system's behaviour), the initial conditions for the wave-function and boundary conditions for the control parameter are added and the full optimisation problem is formulated as

$$\min_{\lambda(\cdot)} J(\lambda) \tag{3.2a}$$

$$\text{s.t. } \partial_t \Psi(z, t) = f(\Psi(z, t), \lambda(t)), \qquad \Psi(z, 0) = \Psi_0(z) \tag{3.2b}$$

$$\lambda(0) = \lambda_0, \ \lambda(T_t) = \lambda_T \tag{3.2c}$$

In principle, the system function f can be any model that describes the experiment. Since we are interested in mean-field solutions in this chapter, the optimal control problem is formulated for the GPE and for the npSE. Details of the mathematical description of BECs are given in Chapter 2.

3.2 Numerical solution of the optimal control problem

As mentioned above, there exist several approaches to find the optimal solution for $\lambda(t)$. In a BFA, the search space of $\lambda(t)$ is restricted from the beginning and the problem is turned into a finite-dimensional optimisation problem. Alternatively, the gradient can be calculated directly from the optimality conditions via functional derivatives without limiting the search space, which is the approach followed in an IOA.

3.2.1 Indirect optimisation approach (IOA)

To find the optimal trajectory $\hat{\lambda}(t)$[1] without restricting the search space, one has to calculate the functional derivative (or Gateaux derivative) of J with respect to the control parameter using calculus of variations. This functional derivative is defined as

$$\delta J(\lambda; \xi_\lambda) = \frac{\mathrm{d}}{\mathrm{d}\nu} J(\lambda + \nu \xi_\lambda)|_{\nu=0} \tag{3.3}$$

where $\xi_\lambda \in \mathcal{V}$ is a variation of λ. At the minimum of J, this functional derivative has to meet the first-order optimality condition $\delta J(\hat{\lambda}; \xi_\lambda) = 0$ for all admissible variations ξ_λ regarding the boundary conditions (3.2c). Note that the cost functional J depends on the wave-function $\Psi = \Psi(z, t)$ and the dependence of the wave-function on the control parameter is defined by the equations describing the system dynamics.

A commonly used approach to calculate $\delta J(\lambda; \xi_\lambda)$ is the introduction of the Lagrange functional

$$L(\lambda, \Psi, p) = \phi(T_t, \Psi(z, T_t)) + \int_0^{T_t} l(t, \Psi(z, t), \lambda(t)) \, \mathrm{d}t + \tag{3.4}$$
$$+ \mathrm{Re}\left(\int_0^{T_t} \int p^*(z, t)(\partial_t \Psi(z, t) - f(\Psi(z, t), \lambda(t))) \, \mathrm{d}z \, \mathrm{d}t \right),$$

that uses the system's state equation $\partial_t \Psi(z, t) = f(\Psi(z, t), \lambda(t))$ with the adjoint variable $p = p(z, t)$ [31]. With this definition, $\delta J(\lambda; \xi_\lambda)$ is now equal to the partial functional derivative $\delta_\lambda L((\lambda, \Psi, p); \xi_\lambda)$ if the conditions $\delta_p L((\lambda, \Psi, p); \xi_p) = 0$ and $\delta_\Psi L((\lambda, \Psi, p); \xi_\Psi) = 0$ are met for all admissible variations of ξ_p and ξ_Ψ, which are variations of the adjoint variable and the wave-function. This relation can be seen in the expansion

$$\delta J(\lambda; \xi_\lambda) = \delta_\lambda J(\lambda, \Psi; \xi_\lambda) + \delta_\Psi J(\lambda, \Psi; \xi_\Psi)|_{\xi_\Psi = \delta \Psi(\lambda; \xi_\lambda)}, \tag{3.5a}$$

where the derivative of the wave-function with respect to the control parameter $\delta \Psi(\lambda; \xi_\lambda)$ is derived by differentiating the state equation with respect to the control parameter

$$\partial_t \delta \Psi(\lambda; \xi_\lambda) = \frac{\partial}{\partial \Psi} f(\Psi, \lambda) \delta \Psi(\lambda; \xi_\lambda) + \frac{\partial}{\partial \lambda} f(\Psi, \lambda) \xi_\lambda \tag{3.5b}$$

considering the initial condition

$$\delta \Psi(\lambda; \xi_\lambda)|_{t=0} = 0. \tag{3.5c}$$

Setting the partial functional derivatives of (3.4) with respect to λ, Ψ and p to zero results in a set of differential equations with initial and final conditions, which is also called optimality system and defines the first-order optimality condition.

Regarding the cooling sequences described in Chapter 1, the condensate should reach the initial ground state again after one cycle within a mean-field description. For each quantum thermal primitive on its own, the most obvious goal is reaching the ground

---

[1]Variables at the optimum are marked with a hat, which is not to be confused with operators in the Dirac notation.

state after each transition, according to the final configuration of the potential, so that no mean-field excitations are remaining. In this work, two different cost functionals are investigated to reach the goal of minimising mean-field excitations. The state-trapping cost functional, or short state cost,

$$J_{\text{state}} = \frac{1}{2}\left(1 - \left|\int \Psi_{\text{des}}^*(z)\Psi(z, T_t)\,\mathrm{d}z\right|^2\right) + \frac{\gamma_{\text{reg}}}{2}\int_0^{T_t}(\partial_t\lambda(t))^2\,\mathrm{d}t \qquad (3.6)$$

evaluates the difference between the obtained final state $\Psi(z, T_t)$ and the desired state $\Psi_{\text{des}}(z)$, which is the ground state of the final configuration of the external potential in this work. The term $\frac{\gamma_{\text{reg}}}{2}\int_0^{T_t}\partial_t(\lambda(t))^2\,\mathrm{d}t$ penalizes strong variations of $\lambda(t)$ and improves convergence. Alternatively, the energy of the obtained final state can be evaluated using the energy cost functional for the normalised 1D-GPE

$$J_{\text{energy}}^{\text{GPE}} = \int \Psi^*(z, T_t)\left(-\frac{1}{2m}\partial_{zz} + V_\lambda(z, T_t) + \frac{g_{\text{1D}}}{2}|\Psi(z, T_t)|^2\right)\Psi(z, T_t)dz -$$
$$- J_{\text{des}}^{\text{GPE}} + \frac{\gamma_{\text{reg}}}{2}\int_0^{T_t}(\partial_t\lambda(t))^2\,\mathrm{d}t, \qquad \gamma_{\text{reg}} > 0 \qquad (3.7)$$

whereby $J_{\text{des}}^{\text{GPE}}$ is the energy of the desired ground state

$$J_{\text{des}}^{\text{GPE}} = \int \Psi_{\text{des}}^*(z)\left(-\frac{1}{2m}\partial_{zz} + V_\lambda(z, T_t) + \frac{g_{\text{1D}}}{2}|\Psi_{\text{des}}(z)|^2\right)\Psi_{\text{des}}(z)dz. \qquad (3.8)$$

This energy cost originates from the Hamiltonian for the 1D-GPE. This desired energy will always be smaller than the achieved energy, since the ground state is defined as the state of smallest energy.

For the npSE, this energy cost reads as

$$J_{\text{energy}}^{\text{npSE}} = \int \Psi^*(z, T_t)\left(-\frac{1}{2m}\partial_{zz} + V_\lambda(z, T_t) - \mu + \omega_\perp\sqrt{1 + 2a_sN|\Psi(z, t)|^2}\right)\Psi(z, T_t)dz -$$
$$- J_{\text{des}}^{\text{npSE}} + \frac{\gamma_{\text{reg}}}{2}\int_0^{T_t}(\partial_t\lambda(t))^2\,\mathrm{d}t, \qquad \gamma_{\text{reg}} > 0 \qquad (3.9)$$

with

$$J_{\text{des}}^{\text{npSE}} = \int \Psi_{\text{des}}^*(z, T_t)$$
$$\left(-\frac{1}{2m}\partial_{zz} + V_\lambda(z, T_t) - \mu + \omega_\perp\sqrt{1 + 2a_sN|\Psi_{\text{des}}(z, t)|^2}\right)\Psi_{\text{des}}(z, T_t)dz. \quad (3.10)$$

If the desired final state is the ground state, which by definition is the state of lowest energy, both the state and the energy cost functionals have the global minimum at the same value of wave-function and control parameter. Convergence behaviour of the two cost functionals can still differ substantially and local minima might not be the same, as shown in Section 3.4. Obviously, the desired state, the cost values and optimal solutions are not the same for the GPE and the npSE. When the GPE is used as mathematical

description for the system, the resulting first-order optimality conditions for the state cost, as derived in [31], are

$$i\partial_t \hat{\Psi}(z,t) = \left(-\frac{1}{2m}\Delta + V_{\hat\lambda}(z,t) + g_{1D}|\hat\Psi(z,t)|^2 \right)\hat\Psi(z,t) \tag{3.11a}$$

$$i\partial_t \hat{p}(z,t) = \left(-\frac{1}{2m}\Delta + V_{\hat\lambda}(z,t) + g_{1D}|\hat\Psi(z,t)|^2 \right)\hat{p}(z,t) + g_{1D}\hat\Psi(z,t)^2 \hat{p}^*(z,t) \tag{3.11b}$$

$$\gamma_{\mathrm{reg}}\partial_{tt}\hat\lambda = -\mathrm{Re}\int_\Omega \hat\Psi^*(z,t)\frac{\partial V_\lambda}{\partial\lambda}|_{\lambda=\hat\lambda(t)}p(z,t)\,\mathrm{d}z \tag{3.11c}$$

$$\hat\Psi(z,0) = \Psi_0(z) \tag{3.11d}$$

$$\hat{p}(z,T_t) = i\int \Psi^*_{\mathrm{des}}(z)\hat\Psi(z,T_t)\,\mathrm{d}z\Psi_{\mathrm{des}}(z) \tag{3.11e}$$

$$\lambda(0) = \lambda_0, \qquad \lambda(T_t) = \lambda_T \tag{3.11f}$$

If the energy cost (3.7) is used, the final condition of the adjoint variable changes to

$$\hat{p}(z,T_t) = -2i\left(-\frac{1}{2m}\Delta + V_{\hat\lambda}(z,T_t) + g_{1D}|\hat\Psi(z,T_t)|^2 \right)\hat\Psi(z,T_t). \tag{3.12}$$

Since the 1D-GPE is an approximation of the npSE (2.4), which describes the quasi condensate of the experiment more accurately, the IOA is also studied for the npSE in this work. For the npSE, the derivation of the optimality system is done in the same way as for the GPE. All required equations are briefly discussed in the following paragraphs.

In the first step, the npSE is rewritten as

$$\partial_t\Psi(z,t) = f_{\mathrm{npSE}}(\Psi,\lambda) \tag{3.13a}$$

$$f_{\mathrm{npSE}}(\Psi,\lambda) = -i\Bigg[-\frac{1}{2m}\partial_{zz}\Psi(z,t) + V_\lambda(z,t)\Psi(z,t) +$$
$$+ \omega_\perp\left(\frac{1 + 3a_sN|\Psi(z,t)|^2}{\sqrt{1+2a_sN|\Psi(z,t)|^2}} + 1 \right)\Psi(z,t) \Bigg]. \tag{3.13b}$$

For the state cost, the partial functional derivative of the Lagrange functional with respect to Ψ results in

$$\delta_\Psi L((\lambda,\Psi,p);\xi_\Psi) = \mathrm{Re}\left(\int\int \Psi^*_{\mathrm{des}}(z)\Psi(z,T_t)\,\mathrm{d}z\Psi^*_{\mathrm{des}}(z)\xi_\Psi(z,T_t)\,\mathrm{d}z \right) + \tag{3.14}$$
$$+ \mathrm{Re}\left(\int_0^{T_t}\int p^*(z,t)(\partial_t\xi_\Psi(z,T_t) - \delta_\Psi f_{\mathrm{npSE}}(\Psi,\lambda;\xi_\Psi))\,\mathrm{d}z\,\mathrm{d}t \right)$$

where

$$i\delta_\Psi f_{\text{npSE}}(\Psi, \lambda; \xi_\Psi) = -\frac{1}{2m}\partial_{zz}\xi_\Psi(z,t) + V_\lambda(z,t)\xi_\Psi(z,t) + \tag{3.15}$$

$$+ \omega_\perp\left(\frac{1 + 3a_sN|\Psi(z,t)|^2}{\sqrt{1 + 2a_sN|\Psi(z,t)|^2}} + 1\right)\xi_\Psi(z,t) +$$

$$+ \omega_\perp 3a_sN\frac{\Psi^*(z,t)\xi_\Psi(z,t) + \Psi(z,t)\xi_\Psi^*(z,t)}{\sqrt{1 + 2a_sN|\Psi(z,t)|^2}}\Psi(z,t) -$$

$$- \omega_\perp 2a_sN\frac{1}{2}\frac{1 + 3a_sN|\Psi(z,t)|^2}{(1 + 2a_sN|\Psi(z,t)|^2)^{\frac{3}{2}}}\left(\Psi^*(z,t)\xi_\Psi(z,t) + \Psi(z,t)\xi_\Psi^*(z,t)\right)\Psi(z,t).$$

Considering the initial condition of the wave-function and assuming that the external potential at the boundaries of the spatial domain Ω is sufficiently high, the conditions $\xi_\Psi(z,0) = 0$ and $\xi_\Psi(z,t) = \partial_z\xi_\Psi(z,t) = 0 \,\forall z \in \partial\Omega$ are met for all admissible variations. By using partial integration, (3.14) can be rewritten as

$$\delta_\Psi L((\lambda, \Psi, p); \xi_\Psi) = \tag{3.16}$$

$$\text{Re}\left(\int\int \Psi_{\text{des}}^*(z)\Psi(z,T_t)\,\mathrm{d}z\Psi_{\text{des}}^*(z)\xi_\Psi(z,T_t) + p^*(z,T_t)\xi_\Psi(z,T_t)\,\mathrm{d}z\right) +$$

$$+ \text{Re}\left(\int_0^{T_t}\int -\partial_t p^*(z,t)\xi_\Psi(z,T_t) - i\frac{1}{2m}\partial_{zz}p^*(z,T_t)\xi_\Psi(z,t) + iV_\lambda(z,t)p^*(z,t)\xi_\Psi(z,t) +\right.$$

$$\left. + ip^*(z,T_t)A(\Psi)\xi_\Psi(z,t) + ip^*(z,T_t)B(\Psi)\xi_\Psi^*(z,t)\right)\,\mathrm{d}z\,\mathrm{d}t\right)$$

with

$$A(\Psi) = \omega_\perp\left(\frac{3a_sN|\Psi(z,t)|^2}{\sqrt{1 + 2a_sN|\Psi(z,t)|^2}} - \frac{(1 + 3a_sN|\Psi(z,t)|^2)a_sN|\Psi(z,t)|^2}{(1 + 2a_sN|\Psi(z,t)|^2)^{\frac{3}{2}}} + \tag{3.17a}\right.$$

$$\left. + \frac{1 + 3a_sN|\Psi(z,t)|^2}{\sqrt{1 + 2a_sN|\Psi(z,t)|^2}} - 1\right)$$

$$B(\Psi) = \omega_\perp\left(\frac{3a_sN\Psi(z,t)^2}{\sqrt{1 + 2a_sN|\Psi(z,t)|^2}} - \frac{(1 + 3a_sN|\Psi(z,t)|^2)a_sN\Psi(z,t)^2}{(1 + 2a_sN|\Psi(z,t)|^2)^{\frac{3}{2}}}\right). \tag{3.17b}$$

The functional derivatives with respect to the control-parameter and to the adjoint parameter for the npSE are calculated analogously as for the GPE, i.e.

$$\delta_\lambda L((\lambda, \Psi, p); \xi_\lambda) = \gamma_{\text{reg}}\int_0^{T_t}\partial_t\lambda(t)\partial_t\xi_\lambda(t)\,\mathrm{d}t +$$

$$+ \text{Re}\left(\int_0^{T_t}\int p^*(z,t)i\frac{\partial}{\partial\lambda}V_\lambda(z,t)\Psi(z,t)\xi_\lambda(t)\,\mathrm{d}z\,\mathrm{d}t\right) \tag{3.18}$$

$$\delta_p L((\lambda, \Psi, p); \xi_p) = \text{Re}\left(\int_0^{T_t}\int \xi_p^*(z,t)\left(\partial_t\Psi(z,t) - f_{\text{npSE}}(\Psi(z,t), \lambda(t))\right)\,\mathrm{d}z\,\mathrm{d}t\right). \tag{3.19}$$

In contrast to $\delta_\Psi L((\lambda, \Psi, p); \xi_\Psi)$, these two functional derivatives do not change if the energy cost is used instead of the state cost. Furthermore, the derivative $\delta_\lambda L((\lambda, \Psi, p); \xi_\lambda)$ is the same in the GPE and the npSE and $\delta_p L((\lambda, \Psi, p); \xi_p)$ only differs in the system function f.

By setting all partial functional derivatives of $L(\lambda, \Psi, p)$ to zero for all admissible variations regarding the boundary conditions (3.2b) and (3.2c) and considering the fundamental lemma of the variational calculus, we get the optimality system for the state-trapping cost of the npSE

$$i\partial_t \hat{\Psi}(z,t) = -\frac{1}{2m}\Delta\hat{\Psi}(z,t) + V_{\hat{\lambda}}(z,t)\hat{\Psi}(z,t) +$$
$$+ \omega_\perp \left(\frac{1 + 3a_s N|\hat{\Psi}(z,t)|^2}{\sqrt{1 + 2a_s N|\hat{\Psi}(z,t)|^2}} + 1 \right)\hat{\Psi}(z,t) \tag{3.20a}$$

$$i\partial_t \hat{p}(z,t) = \left(-\frac{1}{2m}\Delta + V_{\hat{\lambda}}(z,t) + A(\hat{\Psi}) \right)\hat{p}(z,t) + B(\hat{\Psi})\hat{p}^*(z,t) \tag{3.20b}$$

$$\gamma_{\text{reg}}\partial_{tt}\hat{\lambda}(t) = -\operatorname{Re}\int \hat{\Psi}^*(z,t)\frac{\partial V_\lambda}{\partial \lambda}\Big|_{\lambda=\hat{\lambda}(t)}p(z,t)\,\mathrm{d}z \tag{3.20c}$$

$$\hat{\Psi}(z,0) = \Psi_0(z) \tag{3.20d}$$

$$\hat{p}(z,T_t) = i\int \Psi^*_{\text{des}}(z)\hat{\Psi}(z,T_t)\,\mathrm{d}z\,\Psi_{\text{des}}(z) \tag{3.20e}$$

$$\hat{\lambda}(0) = \lambda_0, \qquad \hat{\lambda}(T_t) = \lambda_T. \tag{3.20f}$$

If the energy cost for the npSE (3.9) is used, the final condition once again changes to

$$\hat{p}(z,T_t) = -2i\left(-\frac{1}{2m}\Delta + V_{\hat{\lambda}}(z,T_t) + \omega_\perp \left(\frac{1 + 3a_s N|\hat{\Psi}(z,T_t)|^2}{\sqrt{1 + 2a_s N|\hat{\Psi}(z,T_t)|^2}} + 1 \right) \right)\hat{\Psi}(z,T_t). \tag{3.21}$$

To solve the respective optimality system numerically, a gradient-based approach analogous to [31] was chosen. A gradient ∇J_λ is defined to meet

$$(\nabla J_\lambda, \xi_\lambda)_X = \delta J(\lambda; \xi_\lambda) \tag{3.22}$$

for all admissible directions $\xi_\lambda \in X$ and the inner product $(.,.)_X$ of the inner-product space X. As inner-product space, typical choices include the Sobolev H^1 or the Lebesque L^2 space, where $(a,b)_{L^2} = \int_0^{T_t} a(t)b(t)\,\mathrm{d}t$ and $(a,b)_{H^1} = \int_0^{T_t} \partial_t a(t)\partial_t b(t)\,\mathrm{d}t$. Note that the H^1 inner product lacks the term $\int_0^{T_t} a(t)b(t)\,\mathrm{d}t$ from the usual definition and the Dirichlet boundary conditions of $\lambda(t)$ will impose boundary conditions for ∇J_λ. In [31], optimal solutions computed in both functional spaces are compared. They find that the regularization parameter γ_{reg} influences the solution in the H^1 and the L^2 space differently and that in the H^1 space the optimal result tends to be less oscillating and more robust with respect to the choice of γ_{reg}. The H^1-based optimisation also obtains better cost-value results in less computation time. For this reason, H^1 was chosen as inner product space in this work.

To obtain the numerical solution of the optimality systems (3.11) or (3.20), the state equation (3.11a) or (3.20a) is propagated forward with some initial guess of the control

parameter $\lambda(t)$, which meets the boundary conditions (3.2c). At $t = T_t$, the final value of the adjoint variable can be computed using its terminal condition (3.12), (3.21), (3.11e) or (3.20e) depending on the chosen mathematical description and cost functional. The adjoint equation (3.11b) or (3.20b) is then solved backwards in time. Since (3.20b) is linear in p, no underlying iterations are needed to solve the implicit equation of the Crank-Nicolson scheme. As mentioned above, $\delta J(\lambda; \xi_\lambda)$ is equal to the partial functional derivative $\delta_\lambda L((\lambda, \Psi, p); \xi_\lambda)$ if Ψ and p are solved to meet their differential equations of the optimality system. Choosing the H^1 space and inserting the partial functional derivative from (3.18) into (3.22) results in a Poisson equation for $\nabla J_\lambda(t)$, i.e.

$$\frac{\mathrm{d}^2}{\mathrm{d}t^2} \nabla J_\lambda(t) = \gamma_{\text{reg}} \ddot{\lambda}(t) + \text{Re} \int \Psi^*(z,t) \frac{\partial V_\lambda}{\partial \lambda} p(z,t) \, \mathrm{d}z. \tag{3.23a}$$

$$\nabla J_\lambda(0) = 0, \qquad \nabla J_\lambda(T_t) = 0. \tag{3.23b}$$

With the values of Ψ and p from the forward and backward propagation this two-point boundary value problem can be solved by spatial discretization. Notice that ∇J_λ vanishes at time $t = 0$ and $t = T_t$ and thus is an admissible variation of the boundary conditions (3.2c). This is a feature of the H^1 space and would not be the case in the L^2 space setting, see [31]. With the obtained gradient, Quasi-Newton (BFGS) iterations are performed until $||\nabla J_\lambda||_X$ reaches a certain tolerance. The full algorithm for the IOA is summarized in Algorithm 1.

As for solving the GPE, the OCTBEC Matlab toolbox [25] is used to solve the optimality system (3.11) of the GPE. To solve the equations of the npSE (3.20), a Split-Step-solver and a Crank-Nicolson scheme was added to the toolbox in this work. Only the Crank-Nicolson scheme was used for all further simulations, as it was already detailed in the previous chapter.

Algorithm 1 Indirect optimisation approach (IOA)

Initialize: $j = 0, \lambda(t) = \lambda_{\text{init}}$ and BFGS algorithm initialisation

repeat

    $j \leftarrow j + 1$

    Propagate the GPE (2.5)/npSE (2.4) from its initial condition to get $\Psi(z,t)$.

    Calculate $p(z, T_t)$ depending on the chosen system equation and cost functional.

    Solve the respective adjoint equation (i.e. (3.11b) or (3.20b)) starting from $t = T_t$.

    Use the solutions of $\Psi(z,t)$ and $p(z,t)$ to solve the boundary value problem (3.23)
        and obtain the gradient ∇J_λ.

    Calculate the search direction $s_j(t)$ using the BFGS algorithm.

    Perform a line search to get the step size α_j .

        (requires multiple propagations of the GPE/npSE).

    Update the control variable $\lambda_j(t) = \lambda_{j-1}(t) + \alpha_j s_j(t)$.

until $||\nabla J_\lambda||_X < \epsilon$ or the maximum number of function evaluations is reached

---

3.3 Basis function approach (BFA)

In the basis function approach (BFA), the control parameter is composed of an initial guess $\lambda_{\text{init}}(t)$ and a set of basis functions $\lambda_i(t)$, $i = 1, \ldots, M$. The control parameter is thus given by

$$\bar{\lambda}(a_i, t) = \lambda_{\text{init}}(t) + \sum_{i=1}^{M} a_i \lambda_i(t), \tag{3.24}$$

with unknown coefficients $a_i \in \mathbb{R}$. The dynamic optimisation problem (3.2) is reduced to a finite-dimensional static optimisation problem

$$\min_{a_i} J(\bar{\lambda}(a_i, t)) \tag{3.25a}$$

$$\text{s.t. } \partial_t \Psi(z, t) = f(\Psi(z, t), \bar{\lambda}(t)), \qquad \Psi(z, 0) = \Psi_0(z) \tag{3.25b}$$

$$\bar{\lambda}(a_i, 0) = \lambda_0, \ \bar{\lambda}(a_i, T_t) = \lambda_T, \tag{3.25c}$$

where the evaluation of the cost function requires the solution of the state equations, which can be very complicated. If $\lambda_{\text{init}}(t)$ meets the boundary conditions (3.2c) and the basis functions are defined to meet $\lambda_i(0) = \lambda_i(T_t) = 0$, the boundary conditions of $\bar{\lambda}(a_i, t)$ are fulfilled automatically and the coefficients a_i are unconstrained. In this work, sine functions are chosen as basis functions and the initial guess λ_{init} is a linear ramp fulfilling the boundary conditions (3.2c)

$$\lambda(t) = \lambda_{\text{init}}(t) + \sum_{i=1}^{M} a_i \sin\left(it\frac{\pi}{T_t}\right). \tag{3.26}$$

With this choice, the resulting static optimisation problem is unconstrained apart from the system equation, which is solved during the function evaluation and does not constrain the parameters a_i. To find the optimal parameters a_i, one can use gradient-based or non-gradient-based optimisation algorithms. In this work, a Quasi-Newton algorithm is used without gradient information. The Quasi Newton algorithm could also be replaced by some other non-gradient-based methods. A popular global optimisation method is the so-called Bayesian or surrogate optimization, a method for computationally expensive cost functions where a virtual surrogate of the cost function is constructed iteratively [32]. Another common choice is the Nelder-Mead simplex optimisation. The latter method is a heuristic search method, which is often applied if gradients are not known or too expensive to calculate. Experience has shown that the BFA with a Quasi-Newton algorithm is a good choice for the investigated type of problems.

In the next section, the basis function approach (BFA) is compared to the solution of the full optimisation problem using the indirect optimisation approach (IOA).

3.4 Results for the optimal compression of a BEC

To compare the results obtained with the IOA to those obtained with a BFA, the compression of a BEC is used as exemplary problem. The external potential is shaped as a box whereby the walls are not assumed to be infinitely steep, but are composed of
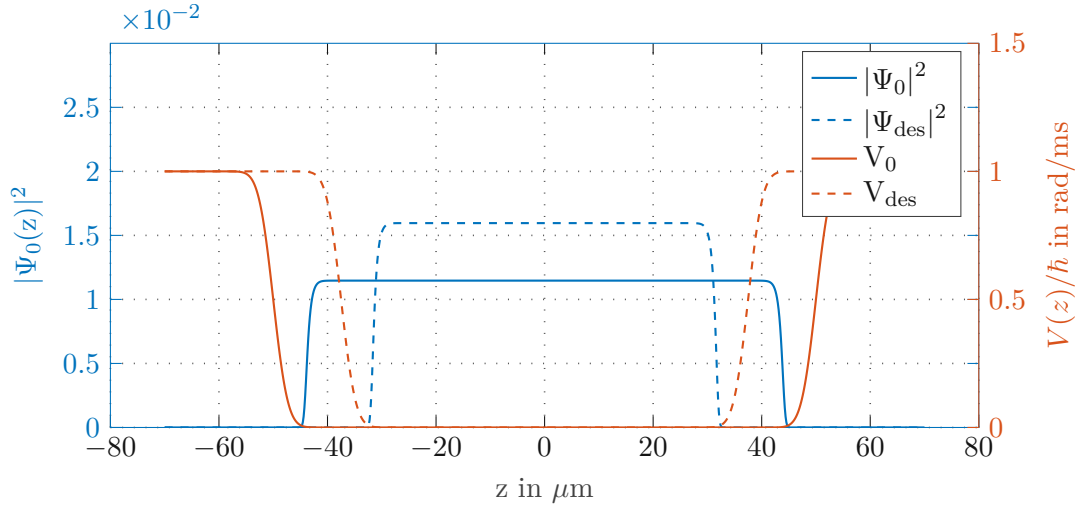
Figure 3.1: Initial and final potential landscape and density profile for the compression of a condensate from $100\,\mu\text{m}$ to $75\,\mu\text{m}$.

Gaussian error functions $\text{erf}(z)$. The box is then compressed from a width of $w_0 = 100\,\mu\text{m}$ to $w_T = 75\,\mu\text{m}$ symmetrically within $T_t = 50\,\text{ms}$, which yields a compression ratio $r_{\text{comp}} = \frac{w_0 - w_T}{w_0} = 0.25$ in this first scenario. The control parameter $\lambda(t)$ defines the displacement of the wall and goes from $\lambda_0 = 0$ to $\lambda_T = 12.5$ during compression. Thus, the external potential is written as

$$V(z,t) = V_{\max} - \frac{V_{\max}}{2}\,\text{erf}\left(\frac{z + (w_0/2 - \lambda(t))}{\sigma}\right) + \frac{V_{\max}}{2}\,\text{erf}\left(\frac{z - (w_0/2 - \lambda(t))}{\sigma}\right). \quad (3.27)$$

The parameter σ depends on the properties of the light from the optical system that shapes the external potential in the experiment and is assumed to be $3\,\mu\text{m}$ here. In Figure 3.1, the initial and desired 1D potential can be seen with the associated ground state density profiles. The initial state of the wave-function is the ground state of the initial configuration of the 1D potential. In all following GPE simulations, the effective coupling constant g_{eff} from (2.8) is used with the density ρ_0 of the initial ground state to adapt the speed of sound in the GPE to the npSE. Note that g_{eff} only adapts the GPE to the npSE for the initial state in linear order. In general, g_{eff} is a nonlinear equation of $|\Psi(z,t)|^2$ and by inserting ρ_0, the speed of sound can only be adapted if the compression ratio is not too high.

The evolution of the density profile over time, calculated in the npSE and the GPE, can be seen in Figure 3.2. The transition ends after $50\,\text{ms}$ and the external potential is held constant for another $50\,\text{ms}$. For these simulations, the condensate was compressed with a linear ramp as control parameter, i.e.

$$\lambda(t) = \begin{cases} \lambda_0 + \frac{t}{T_t}(\lambda_T - \lambda_0) & t \in [0, T_t] \\ \lambda_T & t \geq T_t, \end{cases} \quad (3.28)$$

with $T_t = 50\,\text{ms}$.
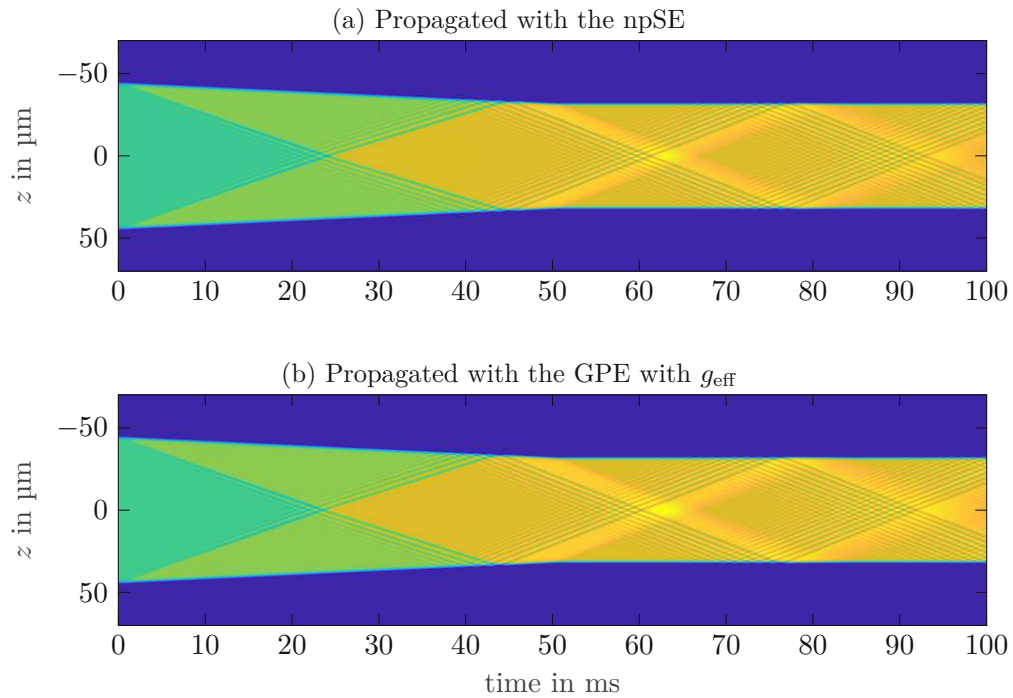
Figure 3.2: Comparison of the evolution of the density over time in the npSE and in the GPE with g_{eff}. The condensate is compressed from $w_0 = 100\,\mu\text{m}$ to $w_T = 75\,\mu\text{m}$ with the external potential of (3.27) using the linear ramp (3.28) as control parameter.

With increasing compression of the box, the density in the condensate rises and the speed of propagating waves in the GPE with g_{eff} deviates from the one in the npSE. When comparing the carpet-plots of the GPE and the npSE in Figure 3.2 visually, the result of the npSE and the GPE with g_{eff} look quite similar, but a more detailed analysis shows that the similarity decreases during the compression.

In the plots of Figure 3.2, it can be seen nicely that the speed of phononic excitations is limited by the speed of sound (2.7) and (2.6) in the condensate. When optimising the compression of a box-shaped BEC by only actuating the walls of the box, the time horizon cannot be shorter than the time the excited wave reaches the opposite wall. This time is referred to as 'minimum control time'. If the condensate would not be compressed, the travelling time of a wave from one wall to the other would be given by $\Delta T = w_0/c$. With compression, the density in the condensate increases and so does the speed of sound, which decreases the minimum control time. Furthermore, the movement of the opposite wall towards the travelling wave shortens the referred path, which further decreases the minimum control time. It follows that a more drastic compression in principle can be performed in shorter time for the given protocol, as long as the speed of the moving walls does not exceed the speed of sound in the condensate.

Note that the minimum control time arises from the limited actuation capabilities of only moving the walls of the box-shape potential. By allowing arbitrary potential shapes

in space and time, one could introduce momentum at any position, instead of just pushing the condensate from the sides. In this way, one would not rely on the condensate's internal dynamics to propagate the excited waves any more and the compression could be done faster than the minimum control time requires.

For the optimal control techniques proposed in this chapter, the transition time T_t is fixed and has to be chosen beforehand. The iterations needed to obtain an optimal trajectory highly depend on this choice of T_t. Indeed, the minimum control time marks a kind of sweet spot for T_t, whereby the resulting optimal trajectories have simple shapes if T_t is chosen a little bit higher than the minimum control time. When choosing T_t significantly higher, the optimal control problem becomes harder to solve. Interestingly, after about double the minimum control time, the reflected wave returns, which again alleviates the numerical issues of the optimal control problem. If the box was not compressed symmetrically from both sides, but only one wall was actuated, the optimal transition would take about double the time, because the moving wall would have to wait for the wave to be reflected back in order to cancel excitations. Therefore, we focus on studying symmetric compression and decompression in this work but all transitions could also be done by only actuating one wall.

To minimise excitations after the transition, we minimise either the state cost (3.6), in which the desired state is the ground state according to the final configuration, or the energy cost (3.7). In Figure 3.3, optimal trajectories resulting from the IOA, which solves the full optimal control problem (3.2), and the BFA (3.25) in the GPE are shown for the compression from $100\,\mu\text{m}$ to $75\,\mu\text{m}$. Optimal trajectories are given both for the energy cost (3.7) and the state cost (3.6), which results in four different optimal trajectories. For the BFA, the ansatz (3.26) is used with $M = 4$.

In Table 3.1 the resulting cost values of the IOA are compared to those obtained with the BFA. The optimisation with the energy cost (3.7) needs significantly less function evaluations to converge, both in the IOA and the BFA. The energy cost values of the two BFA results have a difference of two decades, although the state cost values are similarly small for both optimisation results (the one optimised with the state cost is even a bit smaller). This rises the question which of the two costs is more suited to evaluate the quality of transition. To investigate this problem, the evolution of the error to the desired ground state after the transition, with a fixed external potential, is analysed. This evolution for all of the four different optimal trajectories can be seen in Figure 3.4. Compared with Table 3.1, the optimal trajectories with low energy cost value at the end of the transition also have little oscillations after the transition. With the BFA in combination with the state cost, a state which resembles the ground state is reached, but it does not stay there as seen in the evolution of the error to the ground state. Furthermore, the energy cost generally has better convergence behaviour, a smaller number of function evaluations and is less sensitive to the choice of the time horizon T_t.

The basis functions and the components a_i in the ansatz (3.26) of the optimal result obtained with the BFA are shown in Figure 3.5. The trajectories optimised with the IOA in the infinite-dimensional search space are projected onto this reduced basis and their components are displayed for comparison. Interestingly, the solution of the BFA with the energy cost and the one of the BFA with the state cost exhibit similarly small state cost values (see Table 3.1) although their components differ quite a lot. Using the energy cost
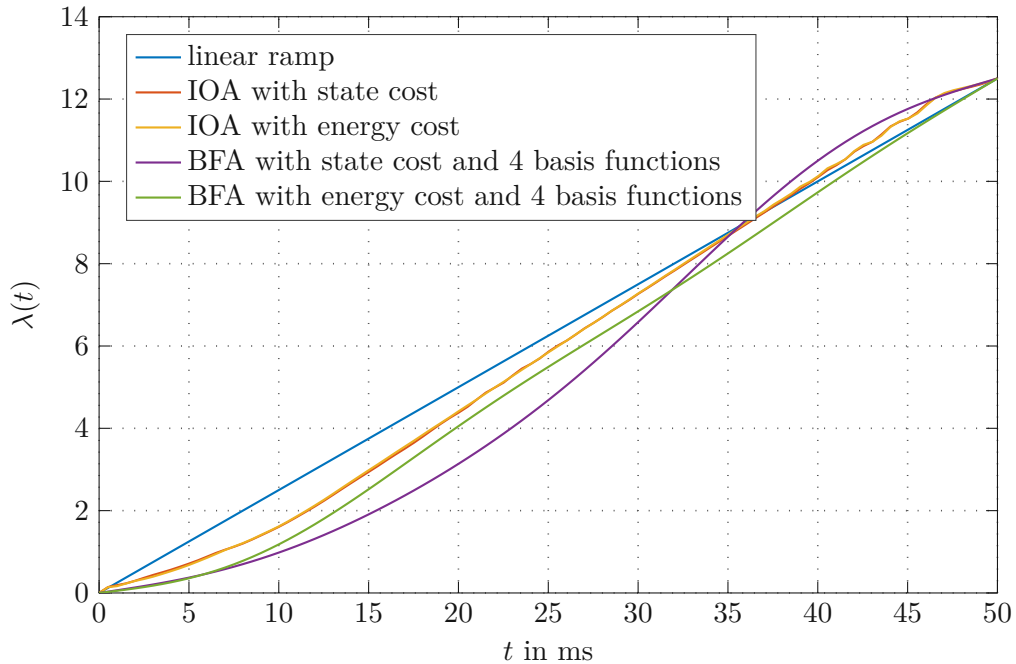
Figure 3.3: Optimal trajectories for the compression of a box-shape condensate from 100 to 75 µm in the GPE. The results found with IOA and BFA are compared whereby two different cost functionals (the state cost of (3.6) and the energy cost of (3.7)) are used.

	J_{energy}	J_{state}	number of cost function evaluations
linear ramp	$2.9441 \cdot 10^{-2}$	$1.9162 \cdot 10^{-1}$	1
IAO with state cost	$5.3696 \cdot 10^{-4}$	$3.7510 \cdot 10^{-5}$	535
IAO with energy cost	$1.5338 \cdot 10^{-5}$	$6.7511 \cdot 10^{-6}$	277
BFA with state cost	$2.7207 \cdot 10^{-2}$	$2.4546 \cdot 10^{-3}$	155
BFA with energy cost	$6.2236 \cdot 10^{-4}$	$8.9778 \cdot 10^{-3}$	65

Table 3.1: Comparison of state and energy cost values of optimal trajectories found by solving the full optimal control problem (3.2) using an indirect optimisation approach (referred to as IOA) and by solving the static optimisation problem in a basis function approach (BFA). As cost functionals the state cost (3.6) and the energy cost (3.7) are compared.
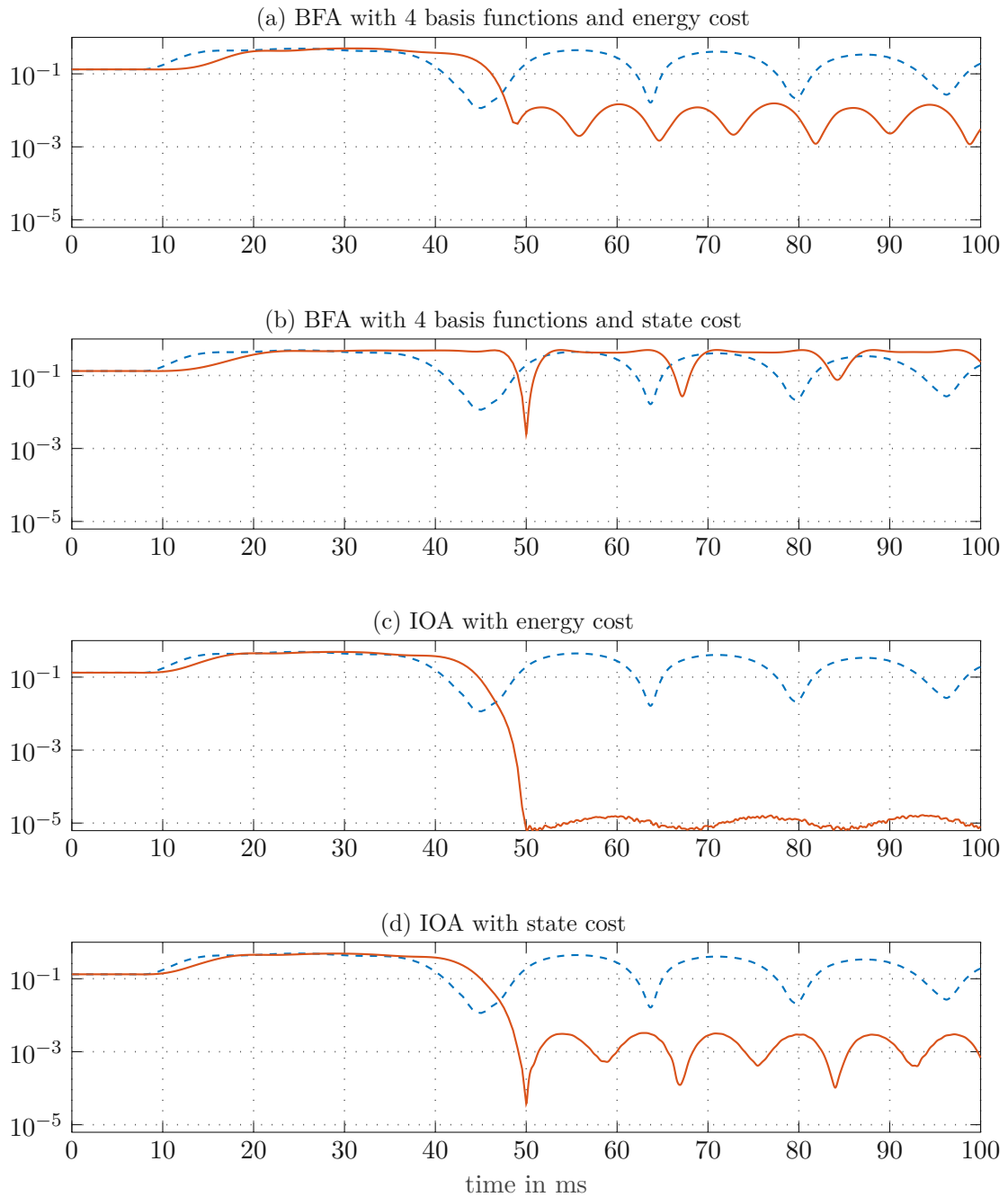
Figure 3.4: Evolution of the state cost $\left(\frac{1}{2}\left(1 - |\langle \Psi_{\text{des}}, \Psi(t)\rangle|^2\right)\right)$ during and after the compression with optimal control parameters, optimised with energy cost and state cost by solving the full optimal control problem (IAO) and using a basis function approach (BFA), respectively. The dashed line is the evolution of the state error if a linear ramp is used for compression.
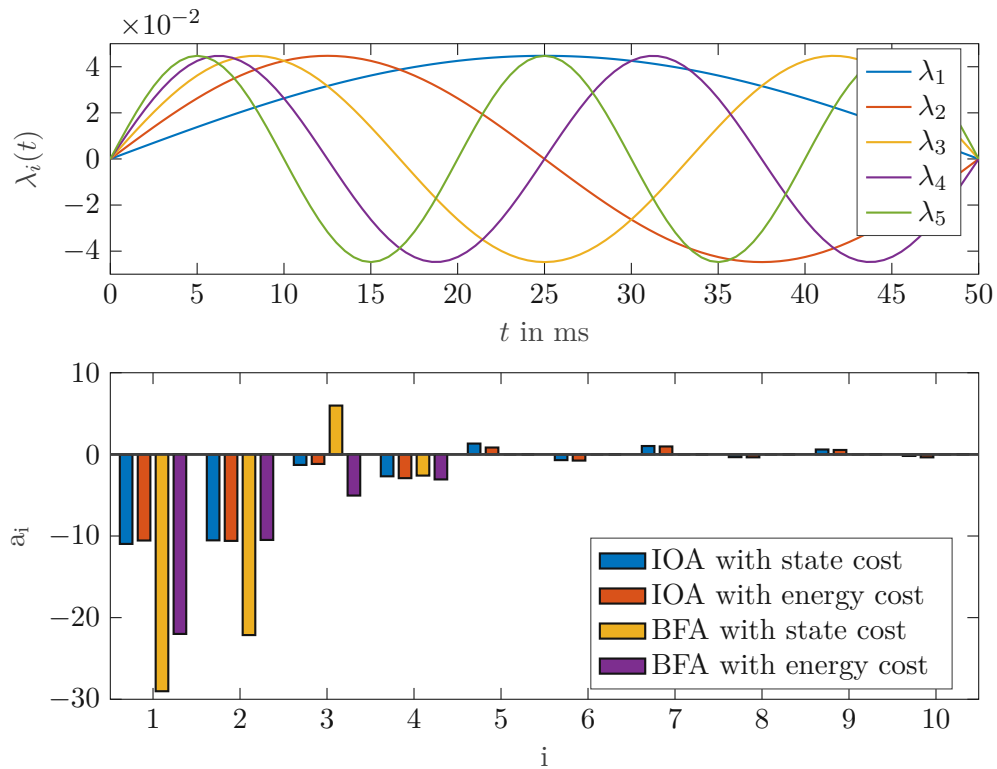
Figure 3.5: Above: First 5 basis functions λ_i of the ansatz (3.26). Below: Components a_i of the optimal result with the BFA ($M = 4$) and by solving the full optimisation problem with the IOA for the energy and state cost.

results in far less oscillations of the error to the desired ground state after the transition and thus, the choice of the right cost functional might be even more important in a BFA compared to the IAO where the search space is not restricted.

Figure 3.6 shows the obtained energy cost with the BFA as a function of the number of basis functions used in (3.26). It can be seen that a BFA with 8 harmonics can already reach costs in the same order as when the full OCT problem is solved. For the results that where discussed above the number of basis functions was chosen as $M = 4$ in order to avoid excessively high computation times.

In Figure 3.7, the trajectory that minimises the energy cost functional in the npSE (3.9) is shown alongside the optimal trajectory in the GPE, whereby the effective coupling constant g_{eff} was used for the GPE. The optimisation in the npSE reaches an energy cost value of $3.8623 \cdot 10^{-6}$ and a state cost value of $1.3075 \cdot 10^{-6}$ within 398 cost-function evaluation. For the discussed compression, which is not so strong, the speed of the travelling waves in the GPE is well adapted to the npSE by the effective coupling constant. The resulting optimal trajectories for $\lambda(t)$ are therefore very similar in both models. When applied to the respective other model, the trajectories obtain energy cost values in the order of 10^{-4}, which is still a good result. The evolution of the density, if the optimal trajectory of the GPE is applied to the npSE, can be seen in Figure 3.7. In this carpet
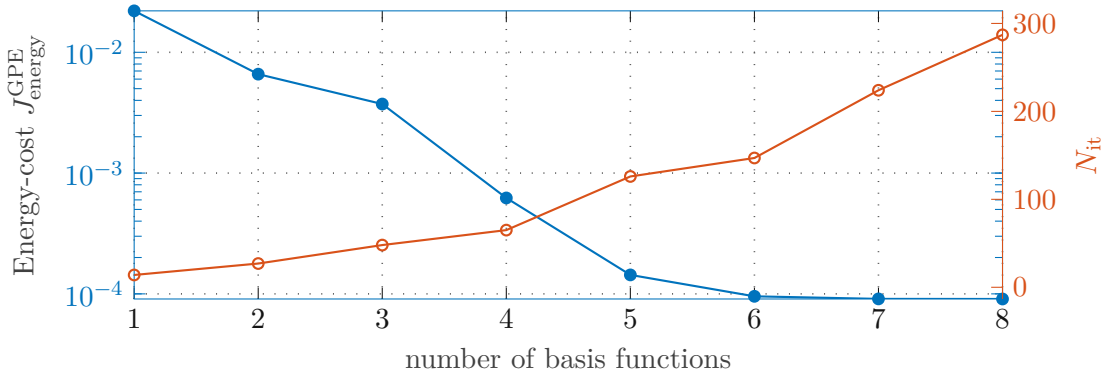
Figure 3.6: energy cost values $J_{\text{energy}}^{\text{GPE}}$ at $t = T_t$ and required number of cost-function evaluations N_{it} plotted over the number of basis functions M for the BFA (3.26).

	$J_{\text{energy}}^{\text{GPE}}$ propagated in GPE	$J_{\text{energy}}^{\text{npSE}}$ propagated in npSE
optimised in GPE	$1.5338 \cdot 10^{-5}$	$3.3597 \cdot 10^{-4}$
optimised in npSE	$2.9741 \cdot 10^{-4}$	$3.8623 \cdot 10^{-6}$

Table 3.2: energy cost values J_{energy} from (3.7) and (3.9) of the compression with control parameters optimised in the GPE and in the npSE model. The box-shaped condensate was compressed from 100 to 75 µm. Optimal trajectories are also applied to the respective other model.

plot it becomes obvious, that excitations after the transition are almost cancelled although the trajectory optimised in the GPE is applied to the npSE. The optimal cost values and the obtained cost values, if optimal trajectories are applied to the respective other model, are listed in Table 3.2.

For a more drastic transition, the box is compressed from a width of $w_0 = 100$ µm to $w_T = 50$ µm ($r_{\text{comp}} = 0.5$) and the optimal control problem is solved analogously to the compression discussed so far. Since the final box width is now smaller than previously, excited waves take less time to travel to the opposite walls and the minimum control time is smaller. The resulting optimal trajectories for the GPE and the npSE, which now go from $\lambda_0 = 0$ to $\lambda_T = 25$ within $T_t = 45$ ms, can be seen in Figure 3.9. Figure 3.8 shows the evolution of the density during and after the optimal compression in the GEP and the npSE. For comparison, the carpet plot of the linear compression is plotted above the optimal result. No visually observable excitations are remaining after the transition when the optimal trajectory is used. In Table 3.3, the achieved energy cost values are displayed. Comparing these results to those of the less drastic compression from above (Figure 3.7 and Table 3.2), it can be seen that the optimal control parameters in the GPE and the npSE now differ a lot and result in worse cost values applied to the respective other model. The effective coupling constant g_{eff} can no longer appropriately adapt the speed of sound to the npSE for more drastic compressions. This relation can also be seen in the carpet
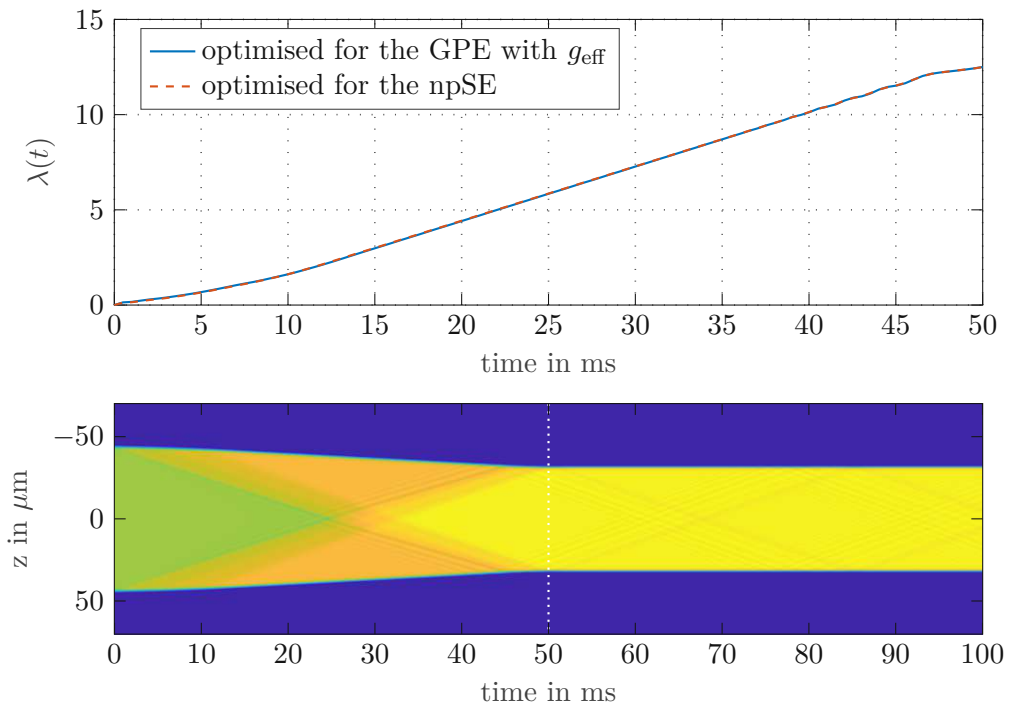
Figure 3.7: Above: optimal trajectories calculated for the GPE with g_{eff} and for the npSE. Below: Carpet plot of the density, whereby the trajectory optimised in the GPE with g_{eff} was used, but the propagation was calculated in the npSE. The resulting energy-cost value is $J_{\mathrm{energy}}^{\mathrm{npSE}} = 3.3597e - 4$.
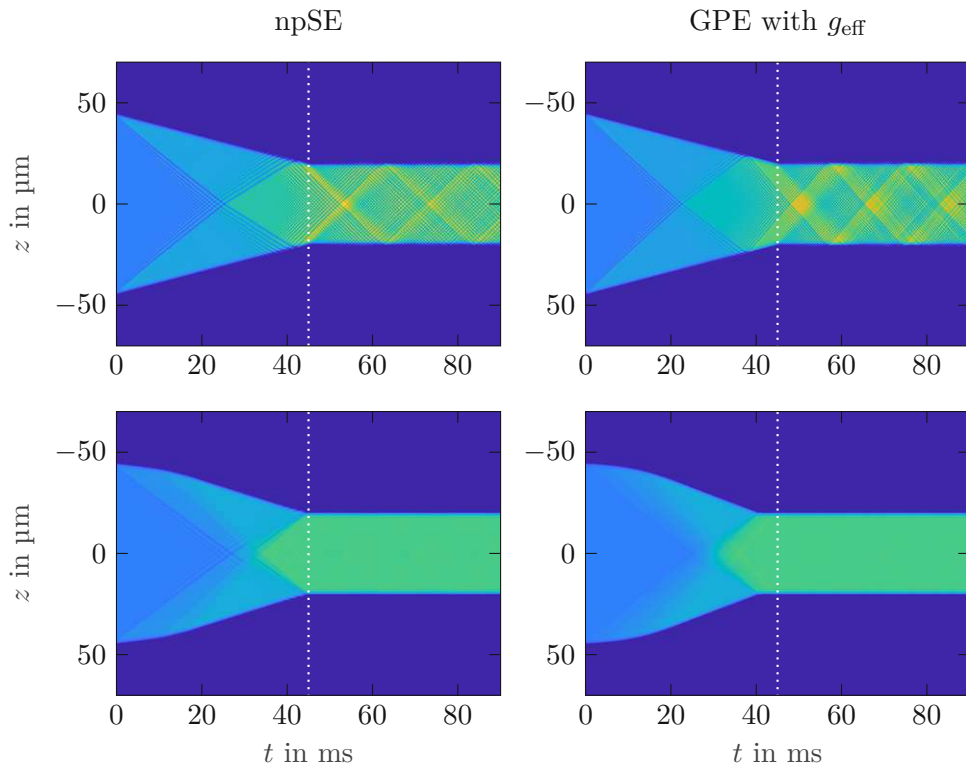
Figure 3.8: Evolution of the density in the npSE and in the GPE during and after compression of a box-shaped condensate from $w_0 = 100\,\mu\mathrm{m}$ to $w_1 = 50\,\mu\mathrm{m}$ within $45\,\mathrm{ms}$. Corresponding cost values are listed in Table 3.3.

plot of Figure 3.9, where the trajectory that is optimal in the GPE with g_{eff} was applied to the npSE. In contrast to the less drastic compression, which was discussed before, a lot of excitations are remaining in this scenario.
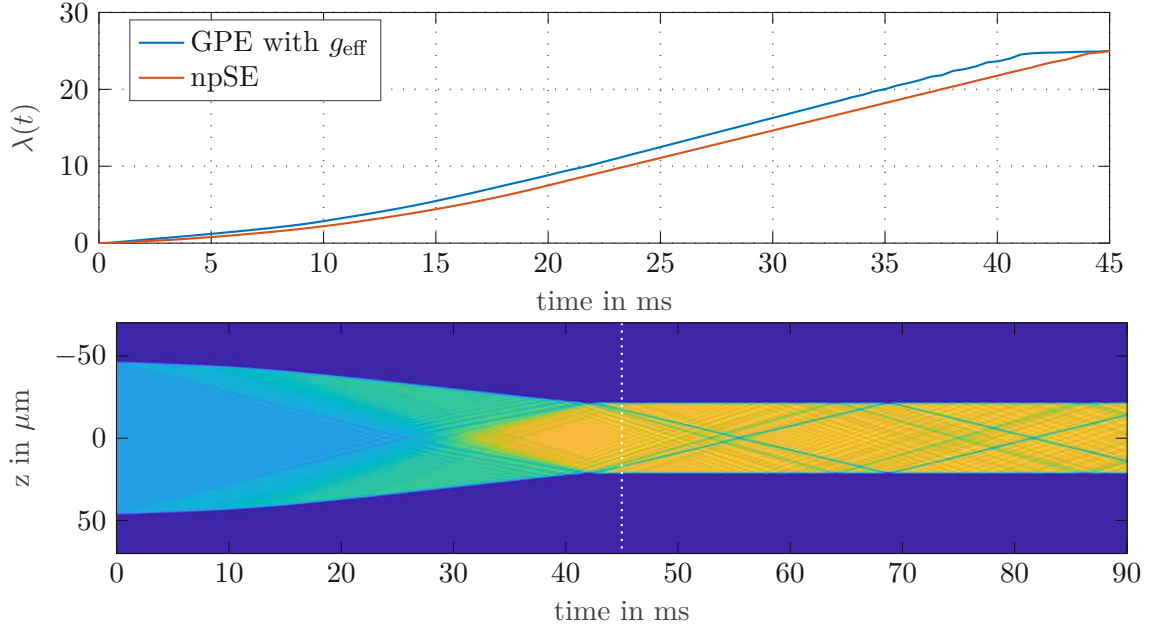
Figure 3.9: Above: Optimal trajectories for the optimisation of the energy cost functional
for the GPE with g_{eff} and the npSE. Below: Evolution of the density when the
optimal trajectory from GPE with g_{eff} is applied to the npSE. This transition
results in an energy cost value of $J_{\text{energy}}^{\text{npSE}} = 5.217 \cdot 10^{-2}$.

	$J_{\text{energy}}^{\text{GPE}}$ if the wave-function is propagated with the GPE with g_{eff}	$J_{\text{energy}}^{\text{npSE}}$ if the wave-function is propagated with the npSE
optimised in GPE with g_{eff}	$1.3416 \cdot 10^{-4}$	$5.217 \cdot 10^{-2}$
optimised in npSE	$5.68 \cdot 10^{-2}$	$4.6694 \cdot 10^{-5}$

Table 3.3: energy cost values J_{energy} from (3.7) and (3.9) of the compression with control
parameters optimised in the GPE and in the npSE model. The box-shaped
condensate was compressed from 100 to 50 µm. Optimal trajectories are also
applied to the respective other model.

3.5 Adaption of the model to experimental results

In the considered experiment, the box-shaped potential is realised with a digital micro mirror device (DMD) [15]. This DMD has pixels to turn on or off and to compress the condensate in the experiment. For this, the box-walls are actuated by turning on whole columns of pixels. A new configuration is sent to the DMD every 0.25 ms, which is why a time and value discretization has to be applied to implement the optimal trajectories on the experiment.

For the more drastic compression from $w_0 = 100\,\mu\text{m}$ to $w_1 = 50\,\mu\text{m}$, 60 pixels are available for the full compression range both on the left and the right of the condensate, which results in discrete steps of $\lambda(t)$ with the size of $\frac{25}{60}$. The optimal trajectory for the compression, which was obtained in the GPE, is implemented on the experiment. The resulting experimental density data is shown in Figure 3.11(a). For plotting the evolution of the density over 90 ms with a resolution of one millisecond, 90 new experiments where prepared and terminated at different times during the compression. Moreover, multiple experiments have to be done for one time-slice to obtain an estimate of the mean density by averaging.

When comparing the experimental data in Figure 3.11(a) to the optimal transition in Figure 3.8, it can be seen that the excited waves hit the opposite wall a little bit too late and the excitations are not cancelled in the experiment. When only the walls can be activated and no global control of the potential V is possible, the quality of the transition is very sensitive to the value of the speed of sound. The speed of sound in the GPE (2.7) is proportional to the square root of the coupling constant as described in Chapter 2. By measuring the slope of the wave propagation in the carpet plot of the experimental data, the speed of sound can be calculated and the coupling constant $g_{1\text{D}}$ can be adapted manually to fit the experiment.

Furthermore, the initial density profile of the experiment (depicted in Figure 3.10) is not a perfectly smooth box as it was assumed in the previous calculations. The potential profile in the experiment can be estimated from the experimental initial density by using the Thomas-Fermi approximation (2.10). The resulting non-smooth box potential is also displayed in Figure 3.10. The wall heights where modified so that the density in the wall stays zero during the compression. This adapted potential is included in the simulations, but the compression is still done only by pushing symmetrically from both sides. Note that only the initial potential shape is known relatively well from the initial ground state density profile, while the evolution of the potential can only be roughly estimated. The precise movement of the potential walls in the experiment is not known, since the optical path is not perfectly identified and determining which influence switching on entire rows of the DMD has on the condensate is not a straightforward task. Thus, the evolution of the potential $V(z,t)$ is only a rough estimate of the experimental potential. For the following simulations, walls that are composed of Gaussian error functions with $\sigma = 2\,\mu\text{m}$ where added to the Thomas-Fermi approximation of experimental initial configuration seen in Figure 3.10. These walls where compressed symmetrically according to the control parameter to adapt the potential $V(z,t)$ to the experiment.

The adaption of the coupling constant was done manually in this chapter by measuring the slope of the excited waves in the experimental carpet plot. The speed of sound in

the GPE is proportional to the square root of g_{1D}, which allows simple adaption to the experiment. This manual method might not be the most efficient and precise way of estimating the experimental coupling constant. Therefore, a recursive minimum variance estimator is presented in Chapter 4 to adapt the parameter in an optimal way. The carpet plot of the GPE with adapted coupling constant $g_{adapted} = 230$ and adapted potential shape is also shown in Figure 3.11(c). In this evolution of the density, the diamond shaped patterns agree nicely to the experimental data.

In Figure 3.11(b), the carpet plot resulting from the npSE with adapted number of particles and adapted potential is shown. Since the atom number fluctuates in the experiment, the mean number of atoms of all experimental measurements is used. The resulting density pattern of the npSE visually agrees well with the experimental data. Thus, an optimal trajectory calculated in the npSE with the correct atom number from measurements and adapted potential also could improve the result on the experiment.

Using the GPE with adapted coupling constant and adapted potential shape, a new optimal trajectory is calculated. This new optimal trajectory is show in Figure 3.12 alongside the density evolution of the linear and the optimal compression. Visually, very view excitations are remaining after the transition. Further insight into the remaining excitations gives the evolution of the state error, which is shown in Figure 3.13. For the non-smooth box, not all excitations can be cancelled. The optimised energy cost value is $7.5217 \cdot 10^{-2}$ and in the evolution of the state-error it can be seen that the obtained trajectory still performs better than a linear ramp and the original optimal trajectory for a smooth box. Since the adapted non-smooth box is also not symmetric, the use of two control parameters to move the walls independently of each other instead of symmetrically compressing the box could further improve the result.
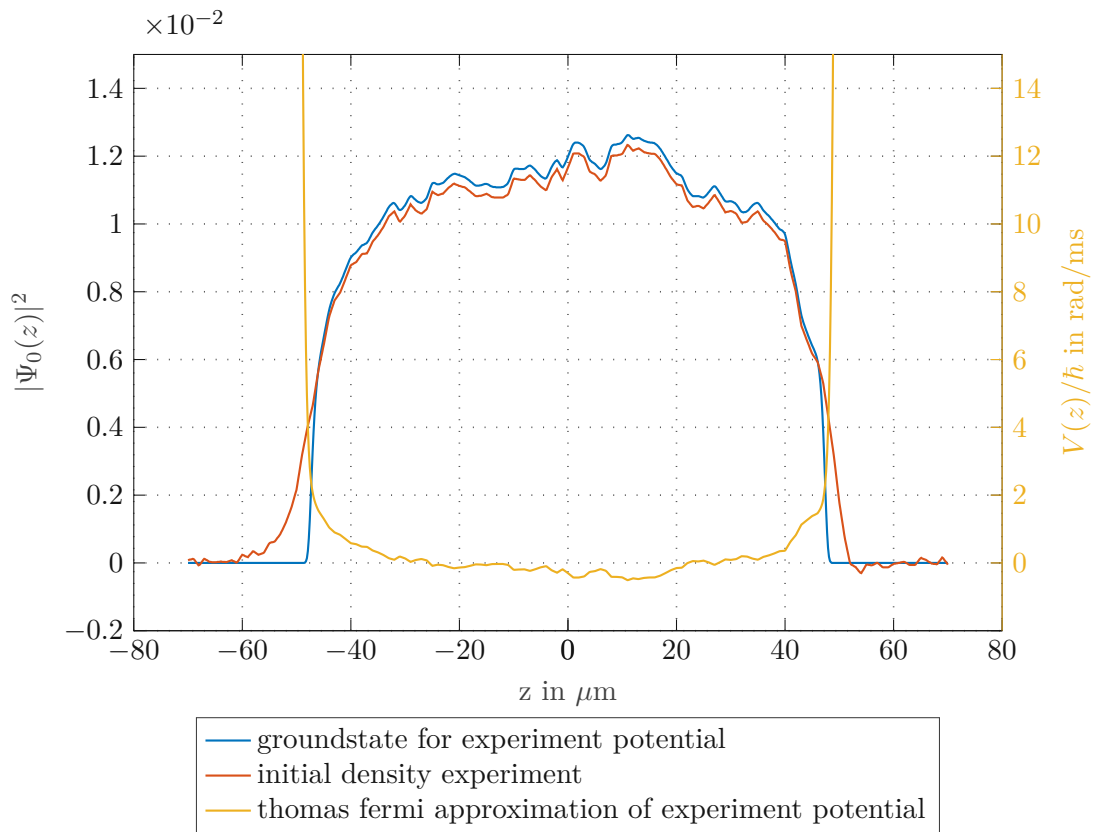
Figure 3.10: Initial density data from the experiment, adapted external potential to fit the initial state of the simulation to the experiment.

(a) Density data from the experiment

(b) Evolution of $|\Psi(z,t)|^2$ in the npSE, with adapted potential V and the atom number from the experimental data

(c) Evolution of $|\Psi(z,t)|^2$ in the 1D-GPE, with manually adapted coupling constant so that the speed of sound matches experimental data ($g_{\text{adapted}} = 230$)
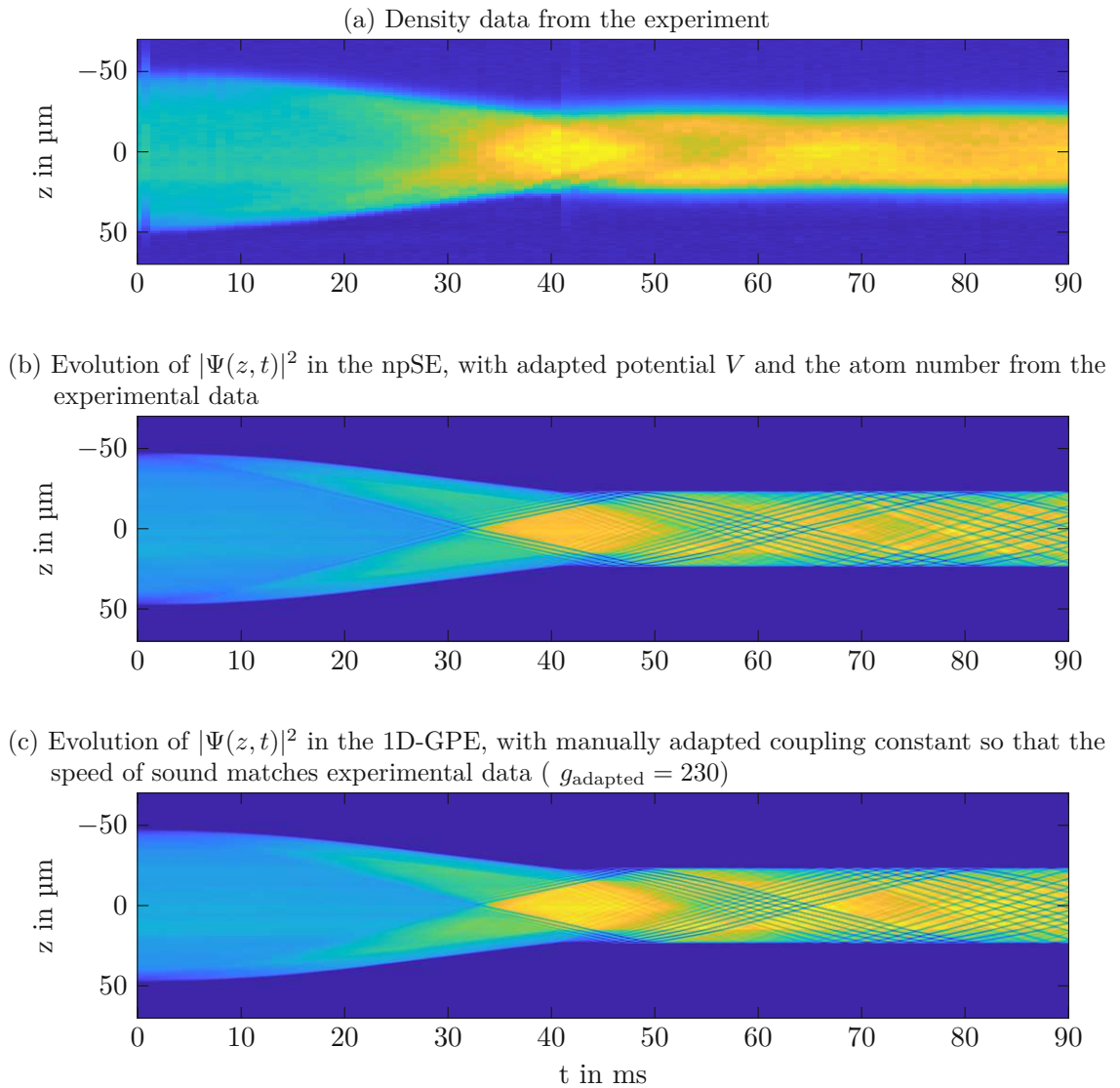
Figure 3.11: Comparison of experimental density data to the simulation results using the npSE and the GPE. The potential landscape of both simulations is adapted to the experiment by using the Thomas-Fermi approximation.
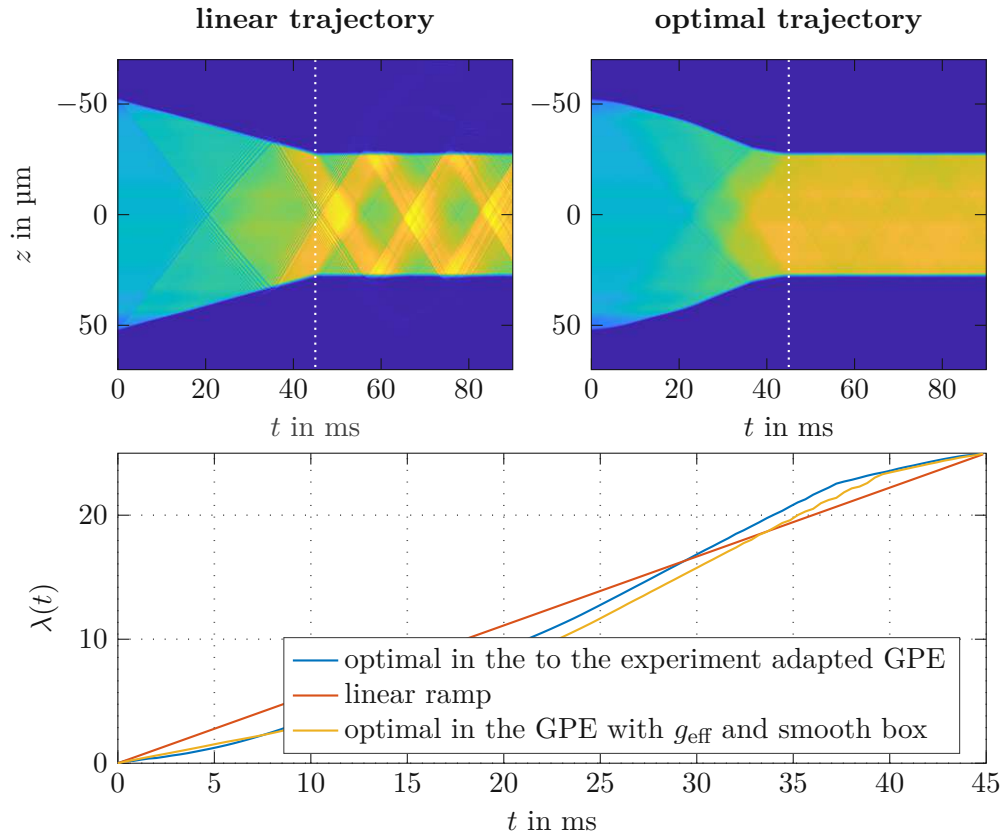
Figure 3.12: Carpet plots for the linear and optimal trajectory in the GPE, whereby the coupling constant and the potential where adapted to the experiment. The resulting optimal trajectory is compared to the trajectory that is optimal for the GPE with the theoretical effective coupling constant in a smooth box potential.
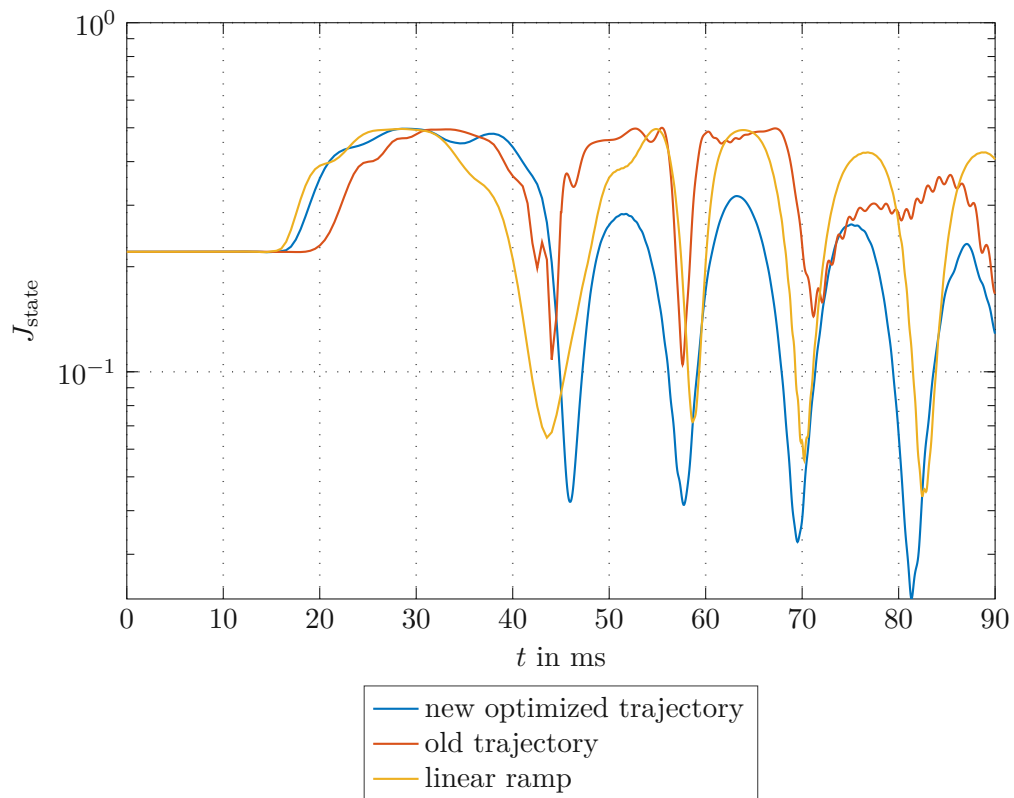
Figure 3.13: Evolution of the state cost, whereby the coupling constant of the GPE and the potential $V(z)$ was adapted to fit the experimental data. The result of the transition with the original optimal control parameter, which was optimised without adaption of the GPE or the potential shape, is compared to the result with a new optimal trajectory, which was optimised in the adapted GPE with non-smooth potential $V(z)$. The result of a transition with a linear ramp is included for comparison purpose.

3.6 Optimal trajectories for the whole QFTM sequence

Up to now, only optimal compression sequences where considered since they can be formulated for a single compartment. To treat the whole cooling cycle (see Chapter 1), the potential $V(z, t)$ is composed of error functions analogous to (3.27) to form three compartments (the system (S), the piston (P) and the bath (B)). Since all compartments are decoupled in the initial configuration, the ground state for each compartment is calculated separately whereby the atom number is set to 5000 for each of the three compartments. The resulting 1D potentials and the associated ground state density of the mean-field wave-functions for every configuration is depicted in Figure 3.14. The quantum thermal primitives are the transitions from one configuration to the next and can be described by the evolution of several control parameters. The compression of a condensate, which is captured by symmetric displacement of the walls, was investigated in great detail in the previous sections. For the decompression of a subsystem, the same parametrisation (3.27) as for the compression is used, only the initial and final value of the control parameter are exchanged.

In the presented cycle, coupling is realised by bringing two subsystems close together and decreasing the wall width between them. By decompressing B, P and B are brought close together automatically, which means that coupling is not a step on its own, but is integrated in the decompression of B. The decompression of B not only enables coupling but also enhances energy flow from P to B since B is cooled down. Furthermore, this way of coupling allows very easy tuning of the coupling strength. By defining the initial position of B, the target wall width is set which has direct influence on the coupling strength. The same relations apply to the coupling of S and P. By decompressing P, it is brought close to S and the final wall width can be tuned by the initial position of S. Another parameter that could be introduced to set the coupling strength is the wall height during coupling. This method of coupling would require an additional subsequence for coupling two subsystems, which would be controlled by additional control parameters. In this work, it is assumed that the decrease of the wall width allows sufficient coupling, and no control parameter for the wall height is introduced. In Figure 3.14, there is still a variation in the wall height visible for small wall widths, because the potential $V(z, t)$ is composed of error functions with a finite slope. With this choice of realising a full cooling cycle, four trajectories are needed, namely those two for the parameter λ_{piston}, which controls the compression and decompression of the piston (P), and another two for the parameter λ_{bath}, which controls the compression and decompression of the bath (B).

As already noted, optimal coupling in the GPE should do nothing. Thus, it does not make sense to investigate coupling parameters as the target wall width, the time of coupling or the wall height in the GPE. Those coupling parameters have to be studied and optimised in advanced models. The chosen method of coupling makes further investigations beyond mean-field theories and possible optimisation steps easy because one can change the final wall width by simply setting the initial position of B instead of calculating new optimal trajectories that minimise mean-field excitations, when adapting coupling parameters. For the presented results in the mean-field GPE, the coupling wall width for both coupling processes is chosen to $5\,\mu\text{m}$. The time of coupling is chosen to $5\,\text{ms}$ for the presented mean-field simulations. In further investigations of the QFTM sequence

that go beyond mean-field theory it might turn out that the chosen parameters do not achieve sufficient coupling and there could be the need of adding an additional sequence for lowering the walls while coupling.

Furthermore, adjusting the relative potentials of two compartments before coupling them is not investigated at this point, which could help to avoid undesired particle flow. Since overall control of the experimental potential is not yet possible, this adjustment might not be easy to implement on the experiment at the current status of the project.

The resulting evolution of the density is shown in Figure 3.15a, whereby linear ramps are used for all transitions. The mean-field is excited with every subsequence, and a lot of excitations remain after one cycle. The optimal trajectories for all QTPs are presented in Figure 3.16 and the evolution of the density for a mean-field optimal cooling cycle can be seen in Figure 3.15b. It is clearly visibly that most of the excitations are cancelled by the optimal trajectories. A drawback could be that excitations that possibly were not cancelled in one QTP get carried along for the next sequence and will sum up over several cycles. This is a consequence of treating each QTP individually. One could approach this problem by defining the initial state of the optimisation for the next cycle as the final state of the previous cycle if needed. Figure 3.17 shows the intermediate density profiles for the non-optimal and optimal cooling cycle. Both in the non-optimal and in the optimal cooling cycle the remaining excitations are bigger in B than in P, since the compression ratio of B is higher than the one of P. A more accurate analysis of the difference between the linear and the optimal cooling sequence is possible by comparing the evolution of energy

$$J_{\text{energy}}(t) = \int \Psi^*(z,t)\left(-\frac{1}{2m}\partial_{zz} + V_\lambda(z,t) + \frac{g_{1\text{D}}}{2}|\Psi(z,t)|^2\right)\Psi(z,t)dz, \qquad (3.29)$$

which is the Hamiltonian of the GPE. The resulting evolution of $J_{\text{energy}}(t)$ is shown in Figure 3.18. An ideal cooling sequence should introduce no mean-field excitations and the energy after all transitions should be the energy of the desired ground state, which is identical to the initial state. It can clearly be seen in the evolution of energy that the optimal sequence introduces far less energy than the linear one. More precisely, the distance to the energy of the desired final state is only $0.003\,199\,\text{kHz}$ for the optimal sequence and $0.157\,27\,\text{kHz}$ for the linear transitions.

The optimised trajectories and results for the full cycle where calculated using the 1D-GPE (2.5). All calculations can also be done in the npSE (2.4), which is a more accurate description of the actual quasi 1D condensate in the considered experiment. The only drawback of using the npSE is the increase of computational costs, since solving the npSE involves more complex equations. Optimal trajectories for the QFTM sequence in the npSE are depicted in Figure 3.16 in addition to the results for the GPE.

The presented protocol surely is not the only possible solution of realising the QFTM sequence. As argued for the example of compressing a box-shaped condensate, displacing the walls symmetrically from both sides results in about half the minimum control time compared to the one-sided compression. Therefore, the presented protocol brings advantages regarding the duration of one cycle, especially because decompression and compression of P and B could be done quasi simultaneously. An alternative protocol could avoid actuation of B to prevent additional heating. In this scenario, P would have to be
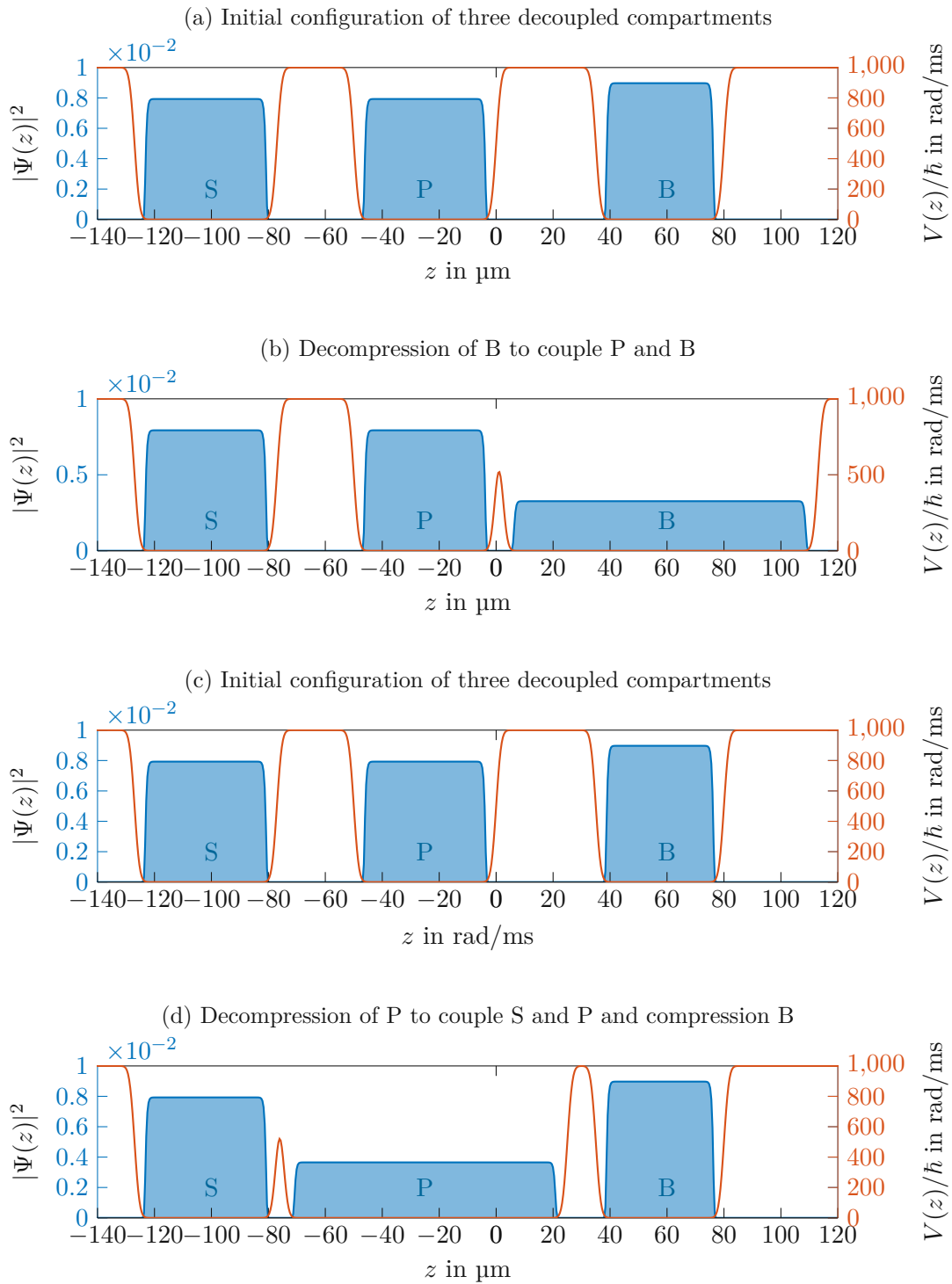
Figure 3.14: Ground states of all intermediate configurations of the potential $V(z, t)$ for the cooling cycle. Transitions from one configuration to another are controlled with the parameters $\lambda_{\text{piston}}(t)$ and $\lambda_{\text{bath}}(t)$.

(a) Cooling cycle with linear trajectories

(b) Optimal cooling cycle
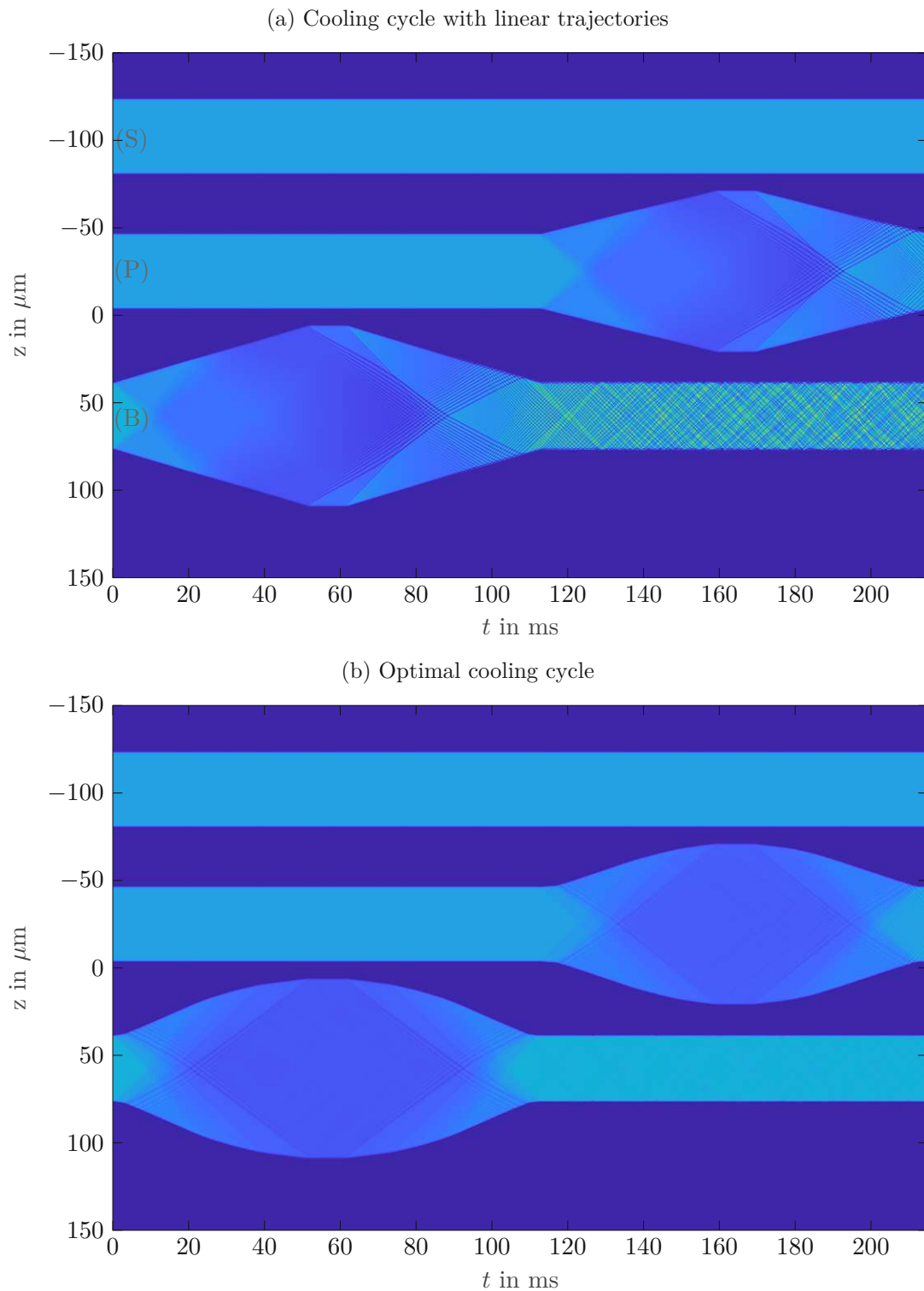
Figure 3.15: Evolution of the density $\rho(z,t)$ during one cooling cycle with linear (a) and optimal (b) trajectories. Optimal trajectories can be seen in Figure 3.16.
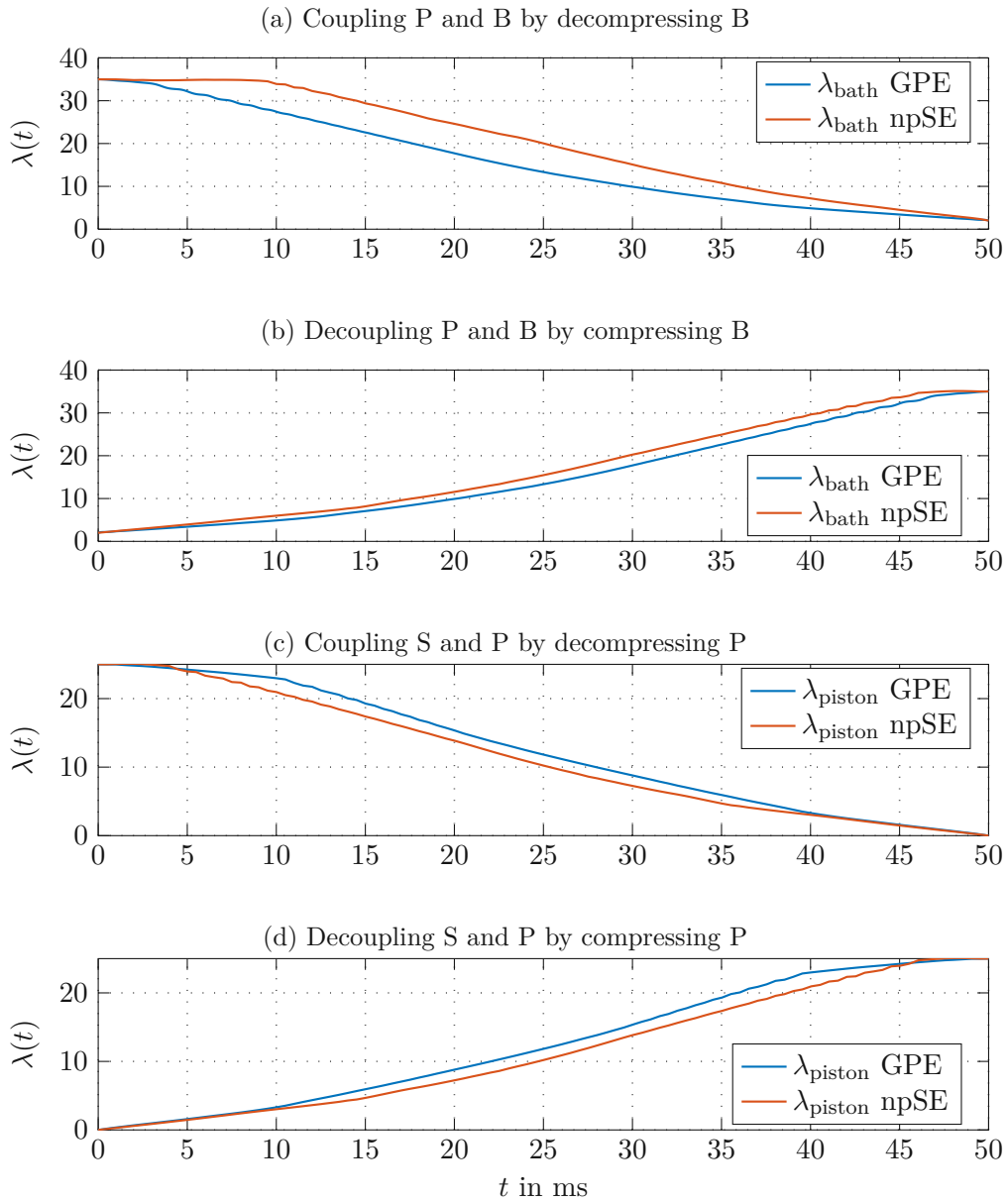
Figure 3.16: Optimal trajectories for the whole QFTM sequence to perform one cycle with minimal mean-field excitations.
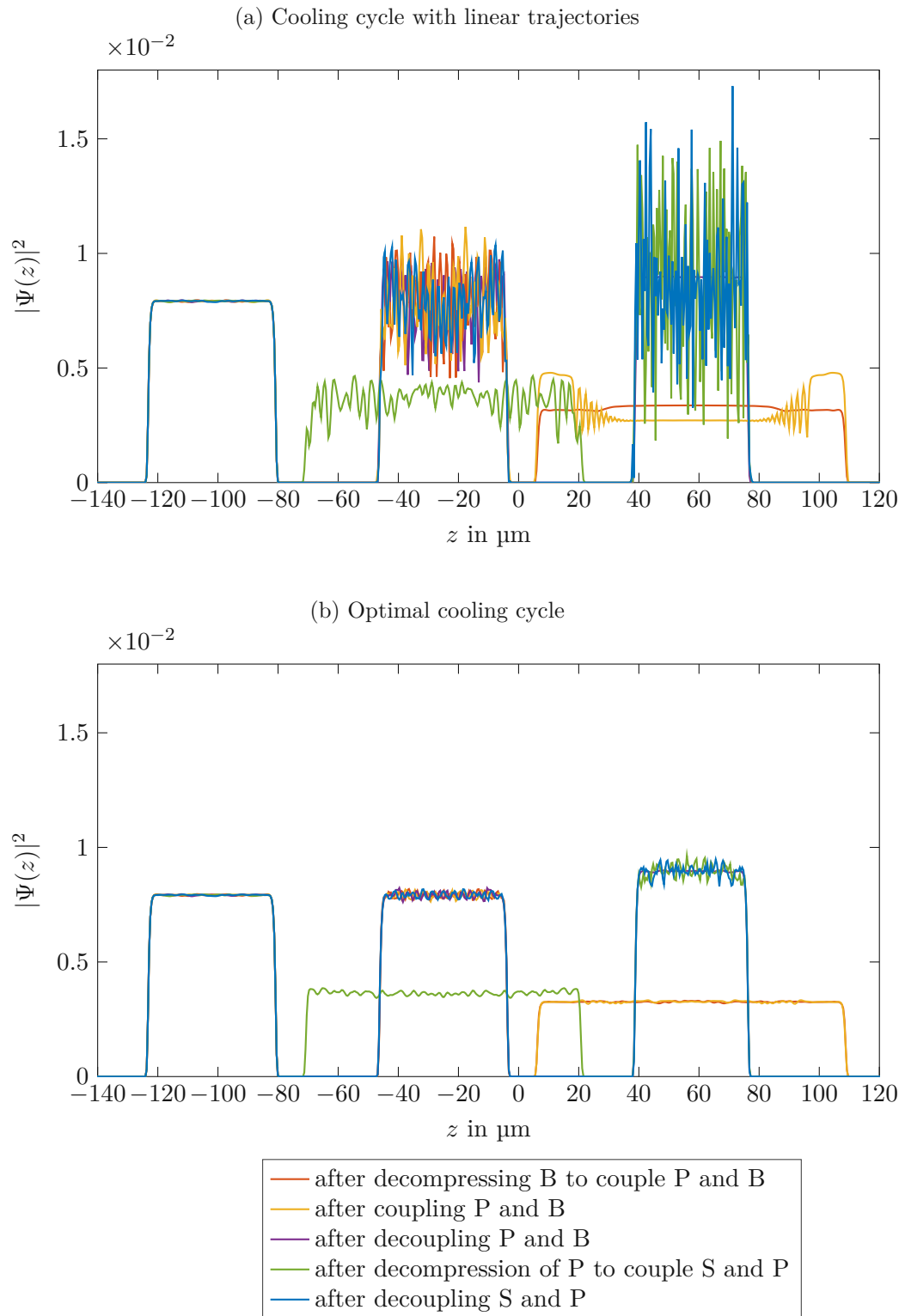
Figure 3.17: Intermediate density profiles during one cooling cycle with linear ramps (a) and with optimal trajectories (b) for the GPE. Optimal trajectories can be seen in Figure 3.16.
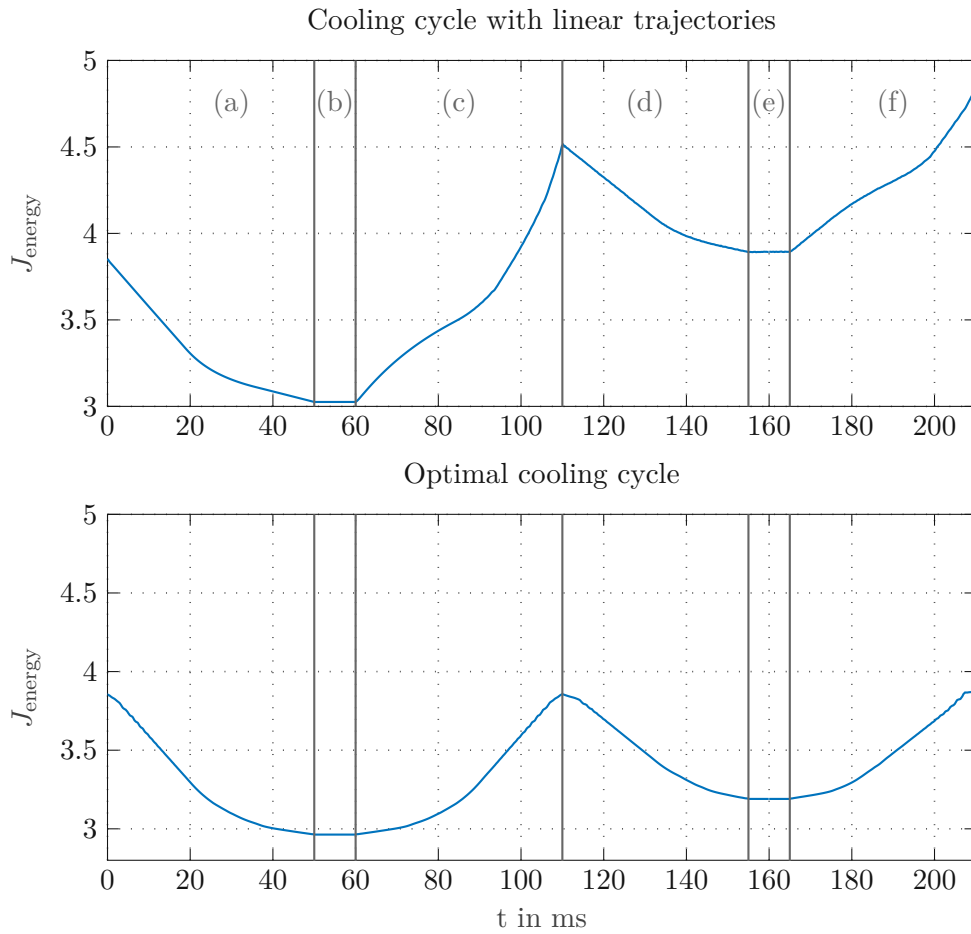
Figure 3.18: Evolution of the mean-field energy (3.29) during the cooling cycle. The result of linear trajectories is compared to the one with optimal control parameters for the GPE. (a) Decompression of B (b) Coupling P and B (c) Compression of B (d) Decompression of P (e) Coupling S and P (f) Compression of P

actuated only by moving its left wall in order to keep the wall width between P and B small. Coupling could then be obtained by additional lowering of the wall.

Using moving compartment walls is a simple and efficient method to manipulate BECs without arbitrary shaped potentials. Optimal trajectories however rely on cancellation of propagating waves in this case. When choosing such an approach in a pure feed forward manner, the mathematical model used during offline optimisation has to fit the experiment extremely well to obtain good results. To overcome this problem, a parameter estimator is designed in Chapter 4 to automatise the adaption of the mathematical model to the experiment. Another approach would be to further improve the trajectories directly on the experiment. The cost functional of such an online optimisation has to assess measurable quantities. In the cost functionals presented above, the wave-function was used to calculate the distance to the ground state or the energy, which are both clearly not measurable. Moreover, the restricted number of online iterations limits the available optimisation schemes to low-level approaches such as the BFA described in Section 3.3. The next section briefly discusses a BFA with a cost functional that assesses the mean-field density of the condensate after transition.

3.7 A basis function approach with measurable quantities

With regard to implementing an optimisation loop directly on the experiment, it is necessary to choose a suitable quantity to be assessed in a cost functional. This quantity not only has to be measurable, but the optimisation should also aim at minimising mean-field excitations after the transition.

A simple measurement that can be taken after each experiment is the atom distribution, which corresponds to the density $\rho(z,t) = |\Psi(z,t)|^2$ in the GPE. Based on the Bhattacharyya-distance one can define a density cost functional

$$J_{\text{density}} = \frac{1}{2}\left(1 - \left|\int \sqrt{|\Psi_{\text{des}}(z)|^2}\sqrt{|\Psi(z,T_t)|^2}\,\mathrm{d}z\right|^2\right), \tag{3.30}$$

that compares the final density profile to the density profile of the desired state. In Figure 3.19, the evolution of this density error and the state error is shown with a trajectory that minimises (3.30). The state error compares the mean-field wave-function to its desired ground state. Directly at $t = T_t$ the density cost indeed reaches a small value, but the condensate is not in its ground state, as seen in the remaining excitations of the state error. Due to missing phase information the density cost (3.30) cannot determine if the condensate is in its ground state. This exemplary problem shows that it is not a straightforward task to choose the right quantity to be assessed in a cost functional if mean-field excitations should be minimised after the transition.

One could use measurement data of multiple points in time or the combination of measurable quantities other than the density. Additionally, this issue could be alleviated by incorporating model information. Such a procedure would be conceptually related to the parameter-estimation approach investigated in the following chapter of this thesis.

$$\frac{1}{2}\left(1 - \left|\int \sqrt{|\Psi_{\text{des}}(z)|^2}\sqrt{|\Psi(z,t)|^2}\,\mathrm{d}z\right|^2\right) \qquad \frac{1}{2}\left(1 - \left|\int \Psi_{\text{des}}^*(z)\Psi(z,t)\,\mathrm{d}z\right|^2\right)$$

- - - linear ramp ——— trajectory that minimises the density-cost (3.27)
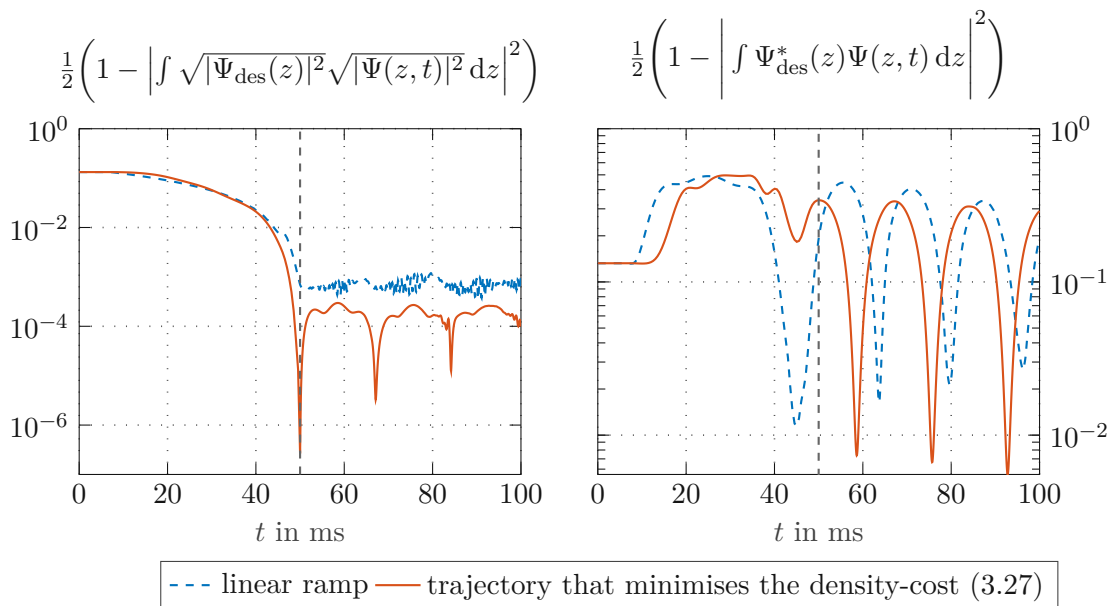
Figure 3.19: Left: Evolution of the density error. Right: Evolution of the state error, during and after the compression with a control parameter optimised with a density cost J_{density}. The grey dashed line at $t = T_t$ marks the end of the compression, which is the time horizon of the optimisation.

4 Parameter estimation from density data

Optimal trajectories for all subsequences in two different mathematical descriptions where presented in Chapter 3.4. Optimal trajectories that are calculated offline will not perform well on the experiment if used in a pure feedforward manner, since parameter inaccuracies, approximations made in the mathematical description or fluctuating quantities impair the performance of experimental results. As a result, measurement data shall be used to improve the cooling sequence directly on the experiment. There are different ways to use experimental data for adapting the pre-calculated trajectories. The first option is an online optimisation using a cost functional that contains measured quantities. While this is a very general approach, the choice of quantities to optimise is not straightforward as illustrated in the previous chapter.

The second possibility of adapting the trajectories is investigated in this chapter. By comparing experimental data to the result of the mathematical model, parameters of the model can be estimated. In this way, the model is adapted to fit the experiment, new trajectories can be calculated on the adapted model and the experimental results can be improved. In this work, a parameter estimation for the GPE is designed, but also any other mean-field description as for example the npSE could be used as mathematical model.

Since the potential $V(z,t)$ is assumed to be adjustable in the GPE (2.5) and the atom mass m is well known, the coupling constant g is chosen as parameter to be estimated. This makes sense as the coupling constant contains parameters that are not known exactly or fluctuate from experiment to experiment and g has direct influence to the speed of sound in the condensate. If one uses another mathematical description than the GPE, the choice of parameter to estimate obviously has to be reconsidered.

The adaption of the speed of sound is especially important since the chosen method of compressing and decompressing is very sensitive on the speed of excited waves. The reason for this sensitivity is the chosen method of controlling the condensate. It is only controlled by moving the walls of the box and thus excited waves have to be cancelled in the exact moment when they hit the opposite wall to compress or decompress a subsystem in an optimal way. Optimal compression or decompression therefore depends on optimal timing and the travelling time of excited waves is defined by the speed of sound in the condensate. Since the (normalised) GPE is considered as a model, the speed of sound is

$$c_{\text{1D-GPE}} = \sqrt{g_{\text{1D}}\frac{\rho(z,t)}{m}}, \qquad g_{\text{1D}} = 2Na_s\omega_\perp \tag{4.1}$$

with the theoretically known transversal confinement $\omega_\perp$ and the atom mass m. The 1D density $\rho(z,t) = |\Psi(z,t)|^2$ is constant in a homogenous box shape condensate, but in the experiment the potential shape will not be perfectly smooth. Furthermore, the particle

number N fluctuates from experiment to experiment and the s-wave scattering length a_s depends on the temperature, which can also change depending on the quality of cooling during the preparation of the condensate. Estimating the coupling constant g includes the estimation of particle number and scattering length and simultaneously adapts the speed of sound. Additionally, the GPE is not an exact description of the physical reality. The parameter adaption can thus potentially compensate also for other model errors.

In this chapter, it is shown that the coupling constant g can be estimated with a Least-Mean-Squares estimator by only using density data. The developed estimator is tested in simulation and the robustness with respect to noise and fluctuations is shown.

4.1 Linearisation of the GPE with respect to the coupling constant

The solution $\Psi(z, t)$ of the GPE at some point in time depends on the value of the coupling constant g with which it was propagated. If g changes from its nominal value by a small amount Δg, the new solution $\Psi_{g+\Delta g}(z, t)$ can be approximated in a linear fashion by

$$\Psi_{g+\Delta g}(z, t) \approx \Psi_g(z, t) + S_g^\Psi(z, t)\Delta g, \tag{4.2}$$

where $\Psi_g(z, t)$ is the wave-function propagated with the nominal coupling constant g. The quantity $S_g^\Psi(z, t)(z, t)$ denotes the derivative of the solution with respect to g and is also referred to as sensitivity function [33].

The equation for the propagation of the sensitivity function is derived by differentiating the GPE (2.5) with respect to g, which yields

$$i\partial_t S_g^\Psi(z, t) = -\frac{1}{2m}\partial_{zz} S_g^\Psi(z, t) + V_\lambda S_g^\Psi(z, t) + g|\Psi_g(z, t)|^2 S_g^\Psi(z, t)+ \tag{4.3a}$$

$$+ g(\Psi_g(z, t))^2\left(S_g^\Psi(z, t)\right)^* + |\Psi_g(z, t)|^2\Psi_g(z, t)$$

to obtain $S_g^\Psi(z, t)$ at any point in time.

Because the wave-function is normalized to one, the initial state, i.e. the ground state of the initial potential configuration, hardly depends on the atom number, which is included in the coupling constant. Furthermore, the initial potential is optimized so that the initial density fits a desired shape. Thus, it is reasonable to assume that the initial state of the condensate is known and the sensitivity $S_g^\Psi(z, t)$ is zero at $t = 0$, i.e.

$$S_g^\Psi(z, 0) = 0. \tag{4.3b}$$

Since the wave-function cannot be measured in the experiment, the sensitivity of a measurable quantity has to be calculated. A simple measurement that can be taken is the atom distribution, which corresponds to the density $\rho(z, t) = |\Psi(z, t)|^2$. As done for the solution $\Psi(z, t)$ above, the density can be linearised if g changes from its nominal value:

$$\rho_{g+\Delta g}(z, t) \approx \rho_g(z, t) + S_g^\rho(z, t)\Delta g. \tag{4.4}$$

$\rho(z, t)$

$|S_g^\rho(z, t)|^2$

t in ms
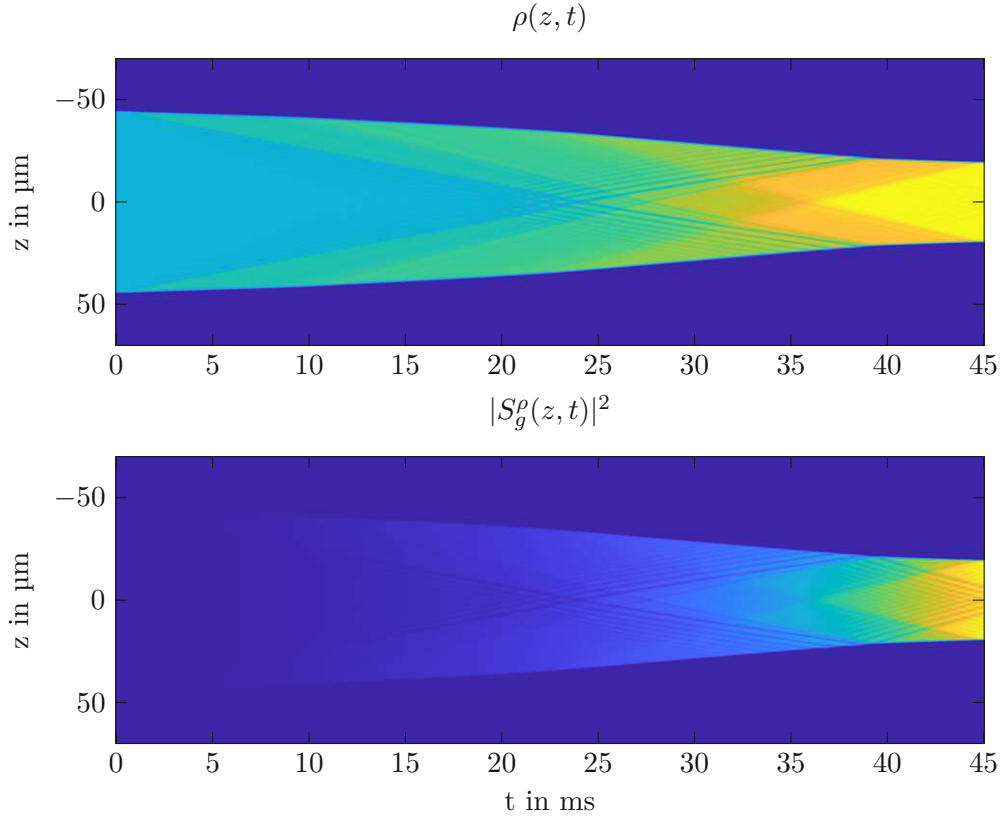
Figure 4.1: Evolution of the density $\rho(z, t) = |\Psi(z, t)|^2$ and the according sensitivity $\mathbf{S}_g^\rho(z, t)$ during the compression of a box-shaped condensate. The box is compressed from 100 to 50 μm within 45 ms. Since the initial state of the condensate is assumed to be known, the sensitivity is zero at $t = 0$.

The condensate's mean-field dynamics are described by the GPE, which is formulated with the wave-function $\Psi(z, t)$. The sensitivity function $S_g^\rho(z, t)$ of the density with respect to g is derived from the result above by

$$S_g^\rho(z, t) = S_g^\Psi(z, t)\Psi^*(z, t) + \Psi(z, t)\left(S_g^\Psi(z, t)\right)^* = 2\operatorname{Re}\left(\Psi(z, t)S_g^\Psi(z, t)\right). \tag{4.5}$$

To solve (4.3) numerically a Crank-Nicolson scheme was implemented analogous to the solver for the adjoint equation in Section 3.4. The evolution in time of the absolute value of the sensitivity function $S_g^\rho(z, t)$ for the compression of a condensate is plotted in Figure 4.1. During the transition, the sensitivity increases, and it can be seen nicely that the speed of sound restricts the sensitivity to the wavefronts of the excitations. In the middle of the condensate, the sensitivity remains zero at the beginning of the transition, and increases along the wavefronts over time.

4.2 Least-Squares Estimator

Based on the linearisation (4.2), a Least-Squares estimator (LSE) [34] for the coupling constant shall be designed. For this purpose, we define a measurement time T_meas, at which the experiment is terminated and a measurement $\mathbf{y}_\text{meas}$ is taken. The measurement is taken on a discrete grid at spatial points $\mathbf{z}_\text{grid} = [z_1, \ldots, z_M]^T$. The aim of the LSE is to find an estimate of the coupling constant $\hat{g}$ to minimise the squared error $||\mathbf{e}||_2^2$, where

$$\mathbf{e} = \mathbf{y} - \mathbf{y}_\text{meas}. \tag{4.6}$$

Here, $\mathbf{y}$ is the output of a mathematical model at $t = T_\text{meas}$ on the same discrete grid as the measurement, which corresponds to the measurement data and depends on $\hat{g}$. In this work, the GPE is used as mathematical model and the output is assumed to be the density ($\mathbf{y} = [\rho(z_1, T_\text{meas}), \ldots, \rho(z_M, T_\text{meas})]^T$). The estimator below is still formulated with a general output $\mathbf{y}$.

The output is written as $\mathbf{y} = \mathbf{F}(g)$, where $\mathbf{F}(g)$ is the propagation operator of the GPE including the calculation of the desired output quantity, if the coupling constant g is used. In the same way as already done in the previous section for the mean-field wave function and the density profile, the output can be approximated around a nominal value of g as

$$\mathbf{y}_{g+\Delta g} = \mathbf{F}(g + \Delta g) \approx \mathbf{F}(g) + \mathbf{S}_g \Delta g. \tag{4.7}$$

Note that $\mathbf{S}_g = [S_g(z_1, T_\text{meas}) \ldots S_g(z_M, T_\text{meas})]^T$ is now the sensitivity of the general output quantity on the discrete grid. Inserting this linearisation results in the quadratic approximation of the error

$$||\mathbf{e}_{g+\Delta g}||_2^2 \approx ||\mathbf{e}_g||_2^2 + 2\mathbf{S}_g^T \mathbf{e}_g \Delta g + \mathbf{S}_g^T \mathbf{S}_g \Delta g^2, \qquad \mathbf{e}_g = \mathbf{F}(g) - \mathbf{y}_\text{meas} \tag{4.8}$$

and by setting the derivative $||\mathbf{e}_{g+\Delta g}||_2^2$ with respect to Δg to zero, we get the optimal value of Δg that minimises the squared error

$$\Delta \tilde{g} = (\mathbf{S}_g^T \mathbf{S}_g)^{-1} \mathbf{S}_g \mathbf{e}_g. \tag{4.9}$$

This result is the least-squares estimation of the coupling constant, but since it is based on a linearisation at some value of g, multiple iterations are needed to solve the nonlinear problem and to fit the simulation result to the experimental data. In each iteration, the output of the mathematical model and the sensitivity is calculated with the last estimation of g (i.e. $\hat{g}_{j-1}$). The propagation operator is then linearised at this last estimation ($\mathbf{F}(\hat{g}_{j-1} + \Delta g) \approx \mathbf{F}(\hat{g}_{j-1}) + \mathbf{S}_{\hat{g}_{j-1}} \Delta g$), which results in the LSE

$$\Delta \tilde{g}_j = (\mathbf{S}_{\hat{g}_{j-1}}^T \mathbf{S}_{\hat{g}_{j-1}})^{-1} \mathbf{S}_{\hat{g}_{j-1}} \mathbf{e}_{\hat{g}_{j-1}}, \tag{4.10}$$

where $\mathbf{e}_{\hat{g}_{j-1}}$ is the error of the previous output to the measurement. The iterative estimator is written as

$$\hat{g}_j = \hat{g}_{j-1} + (\mathbf{S}_{\hat{g}_{j-1}}^T \mathbf{S}_{\hat{g}_{j-1}})^{-1} \mathbf{S}_{\hat{g}_{j-1}} \mathbf{e}_{\hat{g}_{j-1}}, \qquad \mathbf{e}_{\hat{g}_{j-1}} = \mathbf{F}(\hat{g}_{j-1}) - \mathbf{y}_\text{meas}. \tag{4.11}$$

Note that this iterative LSE uses the same measurement data in each iteration. Multiple iterations are only necessary because of the nonlinearity in the propagation operator.
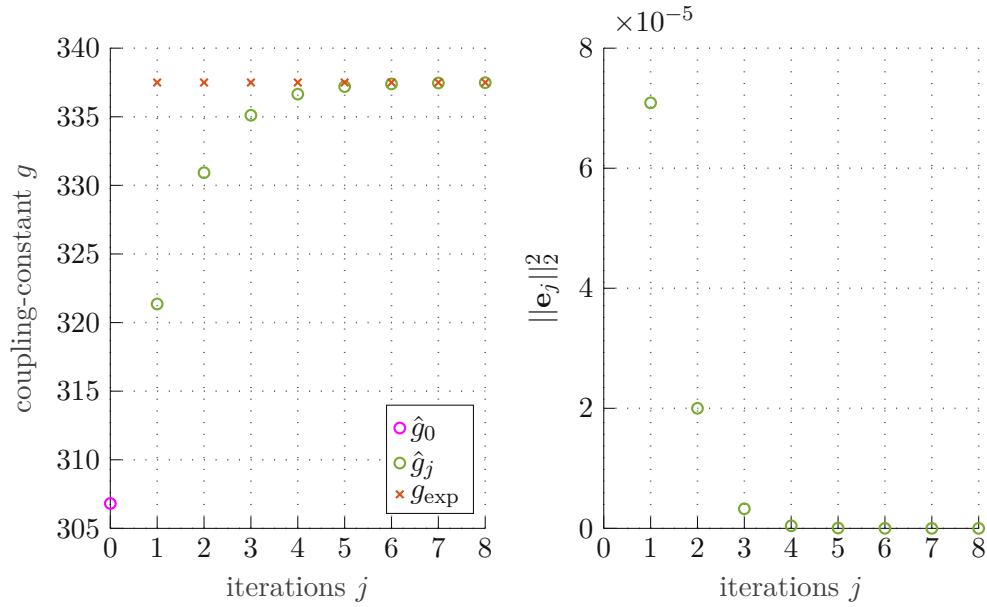
Figure 4.2: Convergence of the Least-Squares estimator (4.11) for a single measurement. GPE simulation with unknown coupling constant is used as experiment from which one measurement of the density at $T_{\text{meas}} = 10\,\text{ms}$ was used for the estimation. The estimated coupling constant $\hat{g}_j$ (left) and the squared error $||\mathbf{e}_{\hat{g}_j}||_2^2$ (right) are plotted over the iterations.

To test the Least-Squares estimator, the GPE with coupling constant g_{exp} was used to generate pseudo measurement data. This coupling constant is assumed to be unknown by the estimator and the initial guess $\hat{g}_0$ was chosen so that $g_{\text{exp}} = 1.1\hat{g}_0$. Figure 4.2 shows the convergence of $\hat{g}_j$ for the compression of a condensate. The estimator converges towards g_{exp} and within 6 iterations an estimation error in the coupling constant of $0.0312\,\%$ is achieved. For this estimation, the condensate was measured at $T_{\text{meas}} = 10\,\text{ms}$, but also other points could be chosen. The measurement time has influence on the sensitivity and the squared error of the nonlinear propagation (4.6). Thus, the convergence of the estimator highly depends on the choice of the measurement time.

In Figure 4.3, the squared error $||\mathbf{e}_g||_2^2$ according to (4.6) is plotted as a function of Δg for three different measurement times T_{meas} together with the quadratic approximation (4.8) of the nonlinear dependence (4.6) at the initial guess $\hat{g}_0$ for $T_{\text{meas}} = 10\,\text{ms}$, $T_{\text{meas}} = 20\,\text{ms}$ and $T_{\text{meas}} = 40\,\text{ms}$. The minima of the nonlinear problem exactly correspond to the step-size Δg needed to match the experimental coupling constant. Near the minima, the quadratic approximation fits the nonlinear problem really well. For small values of T_{meas} at the beginning of the compression, the estimation is quite robust with regard to the initial guess, but both the error in the density and the sensitivity are very small. At later measurement times, the error and the sensitivity are higher, but multiple local minima start to appear. If the initial guess $\hat{g}_0$ is not expected to be close to the true value of the experimental coupling constant, a good strategy is to start with measurement times T_{meas} rather at the beginning of the transition. Once a relatively good estimation is achieved,
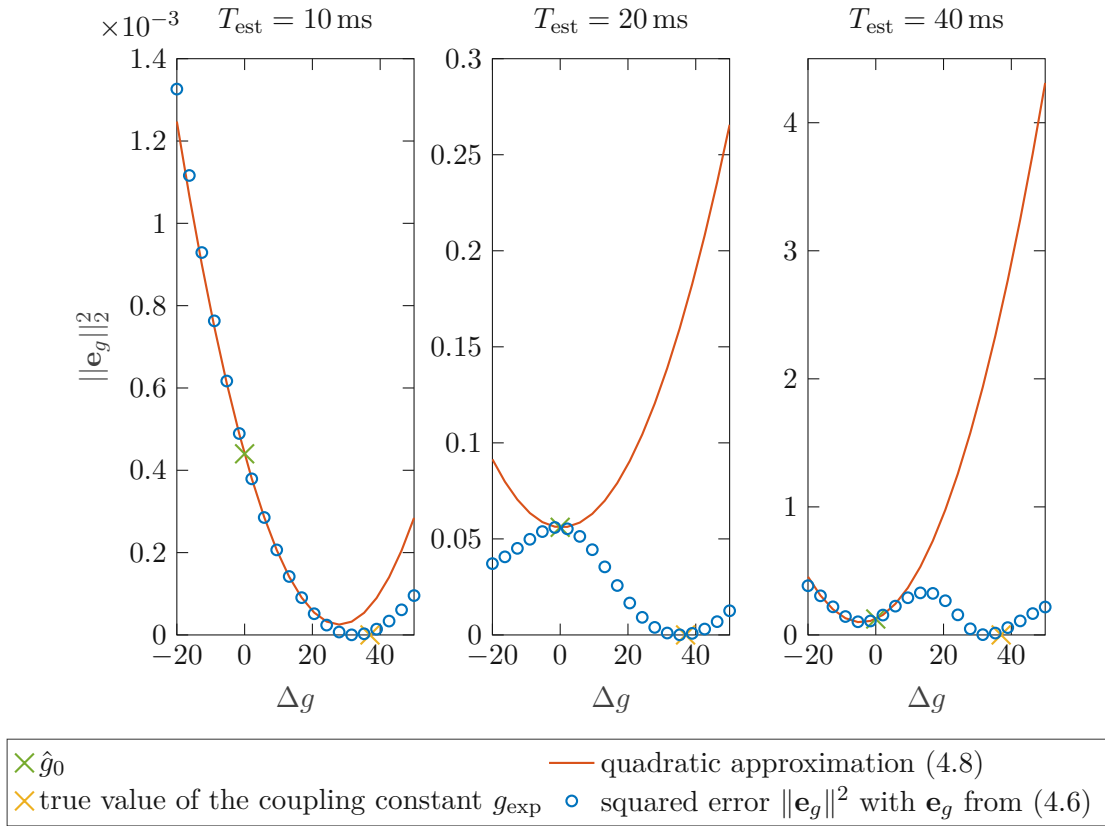
Figure 4.3: Squared error $\|\mathbf{e}_g\|_2^2$ (4.6) and its quadratic approximation (4.8) linearised at the initial guess $\hat{g}_0$ for different measurement times T_{meas}.

further iterations can be done with measurements at later times of the transition that are more sensitive to parameter variations. One could also include multiple measurements with different measurement times T_{meas} in one iteration. Simulation data must then be taken at the same points and concatenated in the same way.

4.3 Iterative Least-Squares estimator with exponential memory

Experimental data is subject to quantum noise and other stochastic fluctuations (e.g. fluctuations of the density, varying atom number or changing temperature of the condensate) which makes the estimation of parameters from a single measurement impossible and information of multiple measurements is needed. These measurements can be taken either at the same measurement time or at different measurement times, whereby the use of measurements from different measurement times can enhance the result of the estimator and gives more insight into the dynamics of the condensate. To adapt the estimation to slow changes, an iterative Least-Squares estimator with exponential memory is used. This estimator takes into account the already obtained information of multiple measurements and includes new measurements iteratively. If a number of N_{meas} measurements are

available, an estimated coupling constant $\hat{g}$ is obtained minimising the weighted squared error

$$\sum_{j=0}^{N_{\text{meas}}} q^{N_{\text{meas}}-j}||\mathbf{e}_{g_j}||_2^2, \qquad \mathbf{e}_{g_j} = \mathbf{y}_j - \mathbf{y}_{\text{meas}}^j \tag{4.12}$$

with the memory factor $q \in (0,1]$ and the output
$\mathbf{y}_j = [\rho(z_1, T_{\text{meas}}^j), \ldots, \rho(z_M, T_{\text{meas}}^j)]^T = \mathbf{F}_j(\hat{g})$ as a result of the GPE simulation. The further in the past a measurement lies, the less impact it will have on the estimation. The iterative Least-Squares estimator with exponential memory [34] is written as

$$\mathbf{k}_j = (\mathbf{P}_{j-1}\mathbf{S}_j^T)(q\mathbf{E} + \mathbf{S}_{\hat{g}_{j-1}}\mathbf{P}_{j-1}\mathbf{S}_{\hat{g}_{j-1}}^T)^{-1} \tag{4.13a}$$

$$\mathbf{P}_j = \left(\mathbf{P}_{j-1} - \mathbf{k}_j\mathbf{S}_{\hat{g}_{j-1}}\mathbf{P}_{j-1}\right)\frac{1}{q} \tag{4.13b}$$

$$\hat{g}_j = \hat{g}_{j-1} + \mathbf{k}_j\mathbf{e}_{g_j}, \qquad \mathbf{e}_{g_j} = F_j(\hat{g}_{j-1}) - \mathbf{y}_{\text{meas}}^j, \tag{4.13c}$$

where $\mathbf{k}_j$ and $\mathbf{P}_j$ are abbreviations, although $\mathbf{P}_j$ can be interpreted as the covariance of the estimation error. This estimator minimises (4.12) if the initial value of $\mathbf{P}$ is chosen as $\mathbf{P}_0 = \alpha\mathbf{E}$ with a big value for the tuning parameter α. The smaller α, the more influence the initial value $\hat{g}_0$ has on the estimation. If the memory factor q is chosen to one, all measurements are equally weighted and (4.13) describes the iterative LSE for multiple measurements. The full algorithm for the iterative LSE with exponential memory is summarized in Algorithm 2. For validating this approach, Gaussian density noise with a

---

Algorithm 2 Iterative Least-Squares estimator with exponential memory

Prepare the initial state of the experiment
Adapt potential $V(z,t)$ of the simulation to the experiment
Initialize: $j = 0$, $\hat{g}_0$, $\mathbf{P}_0 = \alpha\mathbf{E}$, $q \in (0,1]$
for desired number of measurements **do**
    $j \leftarrow j + 1$
    Run the experiment and take a measurement $\mathbf{y}_{\text{meas}}^j$ at T_{meas}^j
    Propagate the GPE (2.5) to get $\Psi_{\hat{g}_j}(z,t)$
    Calculate the density as output: $\rho(z,t) = |\Psi_{\hat{g}_j}(z,t)|^2$
    Calculate the error on the discrete grid:
        $\mathbf{e}_{g_j} = \mathbf{y}_j - \mathbf{y}_{\text{meas}}^j$, $\mathbf{y}_j = [\rho(z_1, T_{\text{meas}}^j), \ldots, \rho(z_M, T_{\text{meas}}^j)]^T$
    Propagate the PDE (4.3) of the sensitivity function $S_{\hat{g}_j}^\Psi(z,t)$
    Calculate $S_{\hat{g}_j}^\rho(z,t)$ from (4.5)
    Update $\mathbf{P}_j$, $\mathbf{k}_j$, $\hat{g}_j$ following (4.13)
end for

---

variance (i.e. σ^2) of 10 % of the peak density was added to the output $\mathbf{y}_{\text{meas}}$ of the GPE experiment and the number of atoms N was drawn randomly from a normal distribution with a variance of 10 % of the nominal atom number for each experiment, which imposes fluctuations of the coupling constant. As for the LSE, the compression of a condensate is used as test scenario. Measurements are taken every 2 ms during the compression, and

used as iterative measurements $\mathbf{y}^j_{\text{meas}}$. Since a nonlinear minimisation problem has to be solved every iteration, 3 sub-iterations are made every iteration without updating the measurements. In Figure 4.4, the convergence of the estimated coupling constant is plotted over the measurement time, which corresponds to the iterations j of the estimator. Comparing these results to the convergence of the LSE (Figure 4.2) that estimated the coupling constant from one measurement without noise, it can be seen that more iterations are needed to estimate the expectation value of the coupling constant correctly.

In conclusion it can be said that the coupling constant in the GPE can nicely be estimated with a Least-Squares estimator by only using density information from one measurement if no measurement noise or parameter fluctuations are present. The correctly estimated coupling constant can then be used to adapt the mathematical description and further improve the control parameter in the adapted model. The resulting new trajectory also improves results on the experiment, since the mathematical model is well adapted to the reality.

In the real-world experiment [35], we still could not perform an estimation of the coupling constant in this automatised way. The reasons for this is that the presented estimator only works well if the potential $V(z,t)$ in the GPE matches the actual potential in the experiment really well. While the initial potential in the experiment is optimised to fit a desired shape, the evolution over time of the potential is not well known. For the compression of a box shape condensate, the not perfectly box-shaped initial state is compressed by switching on whole rows of the DMD. This method produces spatial and temporal discretization as described in Section 3.5. Furthermore, the optical system of the setup is not perfectly identified and the effect of turning on individual pixels or rows is not exactly known. Therefore, the box width at a certain point in time, the steepness of the walls or other effects in the region of the condensate's edges are not fully under our control. A first approach to this problem could be ground-state measurements or even optimisation of intermediate pixel configurations to gain more insight into the evolution over time of the potential $V(z,t)$.

In Section 3.7, it was shown that a BFA with only using density data misses phase information to suppress mean-field excitations after the compression of a condensate, while this chapter uses only density data to estimate a parameter and improve the result. The fundamental difference of those two approaches is the use of model knowledge in the design of the parameter estimator. Following this rational, a promising approach to suppress mean-field excitations in the experiment would be the estimation of model parameters directly on the experiment. After adapting the parameters of the mathematical description, the trajectories can then be improved on the adapted model without limitation of computation time since the experiments are anyway terminated for every new measurement. If reduction of the computation time is desired, one can think of approximating the nonlinear dynamic optimisation problem (3.2) near the beforehand calculated optimal trajectory to a quadratic optimisation problem.
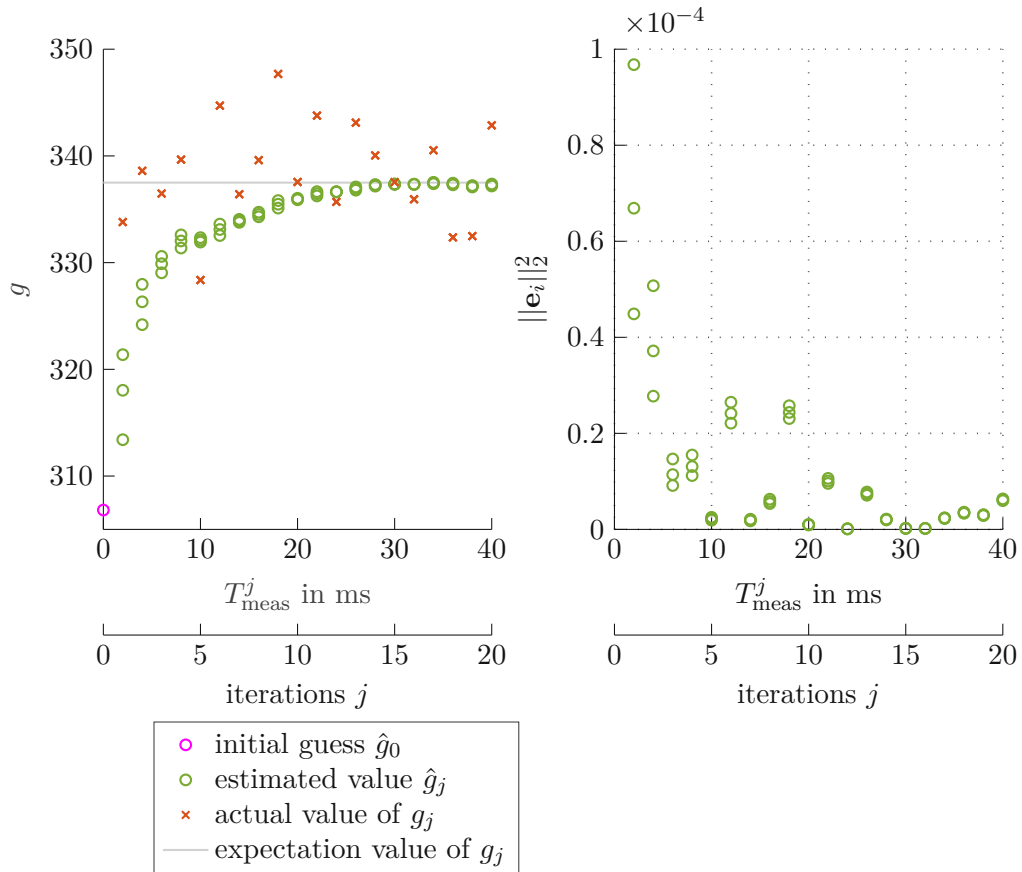
Figure 4.4: Convergence of the estimation of the coupling constant (left) and the squared density error (right) with an iterative Least-Squares estimator with exponential memory. The measurement data was generated by GPE simulations with unknown, fluctuating coupling constant to imitate changing atom numbers in the experiment. Measurements where taken every $2\,\mathrm{ms}$ at ascending measurement times T_{meas}^{j} and at every iteration, three sub-iterations where performed. To imitate measurement noise and density fluctuations, a Gaussian noise with $\sigma^2 = 10\,\%$ of the maximum value of the density was added to the measured density.

5 Stochastic properties of thermal states during the QFTM sequence

As stated in Chapter 2, thermal and quantum fluctuations are not described in mean-field theories such as the GPE or the npSE. To investigate the thermal effects that the QFTM sequence in Chapter 1 has on the three compartments S, P and B and to choose parameters for the coupling phase, a more advanced description of the condensate is necessary. Therefore, a ensemble of thermal initial states is prepared using the sGPE (see Section 2.4) and than propagated with the GPE to go beyond mean-field theory and obtain the evolution of stochastic properties in the condensate.

So far, the evolution of the mean field during the compression of a condensate was discussed in detail in Chapter 3. The parameter controlling the evolution of the potential $V(z, t)$ was optimised so that no mean-field excitations remain after each quantum thermal primitive of the cooling cycle. This chapter shall investigate the evolution of stochastic properties during one cooling cycle. The results with linear ramps as control parameters are compared to those using trajectories that where optimized in the mean-field description. To get insight into thermal properties, two stochastic properties are evaluated during the QFTM sequence. Analogous to the discussion of mean-field optimisation, the compression of a condensate is discussed before the whole QFTM sequence is studied.

5.1 Compression of a thermal condensate

The first stochastic property that one can calculate from a thermal state is the global density fluctuation $\delta\rho$ defined in (2.17). The evolution of this quantity during the compression of a condensate is plotted in Figure 5.1. The result with a linear ramp is compared to the result with the trajectory that minimises mean-field excitations. It can be seen that the density fluctuation rises as the condensate is compressed. This raise in fluctuations is expected since the aim of compressing the condensate is rising its temperature. The final value of the density fluctuation is higher for the linear ramp than for the trajectory that is optimal in the mean-field description. This relation supports the assumption that a trajectory that minimises mean-field excitations will also alleviate additionally excited fluctuations and undesired heating of the condensate. Not only reaches the density fluctuation a higher value for the linear compression directly after the compression at $t = 45$ ms, but it also rises further after the compression. In contrast to the linear compression, density fluctuations hardly increase further after the optimal compression. With further rise of fluctuations, one can observe a decay of mean-field excitations that are remaining after a linear compression. This phenomenon is a consequence of the nonlinear interaction between the mean field and the fluctuations in the GPE. Remaining mean-field excitations are thereby converted to density fluctuations over time.

linear compression   optimal compression
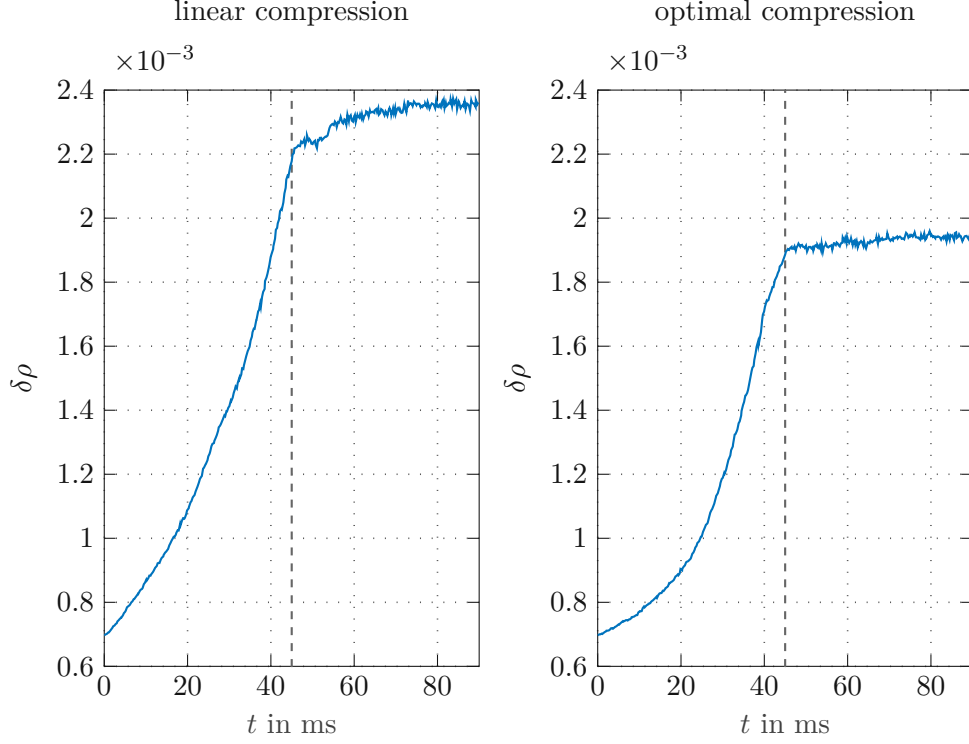
Figure 5.1: Density fluctuations $\delta\rho$ as defined in (2.17). The resulting evolution is compared for a linear compression and the compression that minimises mean-field excitations. The dashed line indicates the end of the transition.

	λ_c	T
initial state	14.982 µm	42.0372 nK
optimal compression	3.832 µm	103.9433 nK
linear compression	6.059 µm	164.3287 nK

Table 5.1: Thermal coherence length and temperature before and after the compression of a condensate. The phase correlation functions $C_D(\Delta z)$ are plotted in Figure 5.2.
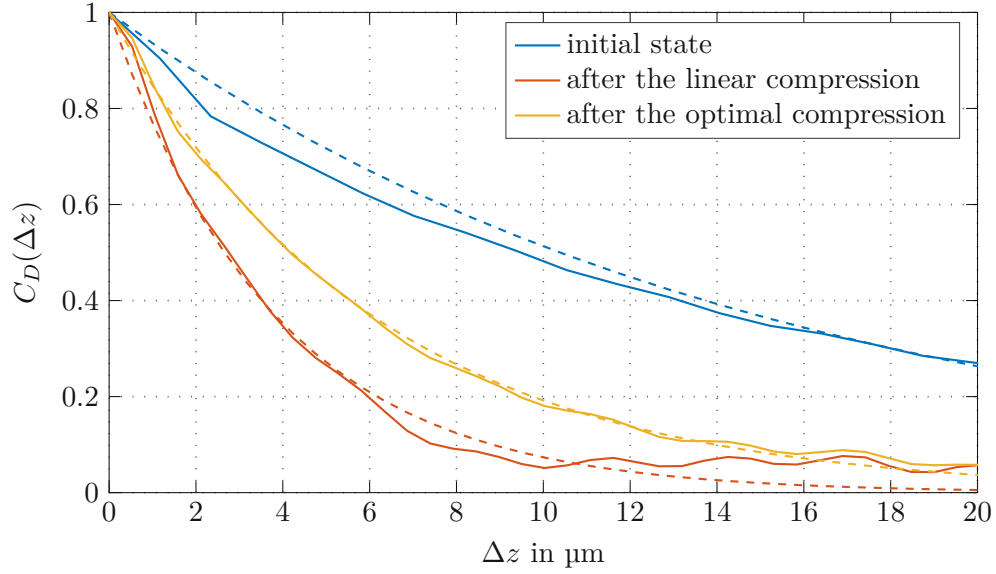
Figure 5.2: Integrated phase correlation $C_D(\Delta z)$ (2.18) of the initial state and after the linear and the optimal compression. The analytic solution (2.20) was fitted to find the coherence length λ_C and the associated temperature T of the thermal state, which are given in Table 5.1.

The second stochastic property that can be looked at to gain insight into the thermal properties during compression is the phase correlation function $C_D(\Delta z)$ defined in (2.18). For a fully thermalised and homogenous condensate, this correlation decays with the thermal coherence length λ_c, which is indirect proportional to the temperature. In Figure 5.2, the phase correlation is plotted for the initial thermal state before compression and 30 ms after the compression both with a linear ramp and the optimal trajectory as control variable. Especially for the linear ramp, the resulting state is not expected to be fully thermalized and homogenous. Nevertheless, the decay of phase correlation gives some insight into the temperature of the condensate. To quantify temperature in this context, the resulting decay of the phase correlation is fitted to the analytic result (2.20) to measure the thermal coherence length and thus assign a temperature value according to $T = 2\hbar \cdot 10^3 \mathrm{rad/s} \tilde{\rho} N/(\tilde{m} k_b \tilde{\lambda}_C)$. The fitted curves are plotted as dashed lines together with the simulation results. The phase correlation of the initial state nicely follows the exponential decay corresponding to a temperature of 42 nK. The phase correlation after the transition decays faster and thus has a higher temperature in this context. Comparing the linear compression to the optimal compression, the result for the optimal trajectory results in a slower decay of phase correlation, a higher coherence length and thus a lower temperature. Notice the remaining correlations of the linear ramp of long distance, which also indicates that the condensate is not fully thermalized. The condensate reaches a temperature of 104 nK if the optimal trajectory is used and 164 nK if a linear ramp is used. These results once more support the presumption that trajectories that minimise mean-field excitations also alleviate additional heating of the condensate.

The compression ratio has influence on the achieved temperature rise in the condensate and therefore could be a crucial parameter to allow for effective coupling after the compression. To investigate this relation, the condensate was compressed from $w_0 = 100\,\mu\text{m}$ to $w_1 = 50\,\mu\text{m}$, $w_1 = 62.5\,\mu\text{m}$ and $w_1 = 75\,\mu\text{m}$ within $45\,\text{ms}$, which results in compression ratios of $r_{\text{comp}} = 1/2$, $r_{\text{comp}} = 3/8$ and $r_{\text{comp}} = 1/4$ ($r_{\text{comp}} = ()w_0 - w_1)/(w_0)$). Figure 5.3 shows the evolution of the density fluctuation during three different compression scenarios. It can clearly be seen that a higher compression ratio results in higher fluctuations in the density and thus points towards a higher temperature of the condensate. The second value to investigate the rise in temperature is the phase coherence length. The decay of phase correlation for all three compression ratios are plotted in Figure 5.4. For the same value of density higher temperature corresponds to smaller phase coherence length. Considering the different densities in the middle of the condensate the following temperature values can be assigned:

$$r_{\text{comp}} = \frac{1}{2}, \; \lambda_c = 3.6404\,\mu\text{m}, \; T = 387.6709\,\text{nK}$$

$$r_{\text{comp}} = \frac{3}{8}, \; \lambda_c = 5.2564\,\mu\text{m}, \; T = 212.1611\,\text{nK}$$

$$r_{\text{comp}} = \frac{1}{4}, \; \lambda_c = 6.0425\,\mu\text{m}, \; T = 146.4712\,\text{nK}$$

For choosing the right compression ratio for effective coupling, the coupling phase could be studied on its own to determine the required temperature difference in the two condensates. The compression ratio can then be chosen subsequently according to the desired temperature rise.

To investigate the amount of undesired energy that is brought into the condensate by actuation, another subsequence of the whole QFTM sequence is studied. The condensate is compressed after decompression and stochastic properties are evaluated. Ideally, no additional heat should be introduced and both density fluctuations and the thermal coherence length should reach their initial value. Figure 5.5 shows the evolution of density fluctuations during this protocol. It can be seen that the optimal trajectory results in far less fluctuations than the linear ramp, but additional heat introduction cannot completely be prevented by this optimal trajectory.

5.2 QFTM sequence for a thermal condensate

Analogous to the full QFTM sequence at zero temperature, the compartments S, P and B are decoupled for the initial configuration and thermal states for all three compartments are prepared with the sGPE separately from each other and the compartments are assumed to have the same temperature for the initial state. The evaluation of one QFTM sequence for a thermal state is computationally very expensive, since all thermal initials have to be propagated by their own. Trying out a large number of configurations or optimising the coupling parameters (e.g. the final wall width for coupling or the duration of holding two condensates near each other) would require very time consuming calculations and is beyond the scope of this thesis. Therefore, coupling parameters were set using an educated guess: coupling is expected to happen when the mean-field wave-functions of
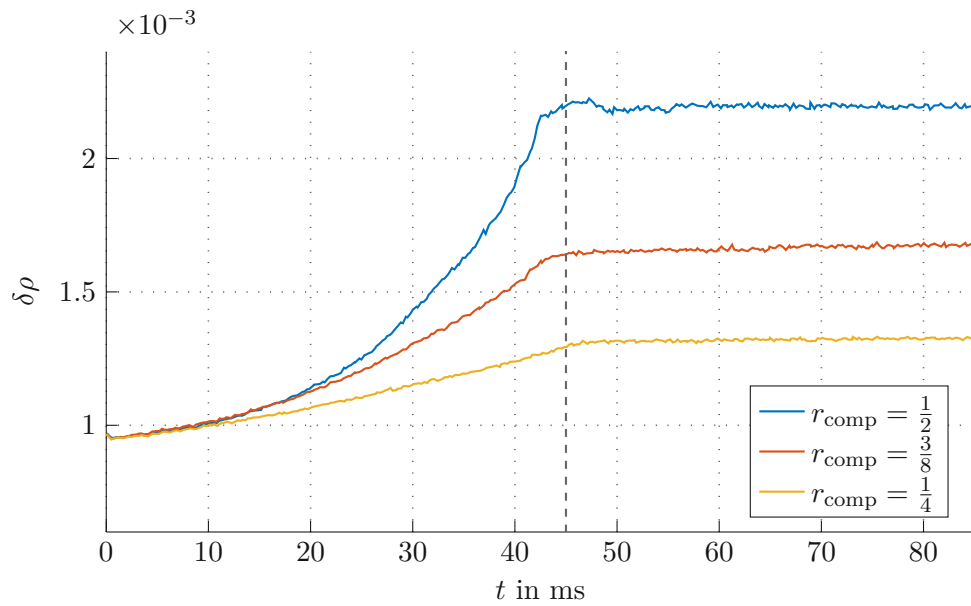
Figure 5.3: Evolution of density fluctuation for three different compression ratios. The condensate is compressed within 45 ms and than the potential $V(z,t)$ is held constant for another 45 ms.
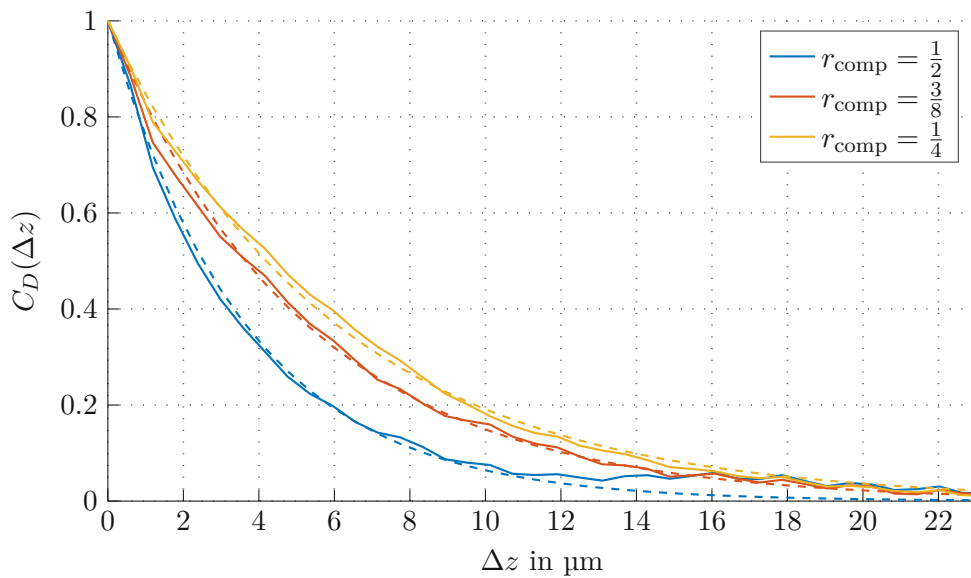

Figure 5.4: Phase correlation after the compression with three different compression ratios r_{comp}
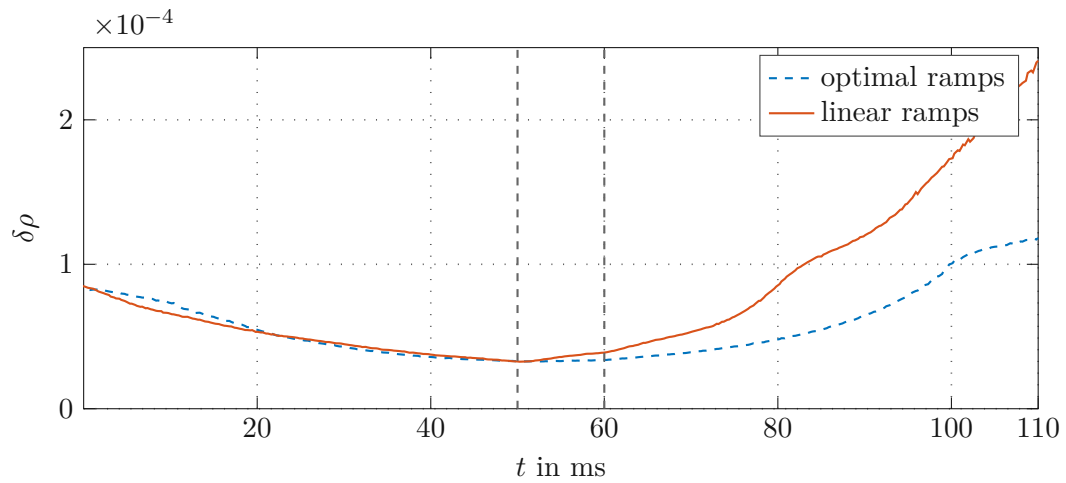
Figure 5.5: Evolution of the density fluctuations during decompression and compression with linear ramps and mean-field-optimal trajectories.

two subsystems do overlap, while their densities are mostly disjoint to limit their mutual disturbance. This approach was followed and the wall width for coupling two condensates was set to $0.5\,\mu m$. The coupling of two condensates would be observable in an exchange of fluctuations and a shift of the thermal coherence lengths. The hotter of both condensates is expected to be cooled and energy would be shifted to the initially cooler one.

As seen in the evolution of the density fluctuations of the whole QFTM sequence in Figure 5.6, no coupling is happening in the coupling phase and the system S remains unchanged during the whole cycle. We found that it is not a straightforward task to find the right parameters so that coupling is happening without combining the condensates. Coupling might only take place if the wall width is decreased to a value very close to zero. Additional lowering of the barrier could help to couple two condensates, but further exploring the coupling phase would most likely need additional computational power or a more effective implementation of propagating thermal states. Such investigations remain to be studied in future work.

At this point, differences to [7] should be mentioned, where coupling was indeed observed. In that work, the field operator is decomposed in the Gross-Pitaevskii (GP) density profile, and density and phase fluctuations. The Lieb-Lininger Hamiltonian is expanded up to second order and an effective Hamiltonian that depends on the GP profile is used as mathematical description for density and phase fluctuations. In other words, equations for small fluctuations that are added on top of the GP profile are derived. This Luttinger Liquid approach is not that computationally expensive and differs fundamentally from the strategy of propagating thermal initials, which was followed in this work.

Furthermore, the coupling process in [7] was modelled by merging two initially completely decoupled condensates. The condensates are already very close to each other before the coupling and decoupling is performed by adding the interaction part of the Hamiltonian in a linear manner, neglecting the precise spatial details. In this way, coupling is tuned by defining the initial overlap of the condensates, but it was not discussed how to get the

optimal	λ_C	T	**linear**	λ_C	T
S	6.2612 µm	75.2214 nK	S	6.9409 µm	67.8441 nK
P	5.8962 µm	79.8773 nK	P	6.0881 µm	77.347 nK
B	13.2567 µm	35.5272 nK	B	2.3866 µm	196.4834 nK

Table 5.2: Thermal coherence length and temperature in the three compartments after decompressing B, which is the first sequence of the full QFTM cycle. The phase correlation function $C(z, z')$ and $C_D(\delta z)$ are plotted in Figure 5.7.

condensates in this state or what protocol the external potential has to follow for coupling. Regarding the compression or decompression of a condensate, the time-dependent GP profile was assumed to stay homogenous during the transition without exciting waves by actuating the external potential.

Even though coupling cannot be studied in detail with the available setup of this work, the optimal QFTM sequence still performs better than the linear one in the sense that far less additional heating is introduced during one cycle. In comparison to the linear cycle, the use of optimal trajectories can reduce the final density fluctuations by 64 %.

The phase correlation after the decompression of the bath, which is the first subsequence of the QFTM sequence, is plotted in Figure 5.7. In the phase correlation $C(z, z')$, it can be seen that the condensate is roughly homogenous after the optimal decompression of B. The temperature that can be assigned to the bath B is 35 nK, while the piston P and the system S remain quasi at the initial temperature of around $75 - 80$ nK. The phase correlation $C(z, z')$ shows that the condensate in B is not at all homogenous or in ground state after the linear decompression. Thus, it does not make sense to assign a single temperature value to the bath B after the linear decompression. Nevertheless, the exponential decay was fitted to the integrated phase correlation $C_D(\Delta z)$. The resulting temperature value can be interpreted as a kind of mean temperature of the compartment, since the calculation of C_D includes an averaging effect due to the integration along diagonal lines of $C(z, z')$. If one would hold the potential V constant after decompression and wait for all bulk excitations to dissolve, the coherence length most likely would decrease further.

The evolution of the mean density of the thermal state is given for the optimal and the linear QFTM sequence in Figure 5.6. The decay of mean-field excitations that comes with a rise in fluctuations can be observed once more in the plots for the thermal condensates. In summery, it can be said that the use of trajectories that minimise mean-field excitations alleviates additional heating during compression and decompression and prevents further rise in fluctuation after the transitions.
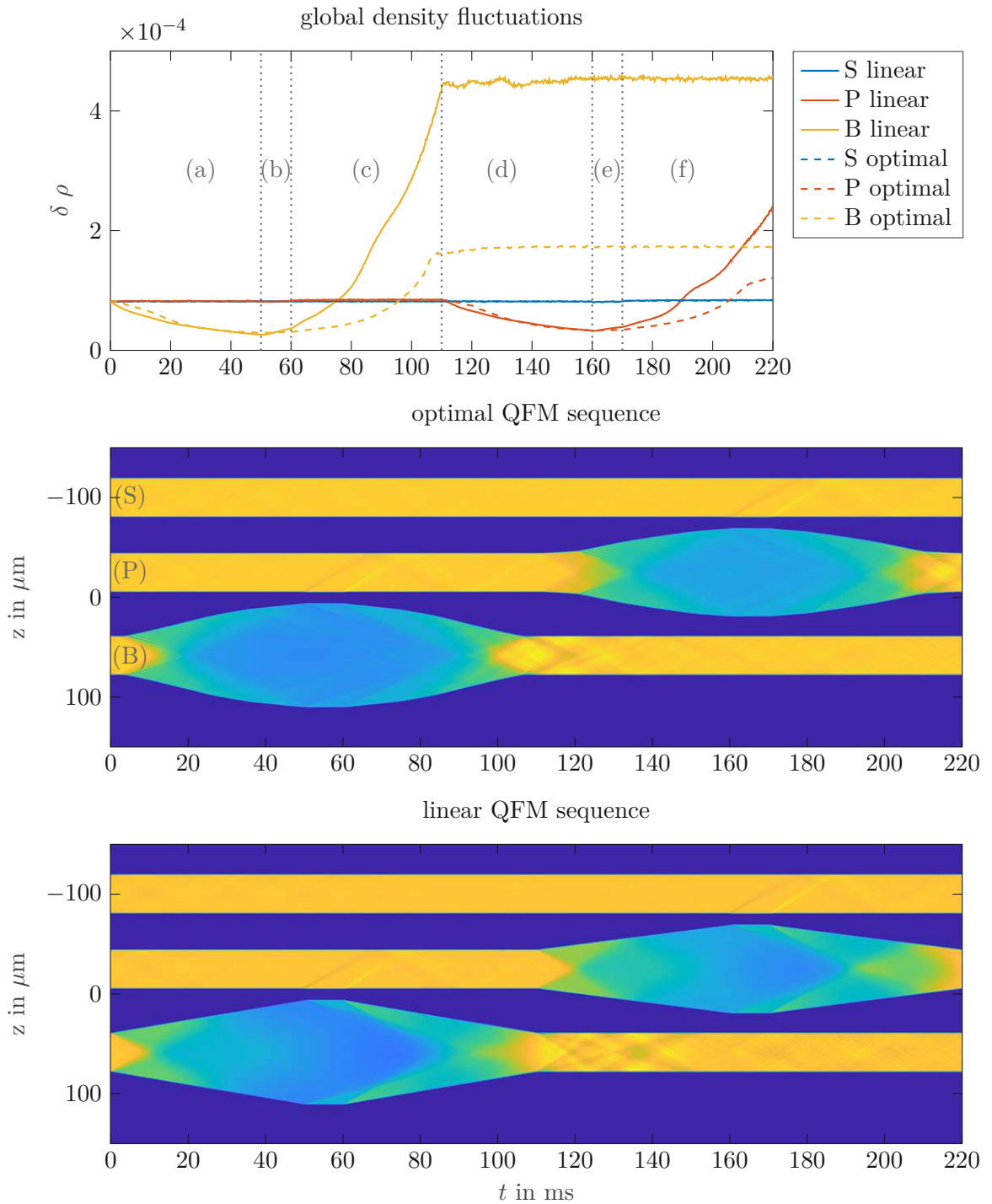
Figure 5.6: Evolution of the density fluctuations and the mean density during one cooling sequence: (a) decompression of B (b) coupling P and B (c) compression of B (d) decompression of P (e) coupling S and P (f) compression of P.
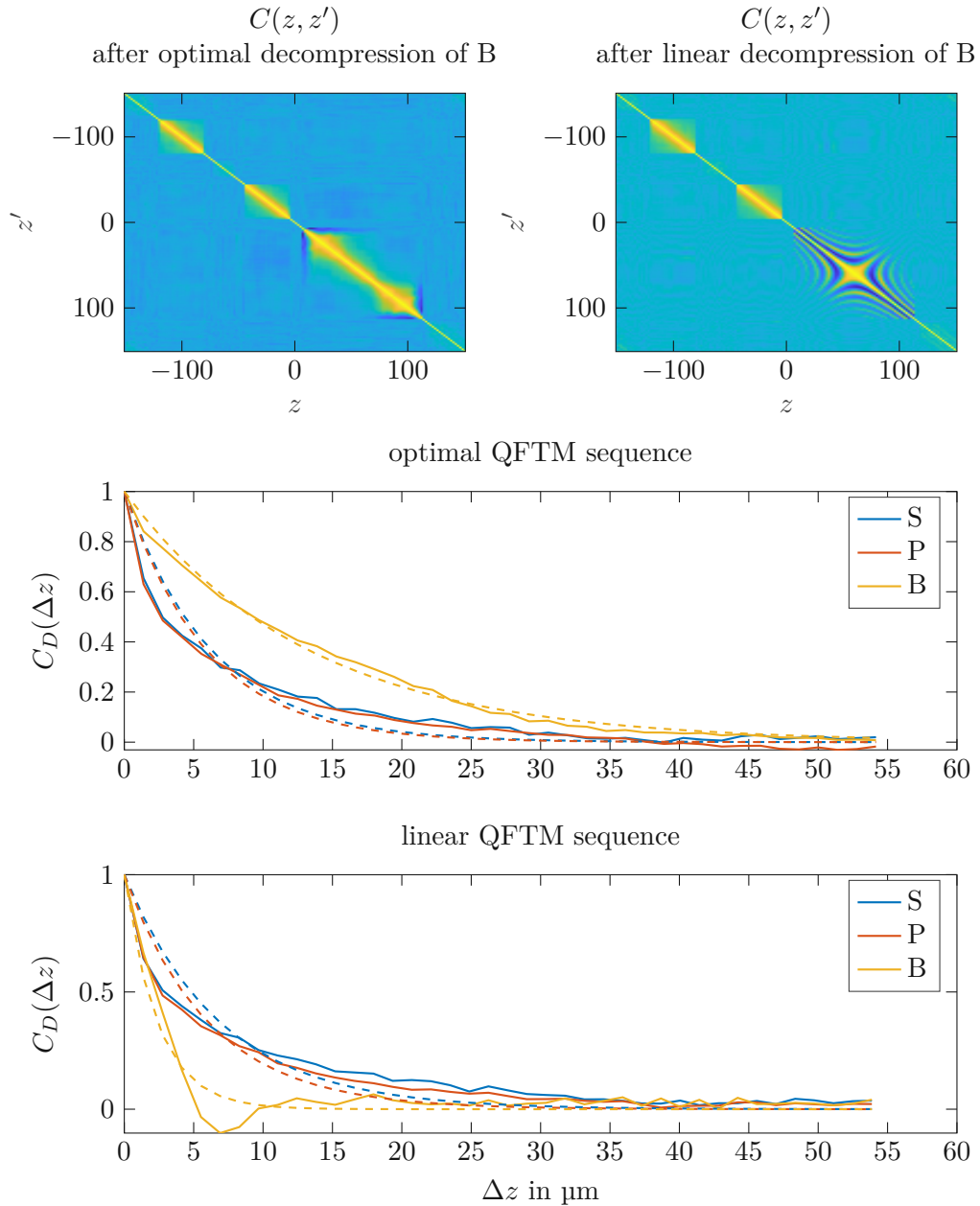
Figure 5.7: Phase correlation after optimal and linear decompression of B, which is the first sequence of the full QFTM cycle. The phase coherence length of the fitted exponential decay and resulting temperatures are given in Table 5.2

6 Conclusion and Outlook

This work studied optimal control strategies for quantum field thermal machines (QFTMs) using BECs in the special framework of one dimensional box-shaped condensates. This restricted framework was chosen because of simple realisation in the considered experiment [15, 35]. An optimal protocol for the potential was developed to perform the cooling sequence of a QFTM as suggested in [7].

In order to find a suitable mathematical description for the condensate both at zero temperature and at finite temperature, an overview of common models was given in Chapter 2. We found that the mean field is well described by the one-dimensional Gross-Pitaevskii equation (1D-GPE) if densities are not too high. The nonpolynomial Schrödinger equation (npSE) is a more accurate description of the experiment that is not so broadly studied as the GPE. To investigate thermal states, we chose to prepare thermal initials using stochastic GPE approaches and propagating them in time using the GPE.

In Chapter 3, optimal control schemes were investigated in both mean-field descriptions, whereby we compared two different approaches for solving the optimisation problem, the first one being the solution of the full dynamic optimisation problem by using functional derivatives without restricting the search space (referred to as indirect optimisation approach (IOA)). Based on the work in [11, 12, 25], where optimal control strategies for the GPE were developed, the required equations were derived for the npSE and optimal trajectories for the QFTM sequence were calculated. We found that optimisation in the npSE and the GPE give similar results if the condensate is only slightly compressed and density profiles in the condensate are not too high, but for more drastic compressions the optimal trajectories differ significantly, since the speed of sound in GPE cannot be adapted to the npSE by the effective coupling constant anymore. These results of the IAO were then compared to a basis function approach (BFA), in which the control variable is composed of basis functions to restrict the search space and reduce the optimality problem to finite dimensions. The resulting static optimisation problem was solved using non-gradient-based algorithms. We also studied two different cost functionals, namely a state cost and an energy cost and found that the use of the energy cost results in less function evaluations and less oscillations in the mean field after the optimal transition. Furthermore, the BFA with 8 ansatz functions reaches comparable good results as the IOA if the energy cost is used, which opens the possibility of performing either black-box or also model-based optimisation directly on the experiment. In this work, a Quasi-Newton optimisation without gradient information was used, which resulted in 65 function evaluations until reaching sufficiently low cost values. Finally, the optimal control of a full QFTM cycle was investigated using the IOA.

Since the real world experiment is not perfectly known and varying parameters impair the performance, it is favourable to use measurement information instead of using the precalculated trajectories in a pure feedforward manner. Besides the mentioned approach

of online optimisation with a BFA, one can recursively adapt the mathematical model based on measurements on the experiment. Following this consideration, an iterative least-squares estimator (LSE) was designed in Chapter 4, which uses density measurements to iteratively estimate the coupling constant of the GPE. Estimating a correct coupling constant is particularly important because it defines the observed speed of sound, which is essential for the box-shaped potentials with moving walls in this thesis.

The simple LSE, which only uses density data at one point in time, could correctly estimate the coupling constant in simulations and within 6 iterations an estimation error of $0.0312\,\%$ is achieved. By using an iterative LSE with exponential memory, the estimation error is sufficiently small after 20 iterations even if significant measurement noise and a fluctuating coupling constant are considered.

The design of a quantum field thermal machine requires a mathematical description of the condensate at finite temperature. In Chapter 5, the propagation of thermal initial states were chosen to investigate the cooling sequence with thermal states. The resulting density fluctuation and phase correlation was calculated before end after the compression. During the compression, density fluctuations rise while the thermal coherence length decreases, which corresponds to the expected and desired rise in temperature. Ideally, the temperature should drop to its initial value after decompressing the condensate again and additional heating is unwanted. The trajectory that is optimal in the mean field also causes far less additional density fluctuations during the transition and a higher thermal coherence length (i.e. a smaller temperature) than a linear transition. If mean-field excitations are remaining after a transition, they will decay in time due to nonlinear interaction, causing additional density and phase fluctuations and heating the condensate. The use of optimal trajectories could not completely prevent the introduction of additional heat, but significantly reduce undesired heating. The presumption that the minimisation of mean-field excitations can alleviate the problem of additionally introduced heat during actuation therefore turned out to be valid. Due to the expensive computational costs of propagating thermal initial states, several parameters that define the coupling process, including the wall width and wall height during coupling, the time span for coupling and also the compression ratio, are not explored in detail in this work. These parameters were set using educated guess and further optimisation would most likely need a more effective implementation or additional computational resources. The coupling process of two condensates therefore remains to be studied in future work.

In conclusion it can be said that mean-field excitations could be strongly suppressed by optimal trajectories and it was shown that these optimal trajectories also alleviate additional heating in thermal states. The quantum field thermal machine was studied very carefully in the restricted framework of box-shaped potentials and the realisation of arbitrary potential shapes will open many more possibilities in the future. The possibility of realising arbitrary potential shapes could also allow cooling protocols that are less sensitive to the speed of sound. Furthermore, the simple protocol of moving walls implies a minimum control time and optimal compression cannot be performed faster than this time. Alternative protocols could introduce momentum at any position and optimal transitions could possibly be executed much faster.

Bibliography

[1] I. M. Georgescu, S. Ashhab, and F. Nori, "Quantum simulation," *Reviews of Modern Physics*, vol. 86, no. 1, 153–185, 2014.

[2] V. Giovannetti, S. Lloyd, and L. Maccone, "Advances in quantum metrology," *Nature Photonics*, vol. 5, no. 4, 222–229, 2011.

[3] T. D. Ladd, F. Jelezko, R. Laflamme, Y. Nakamura, C. Monroe, and J. L. O'Brien, "Quantum computers," *Nature*, vol. 464, no. 7285, 45–53, 2010.

[4] S. Pirandola *et al.*, "Advances in quantum cryptography," *Advances in Optics and Photonics*, vol. 12, no. 4, 1012–1236, 2020.

[5] F. Binder, L. A. Correa, C. Gogolin, J. Anders, and G. Adesso, Eds., *Thermodynamics in the Quantum Regime: Fundamental Aspects and New Directions*, Fundamental Theories of Physics, New York: Springer, 2018.

[6] S. Bhattacharjee and A. Dutta, "Quantum thermal machines and batteries," *arXiv:quant-ph/2008.07889*, 2020. (visited on 05/15/2021).

[7] M. Gluza *et al.*, "Quantum field thermal machines," *PRX Quantum*, vol. 2, no. 3, 030310, 2021.

[8] C.-G. Kang, "Origin of stability analysis: On governors by j.c. maxwell," *IEEE Control Systems Magazine*, vol. 36, no. 5, 77–88, 2016.

[9] I. Georgescu, "25 years of BEC," *Nature Reviews Physics*, vol. 2, no. 8, 396–396, 2020.

[10] T. Langen, *Non-equilibrium Dynamics of One-Dimensional Bose Gases*, ser. Springer Theses. Berlin: Springer, 2015.

[11] U. Hohenester, P. K. Rekdal, A. Borzi, and J. Schmiedmayer, "Optimal quantum control of bose einstein condensates in magnetic microtraps," *Physical Review A*, vol. 75, no. 2, 023602, 2007.

[12] J.-F. Mennemann, D. Matthes, R.-M. Weishäupl, and T. Langen, "Optimal control of bose-einstein condensates in three dimensions," *New Journal of Physics*, vol. 17, no. 11, 113027, 2015.

[13] J. Grond, G. von Winckel, J. Schmiedmayer, and U. Hohenester, "Optimal control of number squeezing in trapped bose-einstein condensates," *Physical Review A*, vol. 80, no. 5, 053625, 2009.

[14] "Optical dipole traps for neutral atoms," *Advances in Atomic, Molecular, and Optical Physics*, vol. 42, 95, 2000.

[15] M. Tajik *et al.*, "Designing arbitrary one-dimensional potentials on an atom chip," *Optics Express*, vol. 27, no. 23, 33474, 2019.

[16] S. A. Erne, "Far-from-equilibrium quantum many-body systems," Ph.D. dissertation, Ruperto-Carola-University of Heidelberg. Germany, 2018.

[17] O. E. Alon, A. I. Streltsov, and L. S. Cederbaum, "Multiconfigurational time-dependent hartree method for bosons: Many-body dynamics of bosonic systems," *Physical Review A*, vol. 77, no. 3, 033613, 2008.

[18] T. Brzozowski, M. Maczynska, M. Zawada, J. Zachorowski, and G. Wojciech, "Time-of-flight measurement of the temperature of cold atoms for short trap-probe beam distances," *Journal of Optics B: Quantum and Semiclassical Optics*, vol. 4, 62, 2002.

[19] J. Rogel-Salazar, "The gross-pitaevskii equation and bose-einstein condensates," *European Journal of Physics*, vol. 34, no. 2, 247–257, 2013.

[20] W. Bao and Y. Cai, "Mathematical theory and numerical methods for bose-einstein condensation," *Kinetic & Related Models*, vol. 6, no. 1, 1–135, 2013.

[21] A. Lode, "The multiconfigurational time-dependent hartree method for bosons with internal degrees of freedom: Theory and composite fragmentation of multi-component bose-einstein condensates," *Physical Review A*, vol. 93, 2016.

[22] M. L. Chiofalo, S. Succi, and M. P. Tosi, "Ground state of trapped interacting bose-einstein condensates by an explicit imaginary-time algorithm," *Physical Review E*, vol. 62, no. 5, 7438–7444, 2000.

[23] S. Rajendran, P. Muruganandam, and M. Lakshmanan, "Bright and dark solitons in a quasi 1d bose-einstein condensates modelled by 1d gross-pitaevskii equation with time-dependent parameters," *Physica D: Nonlinear Phenomena*, vol. 239, no. 7, 366–386, 2010.

[24] T. R. Taha and M. I. Ablowitz, "Analytical and numerical aspects of certain nonlinear evolution equations. II. numerical, nonlinear schrödinger equation," *Journal of Computational Physics*, vol. 55, no. 2, 203–230, 1984.

[25] U. Hohenester, "OCTBEC - a matlab toolbox for optimal quantum control of bose-einstein condensates," *Computer Physics Communications*, vol. 185, no. 1, 194–216, 2014.

[26] R. Kubo, "The fluctuation-dissipation theorem," *Reports on Progress in Physics*, vol. 29, no. 1, 255–284, 1966.

[27] W. Hänsel, J. Reichel, P. Hommelhoff, and T. W. Hänsch, "Trapped-atom interferometer in a magnetic microtrap," *Physical Review A*, vol. 64, no. 6, 063607, 2001.

[28] I. Lesanovsky, T. Schumm, S. Hofferberth, L. M. Andersson, P. Krüger, and J. Schmiedmayer, "Adiabatic radio-frequency potentials for the coherent manipulation of matter waves," *Physical Review A*, vol. 73, no. 3, 033619, 2006.

[29] G. J. Milburn, J. Corney, E. M. Wright, and D. F. Walls, "Quantum dynamics of an atomic bose-einstein condensate in a double-well potential," *Physical Review A*, vol. 55, no. 6, 4318–4324, 1997.

[30] P. Doria, T. Calarco, and S. Montangero, "Optimal control technique for many-body quantum dynamics," *Physical Review Letters*, vol. 106, no. 19, 190501, 2011.

[31] G. v. Winckel and A. Borzí, "Computational techniques for a quantum control problem with h1-cost," *Inverse Problems*, vol. 24, no. 3, 034007, 2008.

[32] P. Frazier, "Tutorial: Optimization via simulation with bayesian statistics and dynamic programming," *Proceedings of the 2012 Winter Simulation Conference (WSC)*, 1–16, 2012.

[33] H. K. Khalil, *Nonlinear Systems.* Upper Saddle River, NJ: Prentice Hall, 2002.

[34] O. Nelles, *Nonlinear System Identification: From Classical Approaches to Neural Networks and Fuzzy Models.* Berlin Heidelberg: Springer, 2001.

[35] B. Rauer *et al.*, "Cooling of a one-dimensional bose gas," *Physical Review Letters*, vol. 116, no. 3, 030402, 2016.

Eidesstattliche Erklärung

Hiermit erkläre ich, dass die vorliegende Arbeit gemäß dem Code of Conduct – Regeln zur Sicherung guter wissenschaftlicher Praxis (in der aktuellen Fassung des jeweiligen Mitteilungsblattes der TU Wien), insbesondere ohne unzulässige Hilfe Dritter und ohne Benutzung anderer als der angegebenen Hilfsmittel, angefertigt wurde. Die aus anderen Quellen direkt oder indirekt übernommenen Daten und Konzepte sind unter Angabe der Quelle gekennzeichnet. Die Arbeit wurde bisher weder im In– noch im Ausland in gleicher oder in ähnlicher Form in anderen Prüfungsverfahren vorgelegt.

Wien, November 2021

Katharina Schrom